

Syracuse University

SURFACE at Syracuse University

Dissertations - ALL

SURFACE at Syracuse University

Summer 8-27-2021

Binary Neutron Star Mergers: Gravitational-wave Measurements of Their Parameters and the Nuclear Equation of State

Daniel Roger Finstad
Syracuse University

Follow this and additional works at: <https://surface.syr.edu/etd>



Part of the [Astrophysics and Astronomy Commons](#)

Recommended Citation

Finstad, Daniel Roger, "Binary Neutron Star Mergers: Gravitational-wave Measurements of Their Parameters and the Nuclear Equation of State" (2021). *Dissertations - ALL*. 1374.
<https://surface.syr.edu/etd/1374>

This Dissertation is brought to you for free and open access by the SURFACE at Syracuse University at SURFACE at Syracuse University. It has been accepted for inclusion in Dissertations - ALL by an authorized administrator of SURFACE at Syracuse University. For more information, please contact surface@syr.edu.

ABSTRACT

Since making the first direct detection of gravitational waves in 2015, the Advanced Laser Interferometer Gravitational-Wave Observatory (LIGO) together with the Virgo observatory has detected an additional 51 confirmed signals from binary mergers. Two of these signals, GW170817 and GW190425, were identified as binary neutron star mergers. As detector sensitivity improves we expect to see many more binary neutron star merger events, both from future observing runs of the LIGO-Virgo network and from planned third-generation detectors. These new detections will provide an exquisite look at the nature of these systems and of neutron stars themselves. This thesis describes how gravitational-wave observations of neutron star mergers can be used to measure the properties of the binary systems and the fundamental physics of neutron stars. We use multimessenger observations of GW170817 to measure its viewing angle, which is important to understand the engine driving the electromagnetic counterpart to the gravitational-wave signal. We describe a new implementation of a fast likelihood model for gravitational-wave parameter estimation. We demonstrate that this likelihood allows analysis of binary neutron star signals to be performed quickly enough to inform strategies for electromagnetic follow-up observations. We measure the tidal deformabilities and radii of the neutron stars in GW170817, imposing a physical constraint to require that both neutron stars obey a common nuclear equation of state. We assess the future prospects for measuring the nuclear equation of state with the LIGO-Virgo network and with the planned third-generation detector, Cosmic Explorer.

**BINARY NEUTRON STAR MERGERS:
GRAVITATIONAL-WAVE MEASUREMENTS
OF THEIR PARAMETERS AND THE
NUCLEAR EQUATION OF STATE**

By

Daniel Finstad

B.A., University of California, 2015

DISSERTATION

SUBMITTED IN PARTIAL FULFILLMENT OF THE REQUIREMENTS

FOR THE DEGREE OF

DOCTOR OF PHILOSOPHY IN PHYSICS

Syracuse University

August 2021

Copyright © Daniel Finstad 2021
All rights reserved.

ACKNOWLEDGEMENTS

I would like to express my sincere gratitude to my advisor, Duncan Brown. I have benefited greatly from his extensive knowledge of gravitational-wave astronomy, and I attribute much of my development as an independent researcher to his mentorship. I am thankful to him for providing many research opportunities and for allowing me the freedom to explore several options to find research that I truly enjoy.

Working in the Syracuse gravitational wave group has been an unforgettable experience. The relaxed and welcoming environment that this group creates and works hard to maintain is what immediately told me I could find a home here, and it's something that I will dearly miss. I am particularly grateful to Peter Saulson for his careful explanations of the LIGO detectors and data, and for always being ready to use his shoe as a pendulum to make a point.

Many thanks to Chris Biver, Collin Capano, and Alex Nitz. In working with them over the past five years, I learned the fundamentals of how to conduct a gravitational-wave data analysis, and how to develop code for brand new analyses of my own design. I am thankful for all the skills I gained as a result of their expertise.

Thanks to Soumi De, Steven Reyes, and Chaitanya Afle for the innumerable conversations and contributions that have helped me find the solutions to many problems. Thank you for being such amazing research group members.

I would especially like to thank Lindsay DeMarchi. Words cannot express how grateful I am for all the help and support you've given me over the entire span of my graduate school career, from studying for the qual to writing this thesis. Thank you for being the kind of scientist and person that makes the world a better place for everyone.

To all other members of the Syracuse gravitational wave group—Derek Davis, Varun Srivastava, Erik Muniz, Ari Pedersen, Nick Didio, Daniel Vander-Hyde, Amber Lenon—thank you for all the fun and support.

Much of my research would have been impossible without Larne Pekowsky and Eric Sedore. I am thankful for their constant willingness to help with any and all computing questions and requests for resources, and for their infinite patience when I inevitably crashed the cluster.

To Ed Wishnow and Walt Fitelson—I wouldn't be where I am today without the research experience I gained working with you, and without all the great advice you've given me over the years. Thanks for taking a chance on me.

I would like to thank my defense committee members—Duncan Brown, Stefan Ballmer, Eric Coughlin, Scott Watson, Alex Nitz, and William Wylie—for taking the time to review and critique this thesis.

Finally, I would like to thank my parents, to whom this thesis is dedicated. Thank you for being such a great source of inspiration, and for your endless support and belief in me.

Contents

List of Tables	viii
List of Figures	xviii
Preface	xix
1 Introduction	1
1.1 Gravitational-wave detectors	2
1.2 Multimessenger astrophysics	3
1.3 Nuclear equation of state	4
2 Parameter Estimation Techniques	10
2.1 Bayesian inference	10
2.2 Sampling	12
2.2.1 Markov Chain Monte Carlo	12
2.2.2 Nested sampling	13
2.3 Practical considerations	14
2.3.1 Waveform model	15
2.3.2 emcee_pt	17
2.3.3 dynesty	17
2.3.4 Long duration signals	18
2.3.5 Relative likelihood	18
3 Measuring the Viewing Angle of GW170817 with Electromagnetic and Gravitational Waves	20
3.1 Introduction	21

3.2	Methods	22
3.3	Results	24
3.4	Discussion	26
4	Fast Parameter Estimation of Binary Mergers for Multimessenger Followup	30
4.1	Introduction	31
4.2	Simulated Search	32
4.3	Parameter estimation	34
4.4	Results	36
4.5	Conclusion	40
5	Tidal Deformabilities and Radii of Neutron Stars from the Observation of GW170817	47
5.1	Introduction	48
5.2	The common equation of state constraint	48
5.3	Implications for the neutron star radius	49
5.4	Parameter estimation methods	50
5.5	Results	54
5.6	Discussion	56
6	Prospects for Precise Equation of State Measurements from Advanced LIGO and Cosmic Explorer	66
6.1	Introduction	67
6.2	Simulated signals	71
6.3	Equation of state in gravitational waves	73
6.4	Parameter estimation	74
6.5	Results	76
6.6	Conclusion	79
7	Conclusions	90
	Bibliography	114

List of Tables

1	Results from parameter estimation analyses using three different mass prior choices with the common EOS constraint, and applying the causal minimum constraint to $\Lambda(m)$. We show 90% credible intervals for $\tilde{\Lambda}$, 90% credible intervals and systematic errors for \hat{R} , and the 90% upper limits on $\tilde{\Lambda}$	57
---	--	----

List of Figures

1	Noise curves, plotted as the amplitude spectral density, for the LIGO detectors in the most recently completed observing run (aLIGO) as well as a selection of proposed upgrade stages and future detectors. LIGO A+ is a planned upgrade to the LIGO detectors which will include improved quantum squeezing and mirror coatings. Voyager is a planned detector featuring a new design in the existing LIGO facilities, which will operate with a laser of 2 micron wavelength. NEMO is a proposed Australian detector optimized for high frequency sensitivity to study neutron star physics [1]. Cosmic Explorer is a planned third-generation detector similar in design to the LIGO detectors except with 40 km arms. Einstein Telescope is another planned third-generation detector which will be located underground, with 10 km arms in an equilateral triangle configuration.	9
2	Sky localizations of GW170817 for LIGO/Virgo (green shaded region) and from our analysis using only GW source information (black contour). Both localizations are 90% confidence regions, while the LIGO/Virgo region shows contours at each 10% threshold. The location of NGC 4993 is marked as a red star.	27

3	<p>Comparison of posterior probability distributions without and with combined EM information. The black contours show the results for using only the GW signal, the blue contours show the results for the fixed sky location of NGC 4993, and the red contours show the results for both the fixed sky location and a Gaussian prior on distance of 40.7 ± 2.36 Mpc from [2]. These analyses used a prior on inclination angle that is uniform in $\cos \iota$. For each parameter, we quote the median value and the 90% credible interval (shown with vertical solid and dashed lines, respectively, on the posterior plot of each parameter). The EM information on the distance measurement greatly improves the precision with which we measure the inclination angle (and significantly reduces the uncertainty on the source-frame chirp mass).</p>	28
4	<p>Inclination angle posteriors (solid lines) plotted against their prior (dotted lines) for two choices of prior: uniform in ι (left), and uniform in $\cos \iota$ (right). We quote the median value and the 90% credible interval for ι in each posterior (shown with vertical lines). The prior uniform in $\cos \iota$ is the prior used by the LIGO/Virgo analysis. The uniform prior does not bias measurement away from angles approaching 180°, so these results suggest that our likelihood is informative close to $\iota = 180^\circ$ and that we can place a conservative lower bound on the viewing angle $\Theta \geq 13^\circ$ (90% confidence).</p>	29

5	<p><i>Left:</i> The wall-clock time in minutes that it takes to perform the parameter estimation using the coherent relative binning likelihood and nested sampling on 32 cores of an Intel[®] Xeon[®] Gold 6140 processor running at a clock speed of 2.3 GHz as a function of the network signal-to-noise ratio of the maximum likelihood template. The average run-time for a single signal is 10.8 minutes, with the maximum run-time being 20 minutes for all signals. Increasing the number of cores does not significantly decrease the wall-clock run-time. The run-time shows a slight increase as a function of the signal-to-noise ratio, as expected given that signals with a larger signal-to-noise ratio have a more narrowly peaked likelihood. <i>Right:</i> The fraction of injections recovered within a credible interval plotted as a function of credible interval. Fidelity to the 1:1 diagonal line is an indication of probability being uniformly distributed across a given parameter’s posterior distribution and is a measure of the accuracy of this analysis at the population level. We find that all of the parameters of interest are estimated in an unbiased way by our parameter estimation method. .</p>	42
6	<p>Fraction of injections recovered as a function of the 90% confidence localization area. The localization results from our parameter estimation analysis are shown in blue, and those from the Bayestar algorithm are in orange. The dotted lines show the results for the entire set of signals, while solid lines show only signals that were above the detection threshold in all three detectors in our simulated search. We find our localization areas are consistently smaller than those from Bayestar, as indicated by the blue lines lying to the left of the orange lines, although the difference in areas is not large. The improvement in localization area between Bayestar and our analysis is 14 deg² on average, and is comparable between the set of triple-coincident signals and the set of all signals.</p>	43

7	<p>Chirp mass and mass ratio recovery metrics for the binary neutron star (left column) and neutron star–black hole (right column) signals in our analysis. <i>Top row:</i> Difference between source-frame chirp mass estimates and the true injected value, as a function of signal-to-noise ratio. Blue circles denote differences from the median posterior values from parameter estimation, while orange circles show differences from best-fit template values from the search. We find that on average our parameter estimation results improve on the accuracy of the best-fit template by a factor of 2. <i>Middle and bottom rows:</i> Fractional uncertainties on chirp mass and mass ratio, respectively, calculated as the ratio of standard deviation and mean of the posterior distributions. Uncertainties from our relative-binned analysis are shown as blue circles, and those from a standard non-relative likelihood analysis on a subset of the population are shown as orange diamonds. Our relative-binned results are consistent with the non-relative analysis, and also with the results in [3].</p>	44
8	<p>Difference between parameter estimates and true injected values for some component parameters of interest, plotted against signal-to-noise ratio. The left column shows results for the component masses of binary neutron star signals, and the right column shows results for the component masses and black hole spin of neutron star–black hole signals. Differences are computed from median posterior values, and masses have been converted to the source-frame using the distance posteriors. We find both component masses of binary neutron star signals are generally constrained to within $\sim 0.5M_{\odot}$ of the true value for all signals, while the majority of primary and secondary masses of neutron star–black hole signals are within about $3M_{\odot}$ and $1M_{\odot}$ respectively. We find our black hole spin measurements are uninformative below a signal-to-noise of 20, but for louder signals the spin is within about 0.3 of the true value.</p>	45

9	Posterior distributions from a relative-binned parameter estimation analysis of GW170817 (black contour) as compared to a run using the standard non-relative likelihood (blue contour). Marginalized 1-dimensional histograms for each parameter are shown along the diagonal, with vertical dashed lines at the median value and the bounds of the 90% credible interval. Off-diagonal plots show 2-dimensional slices of the parameter space with contours delineating the 50% and 90% credible regions. The relative-binned analysis completed in 20 minutes versus roughly 3 hours in the non-relative case, and all parameter distributions are consistent between the two analyses.	46
10	The tidal deformability Λ as a function of mass for physically realistic polytropes. A TOV integration with each EOS parameter set results in a series of values of $\Lambda(m)$ that are shown as points colored by their radii R . Dashed curves are lower bounds to Λ for a given mass m which vary depending on the assumed lower limit to the neutron star maximum mass, m_{max} . All values of m_{max} produce the same upper bound.	59
11	Posterior probability densities for $\Lambda_{1,2}$ with the common EOS constraint using uniform (left), double neutron stars (middle), and Galactic neutron stars (right) component mass priors. The 50% and 90% credible region contours are shown as solid curves. Overlaid are contours of $\tilde{\Lambda}$ (in magenta) and q (in gray). The values of Λ_1 and Λ_2 forbidden by causality have been excluded from the posteriors. . . .	60
12	Measurability [4] of the chirp mass \mathcal{M} , SNR ρ and binary deformability $\tilde{\Lambda}$ in the frequency range 10 Hz - 2000 Hz. Each detector's parameter measurability is scaled to the maximum frequency to show the relative accumulation of measurement over the detector's frequency band. Note that between detectors, L1 is more sensitive than H1, which is more sensitive than V1. Measurability of chirp mass is accumulated primarily at low frequencies, whereas measurability of tidal deformability is accumulated at higher frequencies. We extend computation of the likelihood down to 20 Hz where the measured signal-to-noise ratio (the logarithm of the likelihood) drops to zero in all three detectors.	61

13	Posterior probability density function for Λ_1, Λ_2 from unconstrained $\Lambda_{1,2} \sim U[0, 3000], m_{1,2} \sim U[1, 2] M_\odot, 1.1876 \leq \mathcal{M} \leq 1.2076, m_1 \geq m_2,$ 30 Hz low-frequency cutoff analysis. The black dotted lines show 50% and 90% upper limits from our analysis. The red dotted lines show 50% and 90% upper limits from the LIGO-Virgo analysis [5].	62
14	Comparison of the prior probability distributions on $\tilde{\Lambda}$ for the three mass priors imposing the common EOS constraint: uniform (purple), double neutron stars (red), galactic neutron stars (green) with a prior in $\Lambda_{1,2} \sim U[0, 3000]$ and $m_{1,2} \sim U[1, 2]M_\odot, m_1 \geq m_2$ without the common EOS constraint (blue). The priors in the common EOS analysis are uniform across the region of interest.	63

- 15 Posterior distributions for the source frame chirp mass \mathcal{M}^{src} , mass ratio q , source frame primary mass m_1^{src} and secondary mass m_2^{src} , effective spin χ_{eff} , and binary deformability parameter $\tilde{\Lambda}$ from parameter estimation analyses with three different choices of mass priors. The posteriors represented in blue are from the analysis using a uniform prior on component masses, $m_{1,2} \sim U[1, 2] M_{\odot}$, and 20 Hz low-frequency cutoff. The posteriors represented in red are from the analysis using a Gaussian mass prior for component masses $m_{1,2} \sim N(\mu = 1.33, \sigma = 0.09) M_{\odot}$ known from radio observations of neutron stars in double neutron star (DNS) systems, and 20 Hz low-frequency cutoff. The posteriors represented in green are from the analysis using the observed mass distributions of recycled and slow pulsars in the Galaxy with $m_1 \sim N(\mu = 1.54, \sigma = 0.23) M_{\odot}$ and $m_2 \sim N(\mu = 1.49, \sigma = 0.19) M_{\odot}$ [6], and 20 Hz low-frequency cutoff. The posteriors represented in gray are from the analysis using a uniform prior on component masses, $m_{1,2} \sim U[1, 2] M_{\odot}$, and 25 Hz low-frequency cutoff. All four analyses had the common EOS constraint and the causal $\Lambda(m)$ lower limit imposed. The one-dimensional plots show marginalized probability density functions for the parameters. The dashed lines on the one-dimensional histograms represent the 5%, 50% and 95% percentiles for each analysis, the values of which are quoted in the titles of the histograms. The 2D plots show 50% and 90% credible regions for the different pairs of parameters. Comparison between the analyses with low-frequency cutoff 20 Hz (blue) and 25 Hz (gray) for the uniform mass prior case shows that extending from 25 Hz to 20 Hz better constrains \mathcal{M} , which improves the measurement of $\tilde{\Lambda}$ by eliminating a region of the posterior with higher values \mathcal{M} and high $\tilde{\Lambda}$ 64
- 16 The 90% credible region of the posterior probability for the common radius \hat{R} and binary tidal deformability $\tilde{\Lambda}$ with the common EOS constraint for the three mass priors. The posteriors for the individual parameters are shown with dotted lines at the 5%, 50% and 95% percentiles. The values of $\tilde{\Lambda}$, and hence \hat{R} forbidden by causality have been excluded from the posteriors. 65

17	Match between gravitational waveforms for equal mass binaries with and without tidal deformability included. The match is calculated as the noise-weighted overlap between the two waveforms in the frequency range 20 – 2048 Hz using the Advanced LIGO design sensitivity noise curve <code>aLIGODesignSensitivityP1200087</code> . Waveforms are generated using masses ranging from $1 - 2M_{\odot}$, and for the waveform including tidal deformability we use values of $\tilde{\Lambda} = \Lambda_1 = \Lambda_2$ that span the range of plausible values between the soft (lower curve) and stiff (upper curve) equations of state selected for our analysis.	81
18	The radius in kilometers and dimensionless tidal deformability of a $1.4M_{\odot}$ neutron star, denoted $R_{1.4}$ and $\Lambda_{1.4}$, for the equations of state used in this work. The soft, medium, and stiff equations of state whose measurability we assess, EOS 487, EOS 895, and EOS 1250, are shown as a red diamond, red cross, and red star, respectively. The $(\Lambda_{1.4}, R_{1.4})$ coordinates for the 2000 equations of state used as a prior distribution in our analysis are shown in blue. Shaded regions represent a selection of constraints on the equation of state from gravitational-wave and electromagnetic observations, and nuclear experiment. The constraints span a significant range with potentially some tension between them. The three equations of state we investigate in this work are chosen to span the majority of the range covered by these constraints.	82
19	Combined $R_{1.4}$ measurements for our Gaussian mass distributed population in the LIGO-Virgo network. Results are shown for the soft (blue), medium (orange), and stiff (green) equations of state that we used. Signals are combined one at a time to show an updating constraint on the measurement as each signal is added. Shaded regions represent the 90% credible interval for each measurement. The true values of $R_{1.4}$ for each of the equations of state are plotted as horizontal dashed lines in the appropriate color. Dotted lines show the fractional uncertainty in the measurement at each number of signals included, measured as the ratio of the 90% credible interval to the true value of $R_{1.4}$ for a given equation of state.	83

20	Same as Figure 19 except including only signals with signal-to-noise $\rho < 30$. By removing louder signals we attempt to mitigate any potentially outsize effect on the radius constraint from signals that are unlikely to be seen by the LIGO-Virgo network. For the stiff, medium, and soft equations of state we find that a 10% precision measurement on $R_{1.4}$ is reached after 5, 30, and 50 signals, respectively.	84
21	Same as Figure 19 except we recover all signals with a uniform prior on the source-frame component masses from $1 - 2M_{\odot}$. This incorrect choice of mass prior introduces a bias in the equation of state measurement, leading to systematically lower estimates of $R_{1.4}$. We find that for EOS 1250 and EOS 895 the bias causes the true equation of state to be ruled out at high confidence after about 20 and 100 signals, respectively.	85
22	Combined $R_{1.4}$ measurements for our uniform mass population in the LIGO-Virgo network. Source-frame component masses are drawn from $1 - 2M_{\odot}$ to represent a population with more high-mass neutron stars. All signals are recovered with a uniform mass prior from $1 - 2M_{\odot}$ and signals are combined following the same procedure as the Gaussian mass population. We find the combined equation of state measurements from the uniform mass population are essentially unchanged from the Gaussian mass population, with precision on the measurement of $R_{1.4}$ ranging from $1 - 2\%$	86
23	Probability of seeing 10, 25, and 50 events with signal-to-noise $\rho > 10$ over time, assuming the population of merging binary neutron stars in the local universe follows the universal signal-to-noise distribution described in [7]. The probabilities for 10, 25, and 50 events are shown as solid, dashed, and dotted lines, respectively. We use the median binary neutron star merger rate estimate from [8] and the projected sensitive volume for the upcoming fourth observing run (O4) of the Advanced LIGO network [9] to plot probabilities against number of years at O4 sensitivity. We assume a detection threshold network signal-to-noise ratio of 9.	87

24	<p>Combined $R_{1.4}$ measurements for our Gaussian mass distributed population in Cosmic Explorer, which is representative of the signals expected in one year of observation. Results are shown for the soft (blue) and medium (orange) equations of state in our analysis. As in Fig. 19 the horizontal dashed lines indicate the true value of $R_{1.4}$ for each equation of state, and the dotted lines show the calculated fractional uncertainty which is defined as the ratio of the 90% credible interval to the true value of $R_{1.4}$. We find that for both equations of state, a 10% precision threshold on the measurement of $R_{1.4}$ is achieved almost immediately, consistent with the third-generation detector result from [10]. The measurement precision improves to 0.6% and 0.15% for the soft and medium equations of state, respectively, after all signals are combined.</p>	88
25	<p>Same as Figure 24 except we recover signals using a uniform mass prior from $1 - 2M_{\odot}$. The ordering of signals has been preserved from the Gaussian prior analysis for comparison, and it can be seen that the combined constraints for both equations of state is again biased toward smaller radii as a result of the incorrect mass prior. The bias is smaller than what was seen in our LIGO-Virgo analysis as a result of the much louder signals in the Cosmic Explorer population, however the true values for both equations of state are still found at the edge of their respective 90% credible interval because of the correspondingly smaller statistical uncertainties on these measurements.</p>	89

Preface

Chapter 3 is based on material from:

Daniel Finstad, Soumi De, Duncan A. Brown, Edo Berger, Christopher M. Biwer, “Measuring the Viewing Angle of GW170817 with Electromagnetic and Gravitational Waves,” **The Astrophysical Journal Letters**, Volume 860, Number 1 (2018)
<https://iopscience.iop.org/article/10.3847/2041-8213/aac6c1>.

Chapter 4 is based on material from:

Daniel Finstad, Duncan A. Brown, “Fast Parameter Estimation of Binary Mergers for Multimessenger Followup,” **The Astrophysical Journal Letters**, Volume 905, Number 1 (2020)
<https://iopscience.iop.org/article/10.3847/2041-8213/abca9e>.

Chapter 5 is based on material from:

Soumi De, *Daniel Finstad*, James M. Lattimer, Duncan A. Brown, Edo Berger, Christopher M. Biwer, “Tidal Deformabilities and Radii of Neutron Stars from the Observation of GW170817,” **Physical Review Letters**, Volume 121, Issue 9 (2018)
<https://journals.aps.org/prl/abstract/10.1103/PhysRevLett.121.091102>.

To Mom, Dad, & Lynn

Chapter 1

Introduction

The Advanced LIGO [11] gravitational-wave detector network has completed three observing runs to date, searching the universe for astrophysical signals from coalescing binary systems, spinning neutron stars, and core-collapse supernovae. The first observing run saw the first direct detection of gravitational waves from the binary black hole merger GW150914 [12]. The Virgo detector [13] joined the network towards the end of the second observing run, and on August 17, 2017 the first signal from a binary neutron star merger was observed [5]. The aftermath of this binary neutron star merger was observed across the entire electromagnetic spectrum [14], from gamma-rays to radio, providing an unprecedented window onto the dynamics of these events. The full catalog of confident detections to date stands at 52 signals [15, 16], including two from binary neutron stars, two probable neutron star–black hole systems [17], and a binary system whose secondary compact object is either the highest mass neutron star or the lowest mass black hole ever observed [18]. With the next observing runs of the current detector network promising significantly improved sensitivity [9], and planning well underway for the third-generation detectors Cosmic Explorer [19] and Einstein Telescope [20], the coming decades will provide an incredible opportunity to improve our understanding of neutron stars, black holes, and fundamental physics. In this thesis, we use observations of binary neutron star mergers to study the properties of neutron stars. We also examine the ability of current and future gravitational-wave detectors to measure the nuclear equation of state which describes the behavior of the high density nucleonic matter that makes up the interior of a neutron star.

1.1 Gravitational-wave detectors

The two Advanced LIGO detectors, located in Hanford, Washington and Livingston, Louisiana, together with the Virgo detector in Cascina, Italy comprise a worldwide gravitational-wave detector network. These detectors are Michelson interferometers with a Fabry-Perot cavity in each arm which stores the laser light for ~ 100 bounces, increasing the apparent arm length by two orders of magnitude. As a gravitational-wave passes through the detector it causes space-time to be stretched and squeezed. In an interferometric gravitational-wave detector this distortion results in small changes in the lengths of the arms. This change in arm length is measured as a phase difference over time in the laser light that is recombined from both arms, which allows the measurement of a passing gravitational wave.

Gravitational-wave detectors measure signal amplitude in terms of dimensionless “strain” h , which is given by

$$h = \frac{\Delta L}{L}, \quad (1.1)$$

where L is the arm length of the detector and ΔL is the change in arm length induced by the source. The sensitivity of the detectors is determined by a combination of noise sources including environmental, thermal, and quantum noise, among others [21]. Each noise source impacts detector sensitivity in particular frequency bands, e.g. environmental noise includes seismic motion which limits detector sensitivity at frequencies $\lesssim 10$ Hz, and quantum noise includes uncertainty in the photon arrival time which can be interpreted as shot noise and suppresses sensitivity at frequencies $\gtrsim 200$ Hz. The overall sensitive band for the LIGO and Virgo detectors is roughly 15 – 1000 Hz. From Eqn. 1.1 it can be seen that detector sensitivity increases with arm length L . To take advantage of this, the LIGO detectors were designed with 4 km arms and the Virgo detector has 3 km arms. Cosmic Explorer is a planned third-generation detector which will use the same general design as the LIGO and Virgo detectors except it will have 40 km arms. By increasing the arm lengths by an order of magnitude as compared to the LIGO detectors, Cosmic Explorer will have roughly an order of magnitude greater sensitivity. In Fig. 1 we show the noise curves for the LIGO detectors in the most recent observing run, as well as planned upgrade stages and a number of proposed detectors.

1.2 Multimessenger astrophysics

The first observed binary neutron star merger GW170817 was also the first “multimessenger” gravitational-wave event, as it was observed with both gravitational and electromagnetic waves: a short gamma-ray burst was observed ~ 2 seconds after the gravitational-wave signal [22, 23], and subsequent electromagnetic emission at X-ray, ultraviolet, optical, infrared, and radio frequencies identified a two-component kilonova [24, 25, 26, 27, 28, 29, 30]. Detection of an electromagnetic counterpart enables better understanding of the nature of the merger event and the properties of the neutron stars involved. One example of the benefit of multimessenger information is to break the distance-inclination degeneracy that is present in the amplitude of a gravitational-wave signal from a binary merger. This degeneracy arises from the fact that the gravitational-wave emission is strongest parallel or anti-parallel to the direction of the orbital angular momentum of the binary [31], as a result of the amplitude of the two polarizations of the gravitational wave being maximum in these directions [32]. Thus the inclination of the orbital plane is degenerate with the distance to the source, where a more face-on (or face-away) orientation of the binary at a larger distance is degenerate with a binary that is closer, but less well-aligned.

In Ch. 3 we present an analysis of GW170817 informed by electromagnetic distance measurements of its identified host galaxy, NGC 4993 [33]. We demonstrate that using an independent distance measurement in a gravitational-wave analysis can break the distance-inclination degeneracy to allow for much tighter constraints on the inclination angle of the orbital plane of the binary with respect to the line of sight. We present our measurement in the context of the timing delay of the gamma-ray burst and observations of the long-lived kilonova afterglow emission to discuss implications for jet models.

With the increased sensitivity of the next observing runs and future detectors, we expect significantly more potential multimessenger events in the coming years, such that it will be necessary for gravitational-wave parameter estimation analyses to complete in a short amount of time to enable efficient prioritization of resources for electromagnetic follow-up observations [34]. However, the measurement of source parameters for low-mass binary inspirals, such as binary neutron star or neutron star–black hole mergers, is very computationally expensive as a result of the long duration

of these signals in the sensitive band of gravitational-wave detectors: a typical binary neutron star signal entering the sensitive band at 20 Hz will last several minutes before merging. At a sample rate of 4096 Hz, which is standard for most parameter estimation analyses, this translates to $\sim 2 \times 10^5$ frequency-domain data samples required to capture the signal. Each evaluation of the likelihood then requires a frequency-domain inner-product of this detector data with a template waveform, and a full parameter estimation analysis can require $\mathcal{O}(10^9)$ likelihood evaluations [35]. Several methods have been developed to help reduce computational cost [36, 37, 38, 39, 40, 41, 42, 43, 44]. In this thesis we focus on the “relative binning” technique, which uses an approximation to the likelihood near its peak in order to allow the use of fewer frequency samples in each likelihood calculation [45, 46].

In Ch. 4 we present an implementation of the relative binning parameter estimation technique as a likelihood model in *PyCBC Inference*. We extend the relative model to a coherent network statistic to allow sky localization, and we enable use for any frequency-domain waveform approximant available in LALSuite [47]. We validate the relative model on large simulated populations of binary neutron star and neutron star–black hole signals. We demonstrate the feasibility of seeding the analysis of each simulated signal with the best-fit template parameters from a low latency search pipeline, showing the real-world utility of this model in producing fast and accurate parameter estimates that can be used to inform electromagnetic follow-up observations.

1.3 Nuclear equation of state

Neutron stars contain matter at some of the highest densities in the known universe, therefore they can serve as astrophysical laboratories to study how matter behaves under these extreme conditions. The behavior of this dense matter is described by the nuclear equation of state. Gravitational waves from a binary neutron star merger will carry information about the nuclear equation of state through the tidal deformability Λ of the neutron stars: as the pair of neutron stars inspiral and their orbital separation decreases, the gravitational field of each star will induce a deformation in the body of its companion. This tidal deformation is measurable in a gravitational-wave signal as the energy required to induce the effect alters the gravitational-wave phase evolution

of the inspiral [48].

The gravitational waveforms used to measure the nuclear equation of state are computed using either post-Newtonian methods, which are perturbative expansions in the invariant velocity of the binary, or using effective-one-body models that include tidal effects [49, 50, 51, 52, 53, 54] and provide better accuracy than post-Newtonian models by tuning higher-order terms to numerical relativity waveforms. The post-Newtonian waveform is written as a power series in the invariant velocity $v = (\pi M f)^{1/3}$, where f is the gravitational-wave frequency and $M = m_1 + m_2$ is the total mass of the binary. As v increases throughout the inspiral, the tidal terms become large enough to contribute a measurable phase shift in the gravitational-wave signal. Since the tidal deformation only becomes significant for small orbital separations, the effect in the gravitational-wave signal is only measurable at the higher frequencies just before merger. It has been found that tidal effects only become important for frequencies $f \gtrsim 400$ Hz [55]. Gravitational-wave detectors that use a laser interferometer are generally less sensitive at these higher frequencies as a result of quantum noise [56], making tidal effects challenging to measure.

In Ch. 5 we perform the first open-data analysis of GW170817 focused on measuring the tidal deformability of the merging neutron stars. We impose a physical constraint requiring that both neutron stars obey a common equation of state, and we construct a prior on the leading order tidal parameter that is uniform to reflect our uninformed prior knowledge. We describe the derivation of our constraint and present measurements of the tidal deformability and neutron star radius under several different assumptions about the mass distribution of neutron stars in merging binaries.

A number of previous studies have examined Advanced LIGO's ability to measure the neutron star equation of state through the star's tidal deformability. Lackey *et al.* [57] performed parameter estimation for the loudest twenty binary neutron star events in a year of data, with signal-to-noise ratios ranging from 13 to 64 in Advanced LIGO at design sensitivity. They found that only the loudest five events are the most informative toward constraining the equation of state. To constrain the equation of state they measure the tidal deformability parameter $\tilde{\Lambda}$, which is the linear combination of the individual tidal parameters Λ_1 and Λ_2 . To combine the information from multiple events, they follow a two-step process. First, they sample

the posteriors for each of the events individually and then marginalize over all the parameters except the equation of state dependent parameters (i.e. $m_1, m_2, \tilde{\Lambda}$) to obtain a quasilielihood. In the second step they sample the joint likelihood for n binary neutron star events, taking into account that $\tilde{\Lambda}$ can be expressed in terms of the masses and the equation of state parameters, and then marginalize over the masses. They also use Fisher matrix analysis for high signal-to-noise ratio events to compute the quasilielihood, and find that for the most part the results with Fisher matrix are comparable to the Bayesian analysis, but that they slightly underestimate the uncertainty in radius, pressure and tidal deformability. They find that when stacking events together, the statistical error reduces, but the systematic error remains. They claim that systematic errors are due to uncertainties in the post-Newtonian waveform models.

Agathos *et al.* [58] expand on the work by Ref. [57] by including more events, spins for the neutron stars, and by terminating the waveforms at the first point of contact. They also include higher post-Newtonian terms in their waveform model. They attempt to infer the neutron star equation of state via two methods: hypothesis ranking and parameter estimation. For hypothesis ranking, they evaluate the odds ratio and rank the equations of state. The highest ranked equation of state is assumed to be the one that is closest to the true equation of state. For parameter estimation, they expand the $\Lambda(m)$ relation around $m_0 = 1.4M_\odot$ at quadratic order. This allows them to combine the equation of state dependent parameters for multiple detections, which are the coefficients c_j in the quadratic expression for $\Lambda(m)$. For the signals they use, they are only able to measure c_0 and can't infer c_1, c_2 . Their signals have signal-to-noise ratio between 8 and 30. They find that more than 50 sources are needed to make comparative equation of state studies successful for the equations of state that they examine. They also find that if the source mass distribution is strongly peaked, using flat priors while inferring the equation of state parameters induces systematic errors. They suggest that this can be mitigated by including better priors for the masses by incorporating information on masses from other astrophysical observations. Unfortunately, the equations of state examined by Agathos *et al.* are quite stiff (i.e. have a large radius for a given mass), and they are disfavored by GW170817. Since the measurability of the tidal deformability depends on the nuclear equation of state,

with stiffer equations being easier to probe as they produce a larger gravitational-wave phase shift, the results of Agathos *et al.* are overly optimistic in light of current knowledge.

More recent work has extended the above analyses using the Fisher matrix formalism, and the inclusion of measurements of the equation of state by other independent methods such as from *NICER*. Forbes *et al.* [59] perform Fisher matrix analysis for low signal-to-noise ratio events while parameterizing the equation of state with 18 different parameters. They claim that a handful of events will be able to significantly constrain the equation of state. Similarly, Carson *et al.* [60] use a Fisher matrix analysis to explore the implications of multiple binary neutron star detections with current and future generation detectors to determine the uncertainty in measuring the tidal deformability. They claim that the uncertainties will continue to dominate until the end of Voyager-type detectors.

Recently, Landry *et al.* [61] studied the equation of state constraints from multiple gravitational wave observations, *NICER* observations, and including information from the detection of the most massive neutron stars observed as radio pulsars. They estimate ~ 60 total events by the end of Advanced LIGO's fourth observing run, and ~ 4 events with signal-to-noise ratio ≥ 20 . They claim that with multiple binary neutron star events by the end of Advanced LIGO's fifth observing run, and including the *NICER* and radio observations, tight constraints can be placed on the equation of state. They find that the uncertainty in the tidal deformability of a $1.4M_{\odot}$ neutron star $\Delta\Lambda_{1.4}$ goes as $\sim 910/\sqrt{n}$, where n is the number of binary neutron star events detected by a gravitational-wave detector. This is consistent with results from Carson *et al.*

In Ch. 6 we present a comprehensive study of the future prospects for a precise equation of state measurement from Advanced LIGO and the proposed third-generation detector Cosmic Explorer. We use the latest information from astrophysical observations to explore a realistic range of equations of state, and perform full Bayesian parameter estimation without relying on approximate Fisher-matrix techniques. We explore the measurability of the equation of state across the full range allowed by recent constraints from gravitational-wave and electromagnetic observations, as well as nuclear experiments. We investigate the effect of different neutron

star mass distributions on the ability to make precise measurements, and we demonstrate the importance of a good estimate of the true mass distribution to mitigate biases in measuring the equation of state.

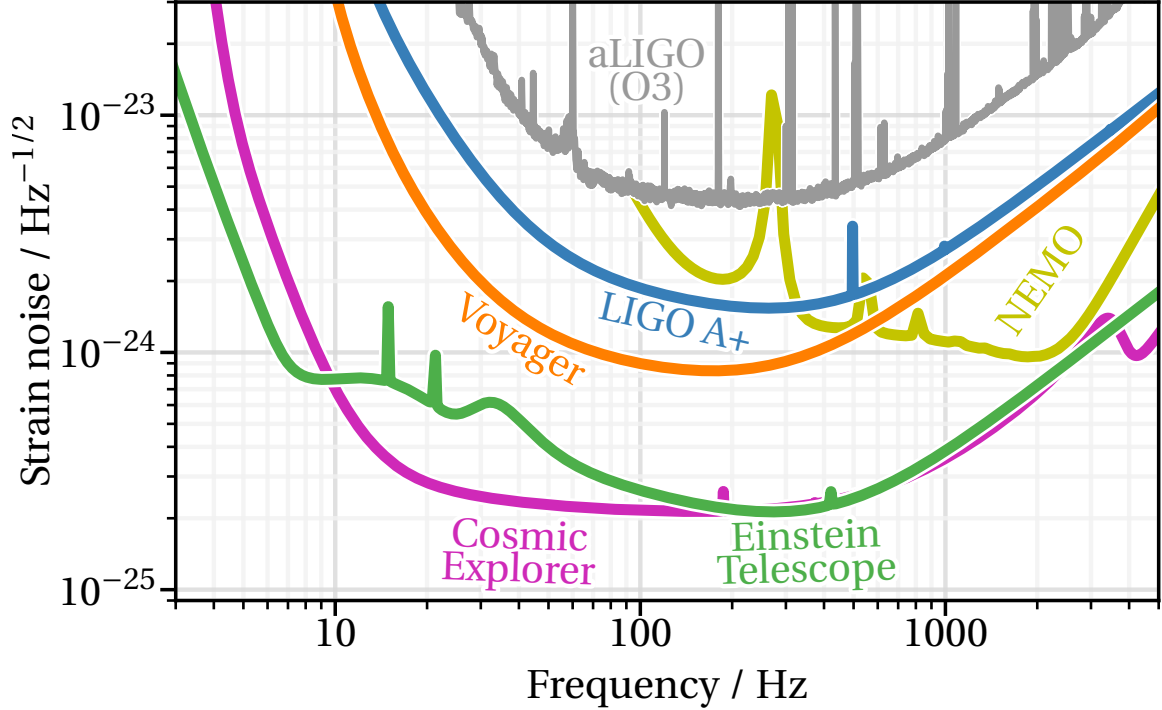


Figure 1: Noise curves, plotted as the amplitude spectral density, for the LIGO detectors in the most recently completed observing run (aLIGO) as well as a selection of proposed upgrade stages and future detectors. LIGO A+ is a planned upgrade to the LIGO detectors which will include improved quantum squeezing and mirror coatings. Voyager is a planned detector featuring a new design in the existing LIGO facilities, which will operate with a laser of 2 micron wavelength. NEMO is a proposed Australian detector optimized for high frequency sensitivity to study neutron star physics [1]. Cosmic Explorer is a planned third-generation detector similar in design to the LIGO detectors except with 40 km arms. Einstein Telescope is another planned third-generation detector which will be located underground, with 10 km arms in an equilateral triangle configuration.

Chapter 2

Parameter Estimation Techniques

We give an overview of the techniques of gravitational-wave parameter estimation, which are employed widely throughout this thesis. We outline the basic principles behind Bayesian inference for gravitational-wave astronomy and the sampling methods we use to produce posterior estimates in our analyses. We also comment on some practical considerations we found useful in the completion of this work, though we emphasize the items we discuss are by no means an exhaustive list.

2.1 Bayesian inference

In gravitational-wave astronomy we use Bayesian methods as a convenient way to infer the astrophysical source parameters from a detected signal [62, 63, 64, 65]. For a stretch of gravitational-wave detector data $\vec{d}(t)$ identified as containing a gravitational-wave signal, Bayes' theorem [66, 67] states that for a hypothesis H , the posterior probability density is

$$p(\vec{\vartheta}|\vec{d}(t), H) = \frac{p(\vec{d}(t)|\vec{\vartheta}, H)p(\vec{\vartheta}|H)}{p(\vec{d}(t)|H)}. \quad (2.1)$$

Here $p(A|B)$ denotes the conditional probability of A given B . In the context of gravitational-wave inference, the hypothesis H is the model of the gravitational waveform, and $\vec{\vartheta}$ is the set of parameters defining this model. Thus the posterior probability density $p(\vec{\vartheta}|\vec{d}(t), H)$ is the conditional probability that the gravitational-wave signal is defined by parameters $\vec{\vartheta}$, given data $\vec{d}(t)$ and waveform model H . The prior probability density $p(\vec{\vartheta}|H)$ represents our prior knowledge of the parameters $\vec{\vartheta}$ before

considering the observed data $\vec{d}(t)$. The posterior probability density is proportional to the prior probability density, as the Bayesian framework considers any new observations in the broader context of prior knowledge. The denominator of Eqn. 2.1, $p(\vec{d}(t)|H)$ is known as the ‘‘evidence’’ or ‘‘marginal likelihood,’’ and it serves as a normalizing constant to ensure the integral of $p(\vec{\vartheta}|\vec{d}(t), H)$ over the parameter space is equal to unity.

In practice, we are very often interested in posterior estimates of only one or a few parameters. In this case we can obtain marginalized posterior probability density functions by integrating $p(\vec{\vartheta}|\vec{d}(t), H)$ over all unwanted parameters. For instance, given a set of parameters $\vec{\vartheta} = \{\theta_1, \theta_2, \dots, \theta_n\}$, the marginalized posterior probability density for source parameter θ_1 is

$$p(\theta_1|\vec{d}(t), H) = \int p(\vec{\vartheta}|\vec{d}(t), H) d\theta_2 d\theta_3 \dots d\theta_n. \quad (2.2)$$

In a parameter estimation analysis of gravitational-wave data, an implicit assumption is made that the gravitational-wave detector noise is stationary, Gaussian, and uncorrelated between detectors in the network. The data stream from the i -th detector in a network is then $d_i(t) = n_i(t) + s_i(t)$, where $s_i(t)$ is the gravitational waveform and $n_i(t)$ is the Gaussian detector noise. Under these assumptions, the likelihood in Eqn. 2.1 has the form [68]

$$\begin{aligned} p(\vec{d}(t)|\vec{\vartheta}, H) &= \exp \left[-\frac{1}{2} \sum_{i=1}^N \langle \tilde{n}_i(f) | \tilde{n}_i(f) \rangle \right] \\ &= \exp \left[-\frac{1}{2} \sum_{i=1}^N \left\langle \tilde{d}_i(f) - \tilde{s}_i(f, \vec{\vartheta}) | \tilde{d}_i(f) - \tilde{s}_i(f, \vec{\vartheta}) \right\rangle \right], \end{aligned} \quad (2.3)$$

where N is the number of detectors in the network. The inner product $\langle \tilde{a} | \tilde{b} \rangle$ is

$$\langle \tilde{a}_i(f) | \tilde{b}_i(f) \rangle = 4\Re \int_0^\infty \frac{\tilde{a}_i(f) \tilde{b}_i^*(f)}{S_n^{(i)}(f)} df, \quad (2.4)$$

where $S_n^{(i)}(f)$ is the power spectral density of the i -th detector’s noise. Here, $\tilde{d}_i(f)$ and $\tilde{n}_i(f)$ are the frequency-domain representations of the data and noise, obtained by a Fourier transformation of $d_i(t)$ and $n_i(t)$, respectively. The model waveform $\tilde{s}_i(f, \vec{\vartheta})$ may be computed directly in the frequency domain, or in the time domain and then Fourier transformed to the frequency domain.

2.2 Sampling

In order to explore the parameter space and produce marginalized posterior distributions for astrophysical parameters of interest we use a variety of stochastic sampling techniques. For all sampling methods though the general principle is the same.

2.2.1 Markov Chain Monte Carlo

A common sampling technique is Markov Chain Monte Carlo (MCMC) where the sampler will assemble a chain of samples drawn from the parameter space according to several rules. The first sample in the chain is drawn randomly from the prior probability density function, then at each iteration a new sample is proposed. Each proposed sample is accepted or rejected according to a tunable acceptance probability, which depends on a comparison of the likelihoods of the previous and proposed samples. If the proposed sample is accepted it is appended to the chain, otherwise the previous sample is repeated instead. The cycle then repeats and sampling proceeds until the desired stopping criteria are satisfied. Ensemble MCMC sampling, where multiple Markov chains are initialized and advanced independently, is also commonly used as a more efficient means to explore a large parameter space.

Neighboring samples in a Markov chain are not independent of one another, since the nature of the sampling technique has each sample in the chain rely on the previous sample [69]. In order to identify samples in the chain that are independent, we calculate the autocorrelation length τ_K , which is the characteristic length over which samples can be considered independent [70]. For a Markov chain X_l of length l , the autocorrelation length is

$$\tau_K = 1 + 2 \sum_{i=1}^K \hat{R}_i, \quad (2.5)$$

where K is the index of the first sample in the Markov chain satisfying $5\tau_K \leq K$. The autocorrelation function \hat{R}_i is defined as

$$\hat{R}_i = \frac{1}{l\sigma^2} \sum_{t=1}^{l-i} (X_t - \mu)(X_{t+i} - \mu), \quad (2.6)$$

where X_t are the samples of X_l between the 0-th and the t -th sample, X_{t+i} are the samples of X_l between the 0-th and the $(t+1)$ -th sample, and μ and σ^2 are the mean and variance of X_t respectively. We can then extract samples from a Markov

chain that are representative of the posterior probability density function by drawing samples from the chain spaced by an interval of the autocorrelation length [69].

An additional modification to typical MCMC sampling is to create parallel copies of each Markov chain at different “temperatures,” and advance chains of each temperature independently. Chains at a temperature T will explore a modified likelihood so that the posterior probability density function becomes

$$p_T(\vec{\vartheta}|\vec{d}(t), H) = \frac{p(\vec{d}(t)|\vec{\vartheta}, H)^{\frac{1}{T}} p(\vec{\vartheta}|H)}{p(\vec{d}(t)|H)}. \quad (2.7)$$

This modification causes the Markov chains with a higher temperature to explore an effectively flatter likelihood landscape, increasing the probability that proposed steps are accepted and thus making these chains more likely to fully explore the parameter space and potentially find largely separated modes of high likelihood. As $T \rightarrow \infty$, the posterior probability density becomes just the (normalized) prior probability density. At each iteration the position of Markov chains are swapped between temperatures using an acceptance criteria described in Ref. [71], allowing information of the likelihood across the entire parameter space to propagate among all the chains. Upon completion of the analysis, posterior samples are taken only from chains where $T = 1$, with independent samples extracted from the chains as described above.

2.2.2 Nested sampling

An alternative to MCMC sampling is “nested” sampling [72, 73, 74], which was initially designed as a means of efficiently computing the evidence but will also produce marginal posteriors as a useful byproduct. Nested sampling does not rely on chains of samples, but rather a constantly updating set of “live points.” To initialize the sampling, N_{live} samples are drawn from the prior volume and the likelihood \mathcal{L} for each is calculated. Then at each iteration i the live point with the lowest likelihood \mathcal{L}_i is dropped from the set, and a new sample is drawn with the condition $\mathcal{L} > \mathcal{L}_i$. In this way, a nested sampler will progress through nested “shells” of increasing likelihood, contracting onto any regions of high likelihood in the parameter space. The remaining prior volume X_i , defined as the fraction of the prior volume contained within an iso-likelihood contour with $\mathcal{L} = \mathcal{L}_i$, is then a monotonically decreasing sequence with

$$1 = X_0 > X_1 > \dots > X_M > 0 \quad (2.8)$$

after M iterations. The evidence \mathcal{Z} can then be numerically approximated by calculating the weighted sum over the discarded samples

$$\mathcal{Z} = \sum_{i=1}^M \mathcal{L}_i w_i, \quad (2.9)$$

where the weights w_i are determined by the quadrature method used, and adding the contribution from the set of live points

$$\mathcal{Z}_{\text{live}} = \frac{X_M}{N_{\text{live}}} \sum_{j=1}^{N_{\text{live}}} \mathcal{L}_j. \quad (2.10)$$

Upon completion of the run, every sample in the collection of discarded and live points is assigned the posterior weight [75]

$$p_j = \frac{\mathcal{L}_j w_j}{\mathcal{Z}}, \quad (2.11)$$

where j goes from 1 to $M + N_{\text{live}}$, and $w_{j>M} = X_M/N_{\text{live}}$. These posterior weights can then be used to draw posterior samples from the full sequence of sampled points in the analysis [75].

Nested sampling is preferable to an MCMC sampler when calculating evidence, as the nested sampling algorithm more efficiently explores the full parameter space. However, the nested samplers available in *PyCBC Inference* are more restrictive in the prior distributions that can be used; they draw samples from a unit interval for each source parameter in the analysis and require a transformation from this space to the desired prior probability distribution. We have also observed nested samplers will sometimes fail to produce reasonable posterior estimates for loud signals, which we discuss in more detail in the next section. In the case where the necessary prior transformation is unavailable, or when analyzing loud signals, an MCMC sampler will perform better than the nested samplers.

2.3 Practical considerations

In this section we describe specific details on the implementation of the principles of Bayesian parameter estimation for gravitational-wave astronomy. In particular, we outline the parameterized waveform models describing the binary inspiral signals that we seek to measure, and additional considerations about specific likelihood models and samplers that are used in this thesis.

2.3.1 Waveform model

The intrinsic parameters describing the gravitational wave radiated by a binary merger in its source frame include the component masses $m_{1,2}$, the three-dimensional spin vectors $\vec{s}_{1,2}$ of the compact objects [76], and the eccentricity e of the binary [77]. The “coalescence phase” ϕ describes the phase of the binary at a fiducial reference time, which is often taken to be the phase at the time of merger. For binaries containing neutron stars, additional parameters $\Lambda_{1,2}$ describe the tidal deformabilities [48, 78] of the stars which depend on the equation of state and the masses. The signal observed by a gravitational-wave detector network on Earth depends on six additional parameters: the geocentric time of arrival t_c , the luminosity distance to the binary d_L , and four Euler angles that describe the transformation of the binary’s source frame to the local frame of the detector network. These four angles are defined by the binary’s right ascension α , declination δ , polarization angle Ψ , and inclination angle ι (the angle between the line of sight and the angular momentum axis of the binary).

The binary’s gravitational-wave phasing depends at leading order on its chirp mass $\mathcal{M} = (m_1 m_2)^{3/5} (m_1 + m_2)^{-1/5}$, where m_1 and m_2 are the binary’s component masses [79]; this quantity will be most accurately measured in a gravitational-wave detection. The mass ratio $\eta = m_1 m_2 / (m_1 + m_2)^2$ enters through higher-order corrections and is less accurately measured. In this thesis, we restrict to binaries where the angular momenta $\chi_{1,2} = J_{1,2} / m_{1,2}^2$ of each compact object (often referred to as the compact object’s spins) are aligned with the orbital angular momentum vector of the binary, reducing the number of spin parameters in the waveform from six to two. We also only consider binaries in quasi-circular orbits, so $e = 0$.

The static neutron star tidal effects first enter at fifth post-Newtonian order and depend on the tidal deformability of each star Λ_i [48, 80]. The parameter Λ_i measures how much each neutron star deforms in the presence of a tidal field, and depends on the neutron star mass and equation of state implicitly through its dimensionless Love number $k_{2,i}$ and radius R_i : $\lambda_i = (2/3)k_{2,i}R_i^5$. At leading order, the tidal effects are imprinted in the gravitational-wave signal through the effective tidal deformability parameter

$$\tilde{\Lambda} = \frac{16}{13} \frac{(12q + 1)\Lambda_1 + (12 + q)q^4\Lambda_2}{(1 + q)^5}, \quad (2.12)$$

where $q = m_2/m_1 \leq 1$ is the binary’s mass ratio. We ignore the dynamic tides in this

thesis, as they do not significantly affect the waveform for the systems considered.

Given a full set of parameters $\vec{\vartheta}$ one can generate a model of a gravitational-waveform from a binary merger using a variety of methods. These methods include: full numerical solutions of the Einstein equations (see Ref. [81] and references therein), perturbation theory [82, 83], analytic models calibrated against numerical simulations [84, 85, 86, 87, 88, 89, 90], and post-Newtonian (pN) theory (see e.g. Ref. [91] and references therein).

Gravitational-wave signals consist of a superposition of harmonic modes. However, sub-dominant harmonics are too weak to be measured, and so in many cases it is sufficient to model only the dominant mode. In this case, the gravitational-wave signal has the same simple dependence on the fiducial phase ϕ in all detectors,

$$\tilde{s}_i(f, \vec{\vartheta}, \phi) = \tilde{s}_i^0(f, \vec{\vartheta}, 0)e^{i\phi}. \quad (2.13)$$

The posterior probability $p(\vec{\vartheta}|\vec{d}(t), H)$ can be analytically marginalized over ϕ for models that use this simplification [68]. If we assume a uniform prior on $\phi \in [0, 2\pi)$, then using the notation of Section 2.1 the logarithm of the marginalized posterior is

$$\begin{aligned} \log p(\vec{\vartheta}|\vec{d}(t), H) &\propto \log p(\vec{\vartheta}|H) + I_0 \left(\left| \sum_i O(\tilde{s}_i^0, \tilde{d}_i) \right| \right) \\ &\quad - \frac{1}{2} \sum_i \left[\langle \tilde{s}_i^0, \tilde{s}_i^0 \rangle - \langle \tilde{d}_i, \tilde{d}_i \rangle \right], \end{aligned} \quad (2.14)$$

where

$$\begin{aligned} \tilde{s}_i^0 &\equiv \tilde{s}_i(f, \vec{\vartheta}, \phi = 0), \\ O(\tilde{s}_i^0, \tilde{d}_i) &\equiv 4 \int_0^\infty \frac{\tilde{s}_i^*(f; \vartheta, 0)\tilde{d}_i(f)}{S_n^{(i)}(f)} df, \end{aligned}$$

and I_0 is the modified Bessel function of the first kind.

In this thesis we use the TaylorF2 [92, 93, 94, 95, 96, 97], IMRPhenomD [98, 99], and IMRPhenomD_NRTidal [98, 99, 100] waveform models. TaylorF2 is a post-Newtonian waveform model, accurate to 3.5 pN order in orbital phase, 2.0 pN order in spin–spin, quadrupole–monopole and self-spin interactions, and 3.5 pN order in spin–orbit interactions. IMRPhenomD is a phenomenological model tuned to numerical relativity data, and includes representations of each of the inspiral, merger, and ringdown portions of a signal. IMRPhenomD_NRTidal builds on the IMRPhenomD model by adding corrections to the gravitational-wave phase due to the tidal deformabilities of neutron stars. All waveforms are generated using their respective LIGO Algorithm Library [101] implementation.

2.3.2 `emcee_pt`

Several of the analyses in this thesis use the parallel-tempered MCMC sampler `emcee_pt` [102, 103]. In these analyses we found frequently that the sampler would fail to converge in a reasonable time, with the number of independent samples staying constant at around 3000 which results in a poorly sampled posterior distribution. *PyCBC Inference* allows for specifying initial distributions for the MCMC chains, as opposed to having their positions drawn randomly from the prior. We found that drawing the initial positions from Gaussian distributions for each parameter, centered near the peak of the likelihood, would result in full convergence in a reasonably short amount of time. In practice, the location of the likelihood peak can be determined by a trial run where the chains are initialized from the full prior distribution, or is known *a priori* as is the case when analyzing a simulated signal.

Another consideration for the `emcee_pt` sampler is the number of temperatures to be used in the analysis. In *PyCBC Inference* this is a tunable setting which can be specified by supplying either an integer, in which case the sampler will automatically pick the temperature spacing, or as an array of inverse-temperatures, with each inverse-temperature specified by $\beta_i = 1/T_i$. Generally, a sufficient number of temperatures, and appropriate placement of them, is an important consideration when performing analyses meant to calculate evidence, as this calculation is done via thermodynamic integration and can easily produce inaccurate results for poor choices of temperatures. However in the analyses we perform we are only concerned with measuring posterior probability distributions for various parameters of interest, and as such we found that using 3 temperatures with the sampler’s automatic spacing was sufficient.

2.3.3 `dynesty`

In Ch. 4 we use the `dynesty` nested sampler [74] for our analysis. We found that when sampling in component masses $m_{1,2}$, this sampler would sometimes struggle to explore the parameter space fully. As a result the sampler would miss regions of high likelihood, and would prematurely claim to have reached its stopping criteria. The posterior distributions in these cases would appear “patchy,” with many small, disjoint regions. We found that in many cases this problem could be avoided by

sampling in the natural mass coordinates of a gravitational-wave signal according to post-Newtonian theory, namely the chirp mass \mathcal{M} and mass ratio $q = m_1/m_2$ or symmetric mass ratio $\eta = m_1 m_2 / (m_1 + m_2)^2$. However for very loud signals, with signal-to-noise ratio $\rho \gtrsim 75$, we sometimes saw the same issue even when sampling in the natural mass coordinates. We did not find any satisfactory solution to this problem in the case of loud signals, so for these signals we recommend the use of a different sampler.

2.3.4 Long duration signals

Gravitational-wave detectors that use an L-shaped interferometer design, such as the two LIGO detectors and the Virgo detector, have the greatest sensitivity in the direction normal to the plane of the detector arms. This direction is a time-dependent quantity though, as the Earth rotates and moves along its orbit around the sun. Typical parameter estimation analyses will neglect any time-dependence in the detector sensitivity, as the duration of a signal in the sensitive frequency band of current generation detectors is only a few minutes, over which time the antenna pattern can be reasonably approximated as constant. However, third-generation detectors such as Cosmic Explorer will have good sensitivity down to much lower frequencies, which can translate into a low-mass binary inspiral signal staying in the sensitive band for an hour or longer. At this point the time-dependence of the detector antenna pattern becomes non-negligible and it is important that the template waveform used in a likelihood calculation accounts for the variation in sensitivity over its duration. Currently, the relative likelihood model in *PyCBC Inference* has an option which will apply a time-dependent detector antenna response to the template waveforms, and we use this functionality for analyses in this work that use a third-generation detector.

2.3.5 Relative likelihood

In Ch. 4 and Ch. 6 we use the relative likelihood model available in *PyCBC Inference* which uses an approximation to the likelihood near its peak in order to reduce run time [104, 46, 105]. In practice, the use of this likelihood model requires some care as the approximation it uses is not valid far from the peak of the likelihood. A specific failure mode we encountered would happen when attempting to explore a large prior

volume, which allowed sampling parameter space far from the likelihood peak. In this failure mode we would see the analysis would “run away” to erroneously large likelihoods, generally for parameter values near the boundaries of the prior volume. To prevent this failure we found that placing a mild restriction on the prior volume was broadly effective. Specifically we found that restricting the chirp mass \mathcal{M} to within $\sim 20\%$ of the expected signal would ensure proper convergence. Alternatively (or in addition) the relative likelihood model can be tuned to use more frequency bins in the likelihood calculation which we found would sometimes also prevent this failure.

Chapter 3

Measuring the Viewing Angle of GW170817 with Electromagnetic and Gravitational Waves

The joint detection of gravitational waves (GWs) and electromagnetic (EM) radiation from the binary neutron star merger GW170817 ushered in a new era of multi-messenger astronomy. Joint GW–EM observations can be used to measure the parameters of the binary with better precision than either observation alone. Here, we use joint GW–EM observations to measure the viewing angle of GW170817, the angle between the binary’s angular momentum and the line of sight. We combine a direct measurement of the distance to the host galaxy of GW170817 (NGC 4993) of 40.7 ± 2.36 Mpc with the Laser Interferometer Gravitational-wave Observatory (LIGO)/Virgo GW data and find that the viewing angle is $32_{-13}^{+10} \pm 1.7$ degrees (90% confidence, statistical, and systematic errors). We place a conservative lower limit on the viewing angle of $\geq 13^\circ$, which is robust to the choice of prior. This measurement provides a constraint on models of the prompt γ -ray and radio/X-ray afterglow emission associated with the merger; for example, it is consistent with the off-axis viewing angle inferred for a structured jet model. We provide for the first time the full posterior samples from Bayesian parameter estimation of LIGO/Virgo data to enable further analysis by the community.

3.1 Introduction

On 2017 August 17, the Advanced Laser Interferometer Gravitational-wave Observatory (LIGO) and Virgo observed the gravitational waves (GWs) from a binary neutron star merger, dubbed GW170817 [5]. This signal was followed 1.7 s later by a short gamma-ray burst (GRB), GRB170817A, detected by the *Fermi* and *INTEGRAL* satellites [22, 23]. Rapid follow-up of the LIGO/Virgo sky localization region led to the identification of an optical counterpart in the galaxy NGC 4993 [106, 33, 107], which in turn enabled multi-wavelength observations spanning from radio to X-rays.

Ultraviolet, optical, and near-infrared observations covering the first month post-merger led to the inference of a complex ejecta structure in terms of mass, velocity, and opacity (e.g., [24, 25, 26, 27, 28, 29, 30]), potentially indicative of non-spherical angular structure. Radio and X-ray observations revealed brightening emission for the first ≈ 5 months, which has been interpreted as resulting from an off-axis structured relativistic jet (e.g., [108, 109, 110, 111, 112]), or alternatively a spherical “cocoon” of mildly relativistic ejecta (e.g., [113]).

Measuring the angle between the binary’s angular momentum axis and the line of sight is important for an understanding of the engine powering the multi-wavelength electromagnetic (EM) emission from GW170817. Following [5], we define the viewing angle $\Theta = \min(\theta_{JN}, 180^\circ - \theta_{JN})$, where θ_{JN} is the angle between the binary’s total angular momentum and the line of sight [5]. For systems where the angular momentum of each compact object (the spin) is small, and precession of the binary’s orbital plane is not significant (as is the case for GW170817), $\theta_{JN} \approx \iota$, where ι is the angle between the binary’s orbital angular momentum and the line of sight (the inclination angle). There is a degeneracy between the binary’s inclination, ι , and the luminosity distance, d_L , when only LIGO/Virgo observations are used to measure the inclination angle [31]. Breaking this degeneracy with an independent distance measurement immediately allows one to place tighter constraints on the inclination angle [114].

Using GW observations alone, LIGO and Virgo constrained the viewing angle to $\Theta \leq 55^\circ$ at 90% confidence with a low-spin prior [5]. To provide an independent distance measurement, Abbott *et al.* used the estimated Hubble flow velocity for NGC 4993 of $3017 \pm 166 \text{ km s}^{-1}$ and a flat cosmology with $H_0 = 67.90 \pm 0.55 \text{ km s}^{-1} \text{ Mpc}^{-1}$ to constrain $\Theta \leq 28^\circ$ [5]. [115] used the combined H_0 -inclination posterior from

[116] in conjunction with the Dark Energy Survey measurement of $H_0 = 67.2_{-1.0}^{+1.2}$ km s⁻¹ Mpc⁻¹ [117] to infer $\Theta \leq 28^\circ$ at 90% confidence [115]. These circuitous approaches to breaking the distance-inclination degeneracy were motivated partly by the absence of a precise distance measurement to NGC 4993, as well as by the lack of a published distance-inclination posterior probability distribution. Furthermore, [115] was not able to place a strong constraint on the lower bound of Θ , as his analysis used the GW posteriors [115] and was constrained by LIGO/Virgo’s choice of prior in their GW analysis [116].

Here, we directly use the most precise distance measurement available for NGC 4993 of $d_L = 40.7 \pm 2.36$ Mpc [2] and the LIGO/Virgo GW data [5] to infer Θ directly from joint GW–EM observations using Bayesian parameter estimation [118, 119, 120]. To allow our results to be used by the community for further analysis we provide the full posterior samples from our analysis as supplemental materials.

3.2 Methods

We use Bayesian inference to measure the parameters of GW170817 [65]. We calculate the posterior probability density function, $p(\boldsymbol{\theta}|\mathbf{d}(t), H)$, for the set of parameters $\boldsymbol{\theta}$ for the GW model, H , given the LIGO Hanford, Livingston, and Virgo GW data $\mathbf{d}(t)$:

$$p(\boldsymbol{\theta}|\mathbf{d}(t), H) = \frac{p(\boldsymbol{\theta}|H)p(\mathbf{d}(t)|\boldsymbol{\theta}, H)}{p(\mathbf{d}(t)|H)}, \quad (3.1)$$

where $\boldsymbol{\theta}$ is the vector of the gravitational waveform parameters. The prior, $p(\boldsymbol{\theta}|H)$, is the set of assumed prior probability distributions for the waveform parameters. The likelihood $p(\mathbf{d}(t)|\boldsymbol{\theta}, H)$ assumes a Gaussian model of detector noise and depends upon the noise-weighted inner product between the gravitational waveform and the GW detector data $\mathbf{d}(t)$ [121, 122]. Marginalization of the likelihood to obtain the posterior probabilities is performed using Markov Chain Monte Carlo (MCMC) techniques. Our implementation used the *PyCBC Inference* software package [119, 120] and the parallel-tempered *emcee* sampler [118].

The MCMC is performed over the detector-frame chirp mass of the binary \mathcal{M}^{det} , the mass ratio $q = m_1/m_2$, $m_1 \geq m_2$, the component spins $\chi_{1,2}$, the time of coalescence t_c , the phase of coalescence ϕ_c , the GW polarization angle ψ , the inclination angle of the binary ι , R.A. and decl. of the binary, and the luminosity distance d_L .

We assume a uniform prior distribution on the binary component masses, $m_{1,2} \in [1.0, 2.0] M_\odot$, transformed to \mathcal{M}^{det} and q with a cut on the detector-frame chirp mass $1.1876 \leq \mathcal{M}^{\text{det}} \leq 1.2076$. We assume a uniform prior on the dimensionless angular momentum of each neutron star, $\chi_{1,2} \in [-0.05, 0.05]$ [123]. The prior on t_c is uniform in the GPS time interval [1187008882.3434, 1187008882.5434]. We assume a uniform prior between 0 and 2π for ϕ_c and ψ . We incorporate EM information through fixing the R.A. and decl. of GW170817 and through the prior probability distribution on the luminosity distance $p(d_L|H)$. We run the MCMC with two prior distributions on the inclination angle ι : a prior uniform in $\cos \iota$, and a prior uniform in ι to explore the posterior distribution for small viewing angles.

We use GW strain data from the Advanced LIGO and Virgo detectors for the GW170817 event, made available through the LIGO Open Science Center (LOSC) [124]. The LOSC_CLN_16_V1 data that we use here include a post-processing noise subtraction performed by the LIGO/Virgo Collaboration [125, 126]. The LOSC documentation states that these data have been truncated to remove tapering effects due to the cleaning process, however the LOSC data shows evidence of tapering after GPS time 1187008900 in the LIGO Hanford detector. To avoid any contamination of our results we do not use any data after GPS time 1187008891.

We high-pass the GW data using an eighth-order Butterworth filter that has an attenuation of 0.1 at 15 Hz. The filter is applied forward and backward to preserve the phase of the data. A low-pass (anti-aliasing) finite impulse response filter is applied prior to resampling the data. The data is decimated to a sample rate of 4096 Hz for the analysis. To estimate the detector's noise power spectral density (PSD) for computing the GW likelihood, we use Welch's method with 16-second Hann-windowed segments (overlapped by 8 s) taken from GPS time 1187007048 to 1187008680. The PSD estimate is truncated to 8 s length in the time domain using the method described in [127]. The GW data $\vec{d}(t)$ used in the likelihood is taken from the interval 1187008763 to 1187008891. The GW likelihood is evaluated from a low-frequency cutoff of 25 Hz to the Nyquist frequency of 2048 Hz.

The waveform model H is the restricted TaylorF2 post-Newtonian (pN) aligned-spin waveform model. We use the LIGO Algorithm Library implementation [101]

accurate to 3.5 pN order in orbital phase [93], 2.0 pN order in spin–spin, quadrupole–monopole and self-spin interactions [95, 94], and 3.5 pN order in spin–orbit interactions [96]. The waveforms are terminated at twice the orbital frequency of a test particle at the innermost stable circular orbit of a Schwarzschild black hole of mass $M = m_1 + m_2$. We neglect matter effects in the waveforms as we find that their effect is significantly smaller than the statistical errors on our measurement of d_L and ι .

To measure the systematic effect of calibration uncertainties we use the 68% occurrence, 1σ calibration uncertainty bounds for LIGO/Virgo’s second observing run as detailed in [128]. We adjusted the GW strain to the extreme cases of calibration error in amplitude and phase to determine the systematic effects on parameter measurement. The strain adjustment was done according to

$$\tilde{d}'(f) = \left(1 + \frac{\delta R(f)}{R(f)}\right) \tilde{d}(f) \quad (3.2)$$

where $\tilde{d}(f)$ is the frequency-domain GW strain data, $\delta R/R$ is the relative response function error (in amplitude and phase), and $\tilde{d}'(f)$ is the resulting adjusted strain data [129].

3.3 Results

As a check on our analysis, we first estimate the parameters of GW170817 using priors that do not assume any information about the source from EM observations. We allow the R.A. and decl. to vary uniformly over the entire sky, and the distance to vary in a wide uniform-in-volume distribution of [5, 80] Mpc. Our analysis localized the source to a region of $\approx 23 \text{ deg}^2$ at 90% confidence, shown in Figure 2. Our sky localization encloses the location of NGC 4993 (e.g., [33]) and agrees well with the localization region of [5].

We then fix the sky location of GW170817 to R.A. = 197.450374° , decl. = -23.381495° [33] and remove these parameters from our parameter estimation. Fixing the sky location of GW170817 has virtually no impact on the inclination measurement, in agreement with previous studies that have explored this correlation [130, 131]. Finally, we set the prior probability distribution on the luminosity distance $p(d_L|H)$ to a Gaussian distribution centered on 40.7 Mpc with a standard deviation of 2.36 Mpc, corresponding to the measured distance and quadrature sum

of statistical and systematic errors reported in [2]. Here we have assumed a Gaussian distribution on this distance measurement, which we deem valid for a measurement of this precision and for the purpose of exploring upper and lower bounds.

Using the EM observations as the prior on the luminosity distance results in significantly narrower posteriors on inclination angle and source-frame chirp mass $\mathcal{M} = (m_1 m_2)^{3/5} / (m_1 + m_2)^{1/5}$ shown in Figure 3. The improved chirp mass measurement is due to the reduced error on d_L , as the d_L posterior samples are used to convert from the measured detector-frame chirp mass \mathcal{M}^{det} to the source-frame chirp mass \mathcal{M}^{src} [132, 133]. However, the improved precision on distance has no effect on our measurements of the component masses or spins, because at leading order the mass ratio $q = m_1/m_2$ and spin parameter χ_{eff} [63] are not correlated with distance. With the EM observations as the prior on d_L and a prior on the inclination angle uniform in $\cos \iota$, we find that the viewing angle is $\Theta = 32^{+10}_{-13}$ degrees (90% confidence).

Errors in the calibration of the GW detectors can cause errors in the measured amplitude of the GW signal and hence in the inclination angle of the binary. We treat this as a systematic error, which we measure by shifting the amplitude calibration of the LIGO and Virgo detectors by the 1σ uncertainty bounds for LIGO/Virgo's second observing run [128]. We find that shifting the calibration to its most sensitive and least sensitive extremes results in a $\pm 1.7^\circ$ shift in the peak of the viewing angle when using a prior on inclination angle that is uniform in $\cos \iota$. We quote this shift as the systematic error on our measurement. Changing the phase error of the calibration within the bounds reported in [128] produces a negligible effect on the inclination angle.

A prior uniform in $\cos \iota$ goes to zero as the viewing angle approaches face on (or face off), so we repeat our analysis using a prior uniform in ι . Figure 4 shows a comparison between the prior and the posterior distributions on inclination angle for each choice of prior. The result using a prior uniform in ι excludes viewing angles $\Theta \leq 14.8^\circ$ at 90% confidence, suggesting that our likelihood is indeed informative at small viewing angles and the lack of posterior support is not due to the prior uniform in $\cos \iota$ vanishing for small angles. Including the systematic error from calibration uncertainty, we set a conservative constraint of $\Theta \geq 13^\circ$ at 90% confidence. This is consistent with the 10-day interval between the merger and the first observation of X-ray afterglow [134], which suggests that the GRB is not beamed at the Earth [135].

3.4 Discussion

Our joint GW–EM analysis of GW170817 used the GW observations along with sky location and a prior on the distance from direct measurement of these parameters from EM observations of NGC 4993. Our 90% confidence region on the viewing angle, $\Theta = 32_{-13}^{+10} \pm 1.7$ degrees (statistical and systematic errors), is significantly narrower than the inference made by GW observations alone, by about a factor of 2.6. It extends well above the $\Theta < 28^\circ$ bound of [115], which was based on an assumed Hubble flow velocity for NGC 4993. The precise distance measurement from [2] also allows us to place a 90% confidence lower bound on Θ that is substantially higher than the 68% confidence lower bound, $\Theta > 10^\circ$, reported by [115].

Our improved constraint on Θ has implications for models of the prompt γ -ray and radio/X-ray afterglow emission from GW170817. For example, our inferred value is in good agreement with the structured jet models of [110], which favor a viewing angle of $\approx 33^\circ$, and [112], which favor a viewing angle of $\approx 20^\circ$. While we do not yet know from a single event if the ejecta components that dominate the early UV/optical/near-infrared emission are significantly asymmetric, our constraint on Θ for GW170817 and future mergers will serve to shed light on the ejecta structure (e.g., spherical vs. polar vs. equatorial).

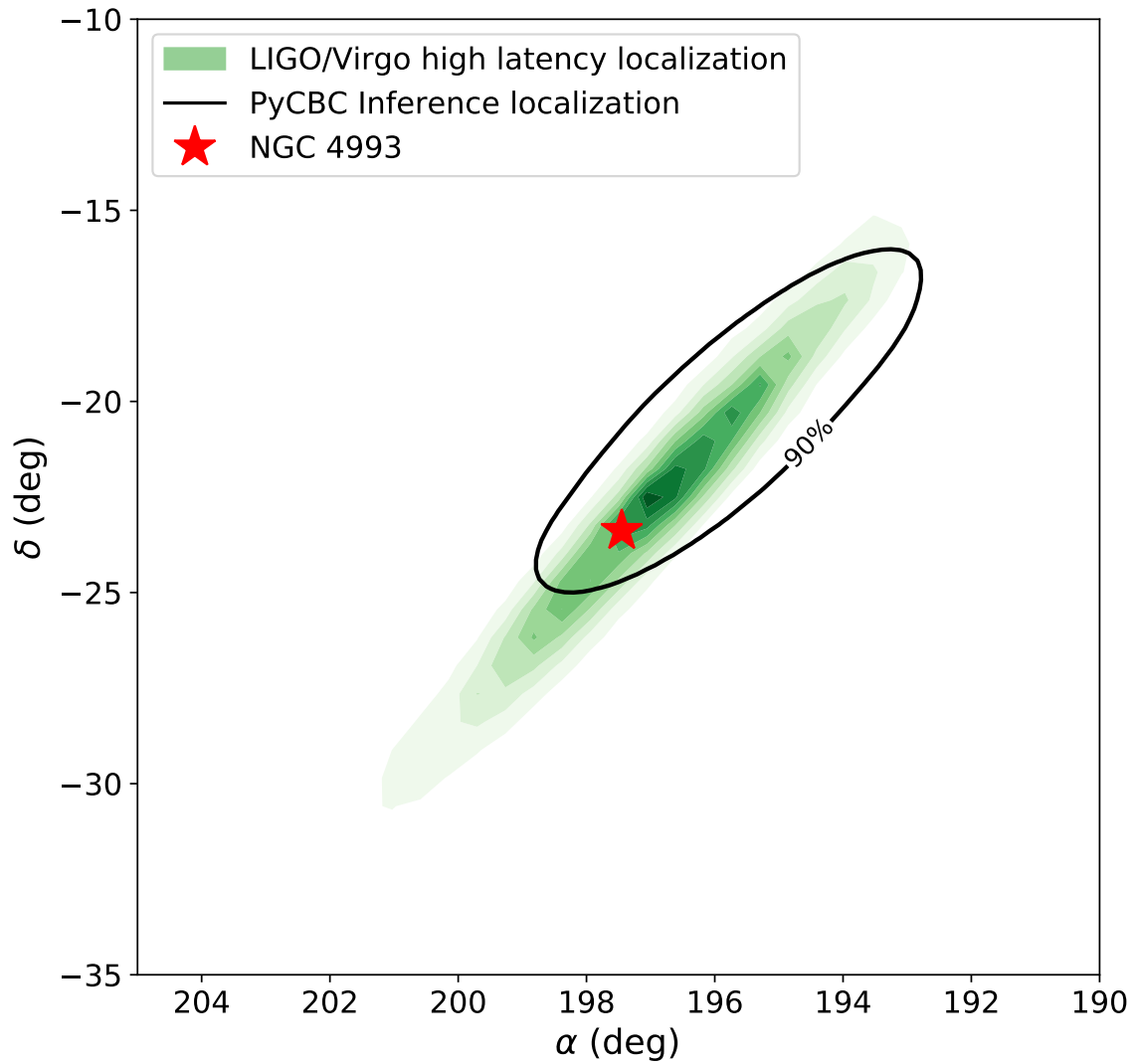


Figure 2: Sky localizations of GW170817 for LIGO/Virgo (green shaded region) and from our analysis using only GW source information (black contour). Both localizations are 90% confidence regions, while the LIGO/Virgo region shows contours at each 10% threshold. The location of NGC 4993 is marked as a red star.

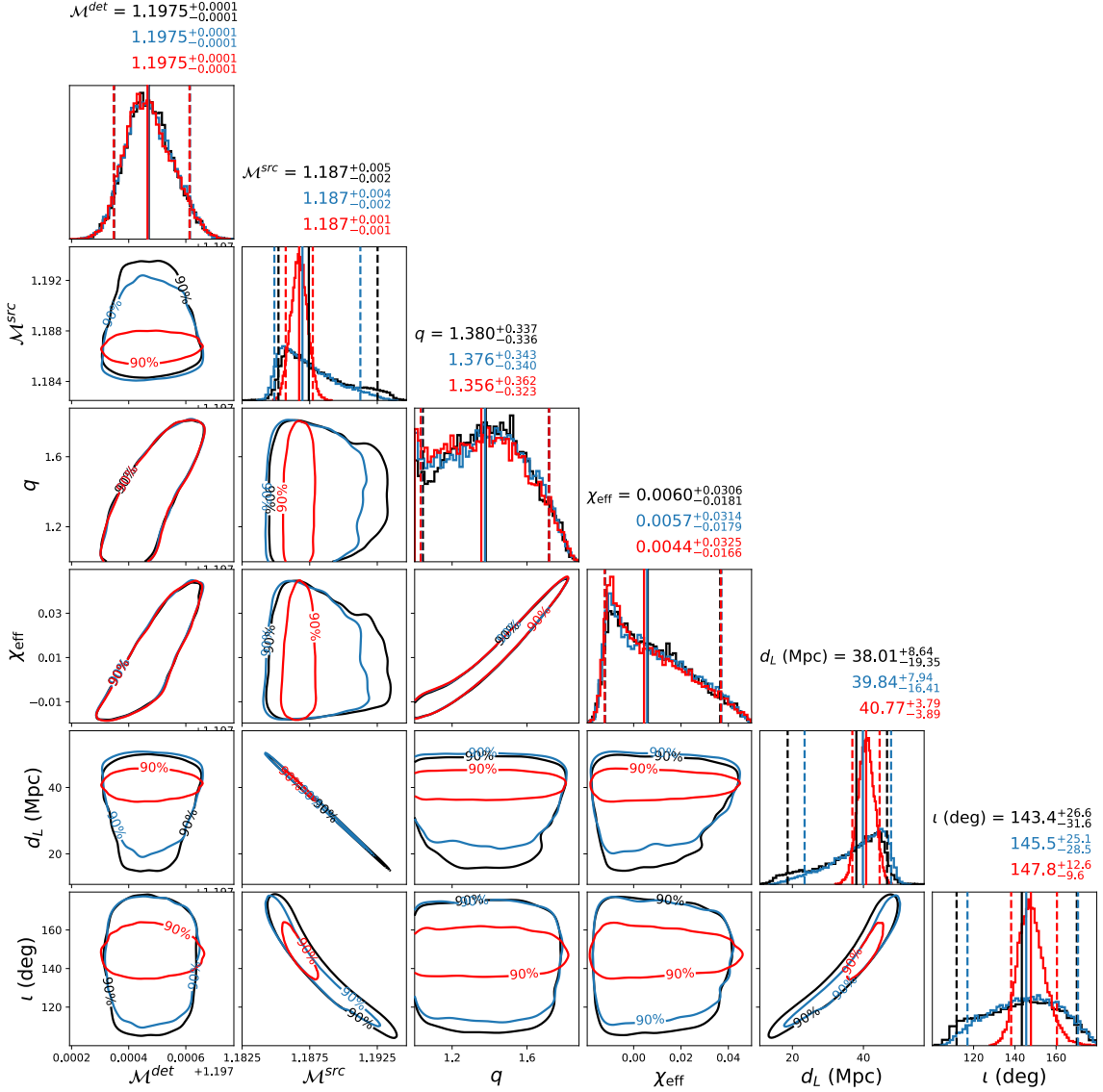


Figure 3: Comparison of posterior probability distributions without and with combined EM information. The black contours show the results for using only the GW signal, the blue contours show the results for the fixed sky location of NGC 4993, and the red contours show the results for both the fixed sky location and a Gaussian prior on distance of 40.7 ± 2.36 Mpc from [2]. These analyses used a prior on inclination angle that is uniform in $\cos \iota$. For each parameter, we quote the median value and the 90% credible interval (shown with vertical solid and dashed lines, respectively, on the posterior plot of each parameter). The EM information on the distance measurement greatly improves the precision with which we measure the inclination angle (and significantly reduces the uncertainty on the source-frame chirp mass).

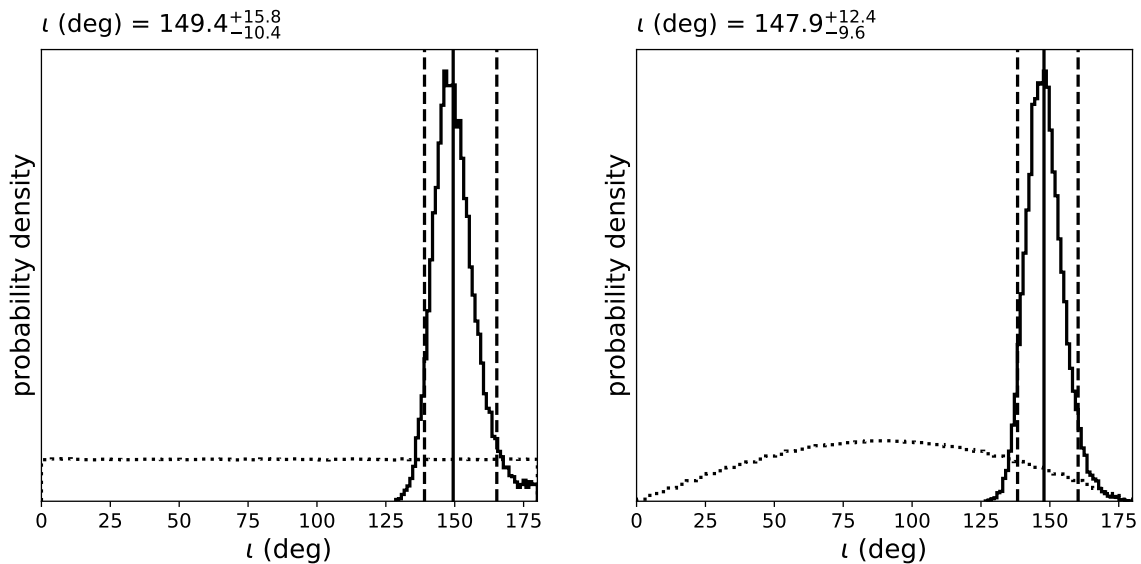


Figure 4: Inclination angle posteriors (solid lines) plotted against their prior (dotted lines) for two choices of prior: uniform in ι (left), and uniform in $\cos \iota$ (right). We quote the median value and the 90% credible interval for ι in each posterior (shown with vertical lines). The prior uniform in $\cos \iota$ is the prior used by the LIGO/Virgo analysis. The uniform prior does not bias measurement away from angles approaching 180° , so these results suggest that our likelihood is informative close to $\iota = 180^\circ$ and that we can place a conservative lower bound on the viewing angle $\Theta \geq 13^\circ$ (90% confidence).

Chapter 4

Fast Parameter Estimation of Binary Mergers for Multimessenger Followup

Significant human and observational resources have been dedicated to electromagnetic followup of gravitational-wave events detected by Advanced LIGO and Virgo. As the sensitivity of LIGO and Virgo improves, the rate of sources detected will increase. [34] have suggested that it may be necessary to prioritize observations of future events. Optimal prioritization requires a rapid measurement of a gravitational-wave event's masses and spins, as these can determine the nature of any electromagnetic emission. We extend the relative binning method of [45] and [46] to a coherent detector-network statistic. We show that the method can be seeded from the output of a matched-filter search and used in a Bayesian parameter measurement framework to produce marginalized posterior probability densities for the source's parameters within 20 minutes of detection on 32 CPU cores. We demonstrate that this algorithm produces unbiased estimates of the parameters with the same accuracy as running parameter estimation using the standard gravitational-wave likelihood. We encourage the adoption of this method in future LIGO-Virgo observing runs to allow fast dissemination of the parameters of detected events so that the observing community can make best use of its resources.

4.1 Introduction

The observation of the binary neutron star merger GW170817 in gravitational and electromagnetic waves [5, 14] has demonstrated the importance of multimessenger astronomy in answering fundamental questions in physics, astronomy, and cosmology; see e.g. [136], [137], and [116]. With the observation of GW190814, gravitational-wave astronomy has begun to explore the properties of compact objects that are more massive than previously observed neutron stars and less massive than previously observed black holes [138]. Advanced LIGO and Virgo perform a search for compact-object binary mergers with several low-latency analyses based on matched filtering [139, 140] and release alerts to the astronomical community to enable followup of detected events. As the sensitivity of the Advanced LIGO and Virgo detectors improves, the rate at which interesting events are detected will increase. [34] have suggested that it may become necessary to prioritize events for followup in future LIGO-Virgo observing runs. Optimal prioritization will require the knowledge of the source-frame component masses and spins of the binary, as these determine the type of electromagnetic counterpart that may be generated by the merger [141, 142].

In this paper, we demonstrate that it is possible to perform full Bayesian parameter estimation on binary neutron star and neutron star–black holes signals within 20 minutes of the source’s detection by a matched-filter search (with an average time of 10.8 minutes) using 32 CPU cores (2.3 GHz Xeon[®] Gold 6140). Our analysis produces marginalized posterior probability densities for the source’s parameters (including source-frame masses, spins, sky location, and distance) that can be used to guide the prioritization of electromagnetic followup in future LIGO-Virgo observing runs. We achieve this by extending the relative binning method originally introduced by [45] (and independently developed by [46]) to a fully coherent statistic, seeding the relative binning algorithm from the output of a matched-filter search, and using the *dynesty* nested-sampling package [74]. We have made our code available in the PyCBC Inference framework [35].

We validate our analysis on a population of simulated binary neutron star and neutron star–black hole signals in a LIGO-Virgo detector network. A matched-filter search is used to identify signals that have a false alarm rate better than one per month. We then use our algorithm to produce marginalized posterior probability

densities for each qualifying signal. For the parameters of interest, we perform a percentile-percentile test and demonstrate that our method produces unbiased parameter estimates. Comparing our sky localization to that of the `Bayestar` algorithm [143], we find that the 90% credible localization area improves by an average of 14 deg². We find that our analysis can recover the source-frame chirp mass to an accuracy of $\sim 5 \times 10^{-2} M_{\odot}$ for binary neutron star signals and $\sim 10^{-1} M_{\odot}$ for neutron star–black hole signals. We demonstrate that the measurement of mass ratio and spin is consistent with that of parameter estimation using the full likelihood, although these quantities are measured less accurately than the chirp mass as they enter the gravitational waveform at higher order and suffer from a partial degeneracy [63, 144]. As an example use case, we demonstrate that our method recovers essentially the same posterior probabilities for the parameters of GW170817 as the full likelihood calculation. Our method obtains marginalized posteriors for GW170817 in 20 minutes, compared to over three hours using the standard likelihood calculation.

This Letter is organized as follows: In Section 4.2 we describe our simulated search. Section 4.3 describes our parameter estimation analysis and our implementation of relative binning for a detector network. Section 4.4 present our results including analysis run times and parameter estimation accuracy. Finally, we contrast our results to current methods in Section 4.5.

4.2 Simulated Search

We simulate a three-detector network representing the LIGO Hanford, LIGO Livingston [145, 146], and Virgo [13] detectors. We generate two populations of simulated signals: 600 binary neutron star and 570 neutron star–black hole binaries. Each population is injected into a realization of 33 hours of simulated detector data, which is created by coloring Gaussian noise to the design power spectral density of each detector [9]. The simulated binary neutron star signals have their chirp mass drawn uniformly from the interval $[0.5, 3] M_{\odot}$ and mass ratio $q = m_1/m_2$ drawn uniformly from the interval $[1, 3]$, with constraints on the component masses so that $1 < m_{1,2}/M_{\odot} < 3$. The neutron star’s spins are restricted to be aligned with the orbital angular momentum and have dimensionless magnitude drawn uniformly from the interval $[-0.05, 0.05]$. The simulated neutron star–black hole signals have their

chirp mass drawn uniformly from the interval $[0.5, 7] M_\odot$ and mass ratio drawn uniformly from the interval $[1, 10]$, with constraints on the component masses so that $1 < m_{1,2}/M_\odot < 10$. Both component spins are restricted to be aligned with the orbital angular momentum, with the black hole spin dimensionless magnitude drawn uniformly from the interval $[-0.998, 0.998]$ and the neutron star spin dimensionless magnitude drawn uniformly from the interval $[-0.05, 0.05]$. This population of sources is chosen to cover the region in which it is expected that there will be neutron star disruption and an electromagnetic counterpart [142]. Each set of simulated signals is uniformly distributed in sky location and follow a uniform-in-volume distance distribution with $d_L \in [10, 300]$ Mpc for binary neutron star signals and $d_L \in [10, 500]$ Mpc for neutron star–black hole signals. This corresponds to a signal population with single-detector signal-to-noise ratios of 1 to $O(100)$. Binary neutron star signals are simulated using the TaylorF2 waveform approximant [147, 148, 149, 150]. The neutron star–black hole signals are simulated using the IMRPhenomD approximant [98, 99]. For both populations, we set the tidal deformability of the neutron stars Λ to zero, as this does not have a significant effect on the parameters we are investigating in this paper [4].

To simulate the output of the LIGO-Virgo searches, we run each set of simulated signals through the PyCBC search pipeline [151] configured to operate in a similar way to the PyCBC Live low-latency search used in the recent Advanced LIGO–Virgo observing runs [152]. This search uses matched filtering [153] with a template bank of gravitational waveforms designed to give at least a 97% match, measured by noise-weighted overlap, to any potential signal in the relevant parameter space [154, 15]. The bank is designed to catch potentially electromagnetically-bright signals, and contains 315,325 waveforms. Template waveforms have component masses spanning $[1, 30] M_\odot$ and dimensionless spin magnitudes in the range $[-1, 1]$, with the spin restricted to the direction of the orbital angular momentum. Templates in the bank are generated using the TaylorF2 approximant for signals with total mass $M = m_1 + m_2 < 4M_\odot$ [150], and with a reduced-order model of the SEOBNRv4 approximant otherwise [155]. Candidate triggers are required to be matched by the same template in at least two detectors in the network and with consistent phase, amplitude, and time of arrival given the network orientation and relative sensitivities between detectors [156]. The search pipeline provides best-fit template parameters

for every trigger and measures the trigger’s statistical significance. The significance of a trigger is determined by the time-slide method and the pipeline computes a false alarm rate for each trigger. We select the triggers that have a false alarm rate more significant than 1 per month as candidate events for parameter estimation followup. This threshold was selected to be the same as that used to release low-latency events as public alerts for electromagnetic followup in the third LIGO-Virgo observing run [157] and corresponds to a network signal-to-noise ratio of approximately 8.3. Of the total injections made, 306 binary neutron star and 253 neutron star–black hole injections satisfied this threshold.

4.3 Parameter estimation

We use *PyCBC Inference* [35] with the *dynesty* nested sampler [74] to perform Bayesian parameter estimation on candidate events from the search pipeline. In general, under the assumption of Gaussian noise characterized by a power spectrum $S(f)$, the likelihood of obtaining detector data d given the presence of a gravitational waveform $h(\theta)$ is

$$\mathcal{L}(d|\theta) \propto \exp \left[-\frac{1}{2} \langle d - h(\theta) | d - h(\theta) \rangle \right], \quad (4.1)$$

where

$$\langle a|b \rangle = 4\Re \int_{f_{\min}}^{f_{\max}} \frac{\tilde{a}^*(f)\tilde{b}(f)}{S(f)} df \quad (4.2)$$

is the noise-weighted inner product [133, 158]. In evaluating this likelihood, we can obtain estimates of the gravitational-wave parameters θ through the posterior probability distribution

$$p(\theta|d) \propto \mathcal{L}(d|\theta)p(\theta), \quad (4.3)$$

where $p(\theta)$ is the assumed prior probability distribution of the parameters. To calculate the likelihood, we use the relative binning method of [45] and [46], which uses a linear interpolation across frequency samples over which the accumulated phase difference $\delta\phi$ between a fiducial waveform and nearby waveforms is less than a tunable threshold. This effectively downsamples the number of frequency points used to compute the likelihood, thereby speeding up the parameter estimation.

The implementation of relative binning used by [46] did not incorporate a coherent

network detection statistic. We extend their method to include the extrinsic parameters which are needed to measure the sky location of an event: right ascension α , declination δ , geocentric time of coalescence t_c , inclination angle ι , and gravitational-wave polarization angle ψ . These parameters are incorporated into the likelihood by projecting each template waveform onto the individual detectors in the network. A general frequency domain waveform template h as seen by a detector can be written as

$$h(f) = F_+(\alpha, \delta, \psi)h_+(f) + F_\times(\alpha, \delta, \psi)h_\times(f) \quad (4.4)$$

where $h_{+,\times}$ are the plus and cross polarizations of the waveform, and $F_{+,\times}$ are the detector antenna responses to the two polarizations [159]. The amplitude of the individual waveform polarizations depend on the inclination angle ι [160]

$$h_+ \propto \frac{1}{2}(1 + \cos^2 \iota), \quad (4.5)$$

$$h_\times \propto \cos \iota. \quad (4.6)$$

We generate waveforms using both polarizations in order to capture this dependence. Similarly, we measure α , δ , t_c , and ψ dependence through the detector antenna responses as the orientation of the detector arms, and thus the sensitivity to the two polarizations, will change as the Earth moves. To account for coherent network timing delays, we calculate detector-specific arrival times for each template waveform using α , δ , and t_c , based on the geometry of the network with respect to the source at the time of the signal, along with the light travel time from the Earth center [161].

The relative-binned likelihood calculation requires a fiducial waveform known to be near the peak of the likelihood. The chirp mass of the template used to generate a candidate by a search pipeline is accurate to within a few $10^{-3}M_\odot$ for binary neutron star signals [162, 163] and to approximately 1% for neutron star–black hole signals [164]. Since the chirp mass is the leading order parameter governing phase evolution for a binary inspiral [79], the best-fit template will be near the peak of the likelihood. We therefore use the parameters that the search pipeline reports for a signal to generate the fiducial waveform that seeds the relative binning method. For the fiducial sky location, inclination, and polarization, we arbitrarily choose $\alpha_f = \pi$, $\delta_f = 0$, $\iota_f = 0$, and $\psi_f = \pi$, as we find that more accurate initial estimates are unnecessary to correctly recover the source parameters. The fiducial coalescence time is set to be

the arithmetic mean of the coalescence time reported by the search pipeline for each detector.

Parameter estimation is performed over the detector-frame chirp mass \mathcal{M} , the mass ratio $q = m_1/m_2$, $m_1 \geq m_2$, the component aligned spins $\chi_{1,2}$, the geocentric time of coalescence t_c , the inclination angle ι , the right ascension α , the declination δ , the luminosity distance d_L , and the gravitational-wave polarization angle ψ . The likelihood calculation includes an analytic marginalization over the coalescence phase ϕ_c . We use the TaylorF2 approximant to generate the likelihood for binary neutron star waveforms and the IMRPhenomD approximant for the neutron star–black hole waveforms. For all simulated signals we use a low-frequency cutoff of 30 Hz and a sample rate of 2048 Hz.

The prior distributions used in the parameter estimation are the same as those of the corresponding population of simulated signals for each parameter, with the exception of the chirp mass which we restrict to be uniform in $\mathcal{M} \in [\mathcal{M}_s - 0.1, \mathcal{M}_s + 0.1] M_\odot$, where \mathcal{M}_s is the chirp mass of the template reported by the search. This constraint on the chirp mass prior enables quicker convergence of the parameter estimation, but in all cases the restricted bounds are well outside the region of posterior support and so do not affect the accuracy of recovery.

For each simulated signal recovered with false alarm rate more significant than 1 per month by the search pipeline, we run the relative-binned parameter estimation analysis to produce posterior distributions for the 10-dimensional set of waveform parameters $\theta = (\mathcal{M}, q, \chi_1, \chi_2, t_c, \iota, \alpha, \delta, d_L, \psi)$. For each signal, we measure the wall-clock time that it takes to perform the parameter estimation on 32 cores of an Intel[®] Xeon[®] Gold 6140 processor running at a clock speed of 2.3 GHz.

4.4 Results

The timing results for the two simulated populations as a function of the network signal-to-noise ratio of the maximum likelihood template are shown in the left panel of Fig. 5. The average run time for a single signal is 10.8 minutes, with the maximum run-time being 20 minutes for all signals. The parallelization used by the nested sampling algorithm is saturated at approximately 32 cores, so while a small decrease in wall-clock time may be gained by fine-tuning the number of cores, increasing the

number beyond 32 does not significantly decrease the run time. Processors with a faster clock speed will generally decrease run time, however.

To determine whether our method of measuring the parameters is accurate for the population of injected signals, we perform a percentile-percentile (PP) test on each of the main parameters of interest: chirp mass \mathcal{M} , mass ratio q , effective spin $\chi_{\text{eff}} = (m_1\chi_1 + m_2\chi_2)/(m_1 + m_2)$, right ascension α , declination δ , luminosity distance d_L , and inclination ι . The PP test calculates the distribution of percentile ranks for all injected parameter values within their respective posteriors and constructs the fraction of injections recovered within a credible interval as a function of credible interval. Any deviation from uniformity in this distribution for a parameter is an indication of measurement bias. We measure any deviation with the Kolmogorov-Smirnov (KS) test [165], which computes the distance between the empirical distribution that we find for the PP test and the expected distribution. The results of the PP tests are shown in the right panel of Fig. 5. For every parameter of interest, we find that the PP test follows the ideal distribution well, with the KS test indicating that the percentile rank distributions cannot be meaningfully distinguished from uniform. Our results show that our analysis produces unbiased estimates for each of the parameters of interest.

To examine the accuracy of sky localization, we calculate the area on the sky containing 90% of the probability for the location of the source. We compare the area of this probability contour to the 90% credible interval of the sky-map produced in low-latency by the `Bayestar` algorithm [143]. Fig. 6 shows the cumulative fraction of signals recovered as a function of the 90% confidence localization area for our method and by `Bayestar`. For direct comparison to the results of [143], we calculate the cumulative fraction using all recovered signals, and the subset of the recovered signals that is detected above threshold in all three detectors. We find that the area of the 90% credible region improves by an average of 14 deg² when using the relative binning parameter estimation compared to `Bayestar`.

To examine the accuracy of parameter recovery, we calculate the difference between the median of the posterior and the known injected value for each parameter. The accuracy of chirp mass recovery in the source-frame is shown in the top panels of Fig. 7 as a function of the network signal-to-noise ratio for each recovered signal. As expected, the accuracy of recovery increases as the signal-to-noise increases. For

binary neutron star signals the difference between the median value of the chirp mass posterior and the injected value is less than $\sim 5 \times 10^{-2} M_{\odot}$ for all simulated signals. This accuracy improves by a factor of 2 for signal-to-noise greater than 20. Neutron star–black hole signals generally have larger uncertainties on their parameters and we find chirp mass residuals for these signals to be less than $10^{-1} M_{\odot}$ for signal-to-noise greater than 10 and a factor of 2 less than that for signal-to-noise greater than 20. For comparison, we show the accuracy of the source-frame chirp mass of the best-fit template from the search. The search measures the detector-frame parameters of the gravitational-wave signal, so we convert this to the source-frame by computing the redshift at the median distance reported by `Bayestar` for the candidate event. The accuracy of the best-fit chirp mass from the search is an order of magnitude worse than estimated by [163]. However, the majority of the error comes from the calculation of the source-frame chirp mass. Comparing the detector-frame chirp mass of the simulated signal to the best-fit template, we find errors of $\sim 10^{-3} M_{\odot}$. While the accuracy of the best-fit template degrades for quieter signals, using this estimate as a seed for the relative-binned analysis does not affect the recovery of the source parameters.

The middle row of Fig. 7 shows the fractional uncertainty in the chirp mass $\sigma_{\mathcal{M}}/\langle\mathcal{M}\rangle$, where $\sigma_{\mathcal{M}}$ and $\langle\mathcal{M}\rangle$ are the standard deviation and mean of the posterior distribution. By this measure we find the accuracy of our method for the binary neutron star population is comparable to that of [3]. As an additional check we also run parameter estimation using the full likelihood for a subset of the population and find that the accuracy of the relative binning method is consistent with results using the full likelihood for both binary neutron star and neutron star–black hole signals. These results show that our recovery of the chirp mass for all signals has more than sufficient accuracy to determine the expected type of electromagnetic counterpart and the possible fate of the merger remnant using the method of [34].

The gravitational-wave phase evolution is less sensitive to changes in the mass ratio and so the component masses of the binary are less well recovered than the chirp mass [63]. A degeneracy exists between the mass ratio and component spins of the binary which makes measuring the component masses and spins challenging, especially for neutron star–black hole systems [144]. The bottom row of Fig. 7 shows the accuracy of measuring the mass ratio $q = m_1/m_2$. Although the measurement

of this parameter is less accurate than that of the chirp mass, our results are again comparable to those seen by [3] and they are consistent with our comparison analysis using the full likelihood on a subset of the population. This demonstrates that the reduced accuracy is intrinsic to the measurability of the parameter and not a result of using the relative binning algorithm.

To further illustrate the utility of our method in recovering parameters of interest to the observing community, Fig. 8 shows the source-frame component mass residuals for all signals as well as the black hole spin residuals for the neutron star–black hole signals, plotted as a function of the network signal-to-noise ratio. The binary neutron star component masses are shown in the left panels of the figure. The residuals on the primary mass are generally less than about $0.5M_{\odot}$ with only a slight tendency to smaller values as signal-to-noise increases. The secondary mass residuals are somewhat smaller, less than about $0.3M_{\odot}$, which can be attributed to the relatively narrow mass parameter space ($1 - 3M_{\odot}$) and our convention requiring $m_2 < m_1$.

Neutron star–black hole signals have larger uncertainties on their intrinsic parameter estimates owing to the larger mass and spin parameter space and the known degeneracy between mass ratio and spin [144]. However, these quantities are important in determining whether a merger will produce an electromagnetic counterpart. The residuals on component masses and black hole spin for our neutron star–black hole signals are shown in the right panels of Fig. 8. We find the primary and secondary mass residuals are mostly less than $3M_{\odot}$ and $1M_{\odot}$, respectively. Our estimates of the black hole spin are generally uninformative below a signal-to-noise of 20, but above this threshold we find the residuals are constrained to be less than ~ 0.3 .

As a final example of the effectiveness of our method, we apply it to GW170817 [5] without including any prior knowledge of host galaxy location or distance. For comparison, we also repeat the analysis using a standard non-relative likelihood, and the posteriors from both runs are shown in Fig. 9. For all measured parameters, we find the posterior distributions from the relative and non-relative analyses are nearly identical, in agreement with [166]. However, the analysis using the relative binning likelihood seeded by a search took only 20 minutes to complete, as compared to over 3 hours for the standard likelihood computation. In the only confirmed observation of a multimessenger gravitational-wave source to date, our analysis is able to provide the same localization region as the standard likelihood as well as the same intrinsic

parameter estimates in substantially less computational time.

4.5 Conclusion

In previous LIGO-Virgo observing runs, the information provided in low-latency to astronomers consisted of the time of the signal, an estimate of its statistical significance (false alarm rate), and a three-dimensional localization probability in sky location and distance. In the recent third observing run, two additional classifications were released that bin events into one of five broad categories (binary neutron star, binary black hole, neutron star–black hole, mass gap, or terrestrial noise) and estimate the probability that the event produced an electromagnetic counterpart [167, 164]. Both of these methods are based on the parameters of the best-fit matched filter template recorded by the low-latency search. [163] performed a template-bank simulation that estimated that the low-latency chirp mass point estimate for binary neutron stars is accurate to $\sim 10^{-3} M_{\odot}$, however they note that there can be significant bias in mass ratio and effective spin from the best-fit template. [164] demonstrated that the best-fit chirp mass from a search can be used to inform a classification scheme in which the classifications are correct in a large majority of cases.

Here, we have extended the relative binning algorithm [45, 46] for fast likelihood evaluation in gravitational-wave parameter estimation to a fully coherent detector network and demonstrated that it can be seeded by the output of a matched-filter search. We have applied our method to a set of 559 simulated signals (306 binary neutron star and 253 neutron star–black hole binaries) as well as to GW170817. We find that in all cases our method produces unbiased estimates for all measured parameters in less than 20 minutes. We have shown that our method is capable of producing full posterior distributions for all signal parameters, which do not suffer from the biases seen when attempting to measure the mass ratio and spin from the best-fit template. In the case of GW170817, the relative-binned analysis produces results nearly identical to those from a standard analysis using the full likelihood, emphasizing our method’s utility in producing fast parameter estimates that are of particular interest for electromagnetic followup.

For gravitational-wave events in LIGO’s third observing run, the average time between an initial trigger alert and the first Bayesian parameter estimation results

being made available was about 10 hours (although only updated sky maps are released and not measurement of the source's parameters). We have demonstrated our method could reduce this delay time considerably, which would allow for electromagnetic followup campaigns to be conducted more efficiently. We encourage the LIGO Scientific and Virgo collaborations to adopt these methods to provide the observing community with fast and accurate estimates of the parameters of detected signals so that these can be used to inform and prioritize electromagnetic followup strategies. Finally, we note that given the computational cost, very few large scale injection studies of low-mass gravitational-wave signals have been done. Our implementation of the relative binning method into *PyCBC Inference* brings these sorts of studies within reach for even modestly equipped computing facilities.

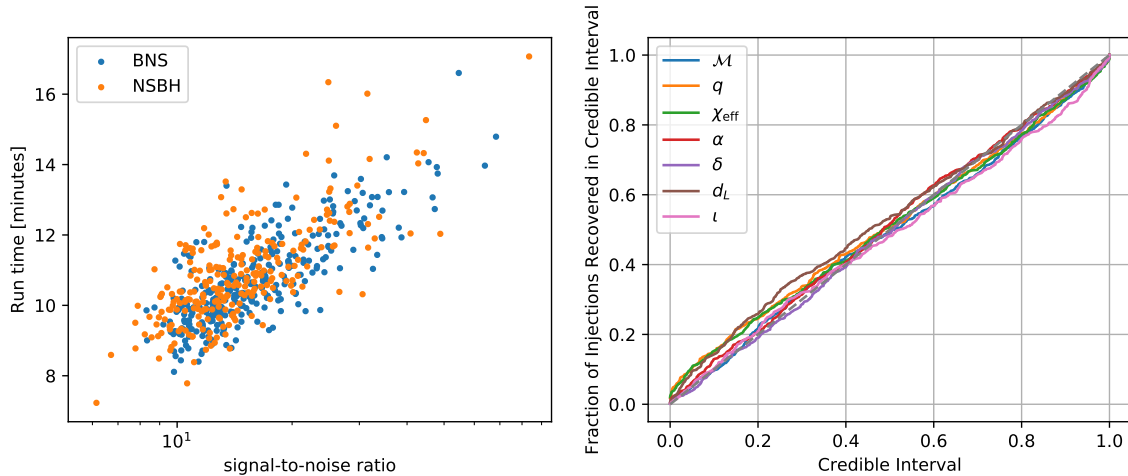


Figure 5: *Left*: The wall-clock time in minutes that it takes to perform the parameter estimation using the coherent relative binning likelihood and nested sampling on 32 cores of an Intel[®] Xeon[®] Gold 6140 processor running at a clock speed of 2.3 GHz as a function of the network signal-to-noise ratio of the maximum likelihood template. The average run-time for a single signal is 10.8 minutes, with the maximum run-time being 20 minutes for all signals. Increasing the number of cores does not significantly decrease the wall-clock run-time. The run-time shows a slight increase as a function of the signal-to-noise ratio, as expected given that signals with a larger signal-to-noise ratio have a more narrowly peaked likelihood. *Right*: The fraction of injections recovered within a credible interval plotted as a function of credible interval. Fidelity to the 1:1 diagonal line is an indication of probability being uniformly distributed across a given parameter’s posterior distribution and is a measure of the accuracy of this analysis at the population level. We find that all of the parameters of interest are estimated in an unbiased way by our parameter estimation method.

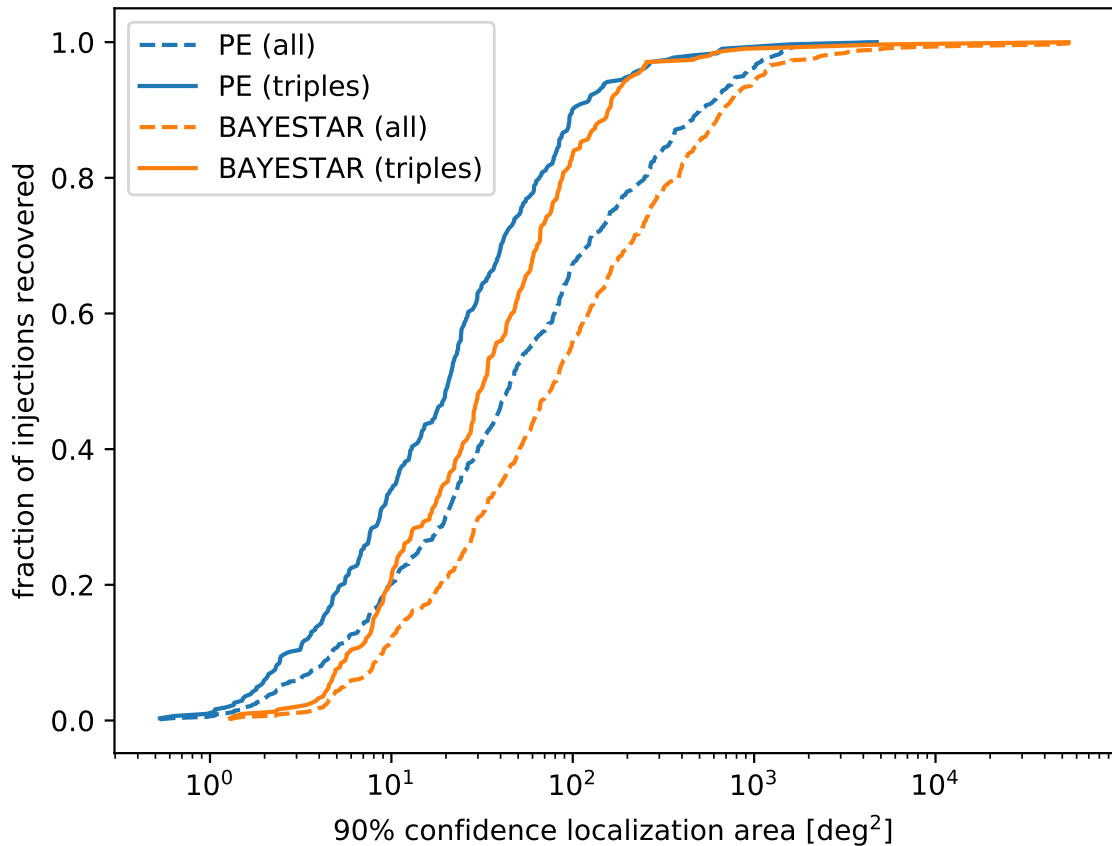


Figure 6: Fraction of injections recovered as a function of the 90% confidence localization area. The localization results from our parameter estimation analysis are shown in blue, and those from the *Bayestar* algorithm are in orange. The dotted lines show the results for the entire set of signals, while solid lines show only signals that were above the detection threshold in all three detectors in our simulated search. We find our localization areas are consistently smaller than those from *Bayestar*, as indicated by the blue lines lying to the left of the orange lines, although the difference in areas is not large. The improvement in localization area between *Bayestar* and our analysis is 14 deg² on average, and is comparable between the set of triple-coincident signals and the set of all signals.

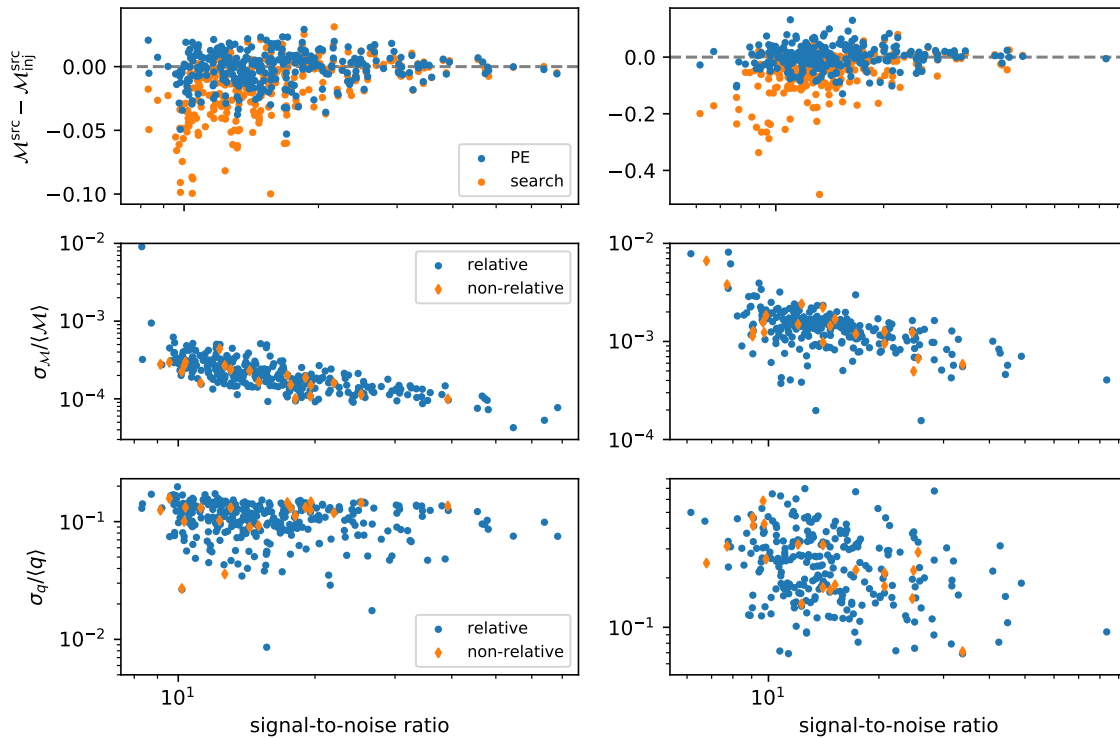


Figure 7: Chirp mass and mass ratio recovery metrics for the binary neutron star (left column) and neutron star–black hole (right column) signals in our analysis. *Top row*: Difference between source-frame chirp mass estimates and the true injected value, as a function of signal-to-noise ratio. Blue circles denote differences from the median posterior values from parameter estimation, while orange circles show differences from best-fit template values from the search. We find that on average our parameter estimation results improve on the accuracy of the best-fit template by a factor of 2. *Middle and bottom rows*: Fractional uncertainties on chirp mass and mass ratio, respectively, calculated as the ratio of standard deviation and mean of the posterior distributions. Uncertainties from our relative-binned analysis are shown as blue circles, and those from a standard non-relative likelihood analysis on a subset of the population are shown as orange diamonds. Our relative-binned results are consistent with the non-relative analysis, and also with the results in [3].

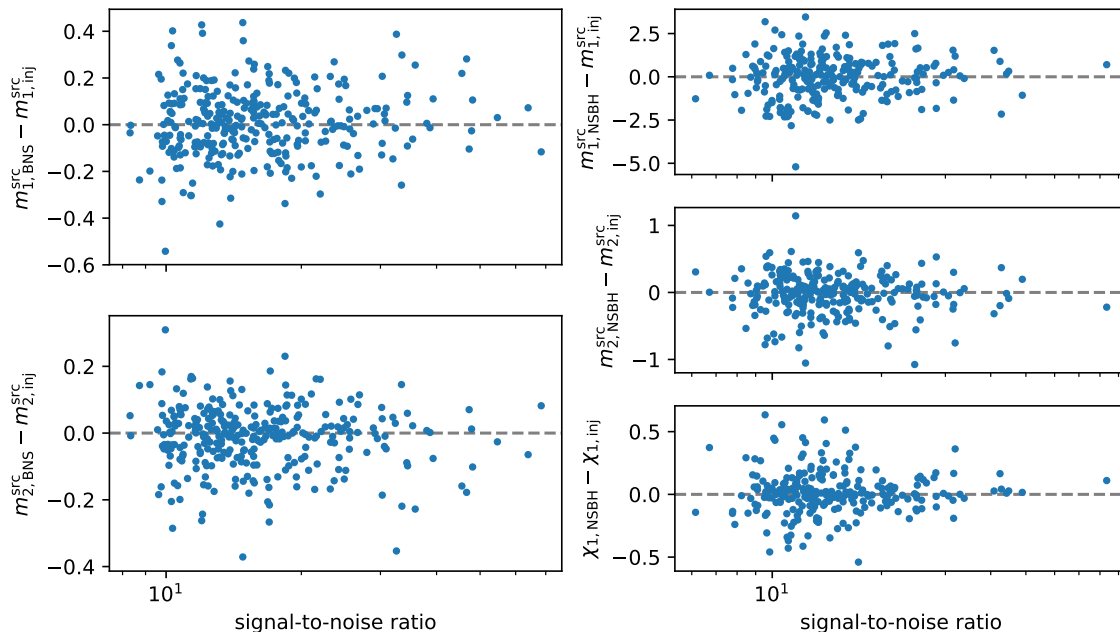


Figure 8: Difference between parameter estimates and true injected values for some component parameters of interest, plotted against signal-to-noise ratio. The left column shows results for the component masses of binary neutron star signals, and the right column shows results for the component masses and black hole spin of neutron star–black hole signals. Differences are computed from median posterior values, and masses have been converted to the source-frame using the distance posteriors. We find both component masses of binary neutron star signals are generally constrained to within $\sim 0.5M_{\odot}$ of the true value for all signals, while the majority of primary and secondary masses of neutron star–black hole signals are within about $3M_{\odot}$ and $1M_{\odot}$ respectively. We find our black hole spin measurements are uninformative below a signal-to-noise of 20, but for louder signals the spin is within about 0.3 of the true value.

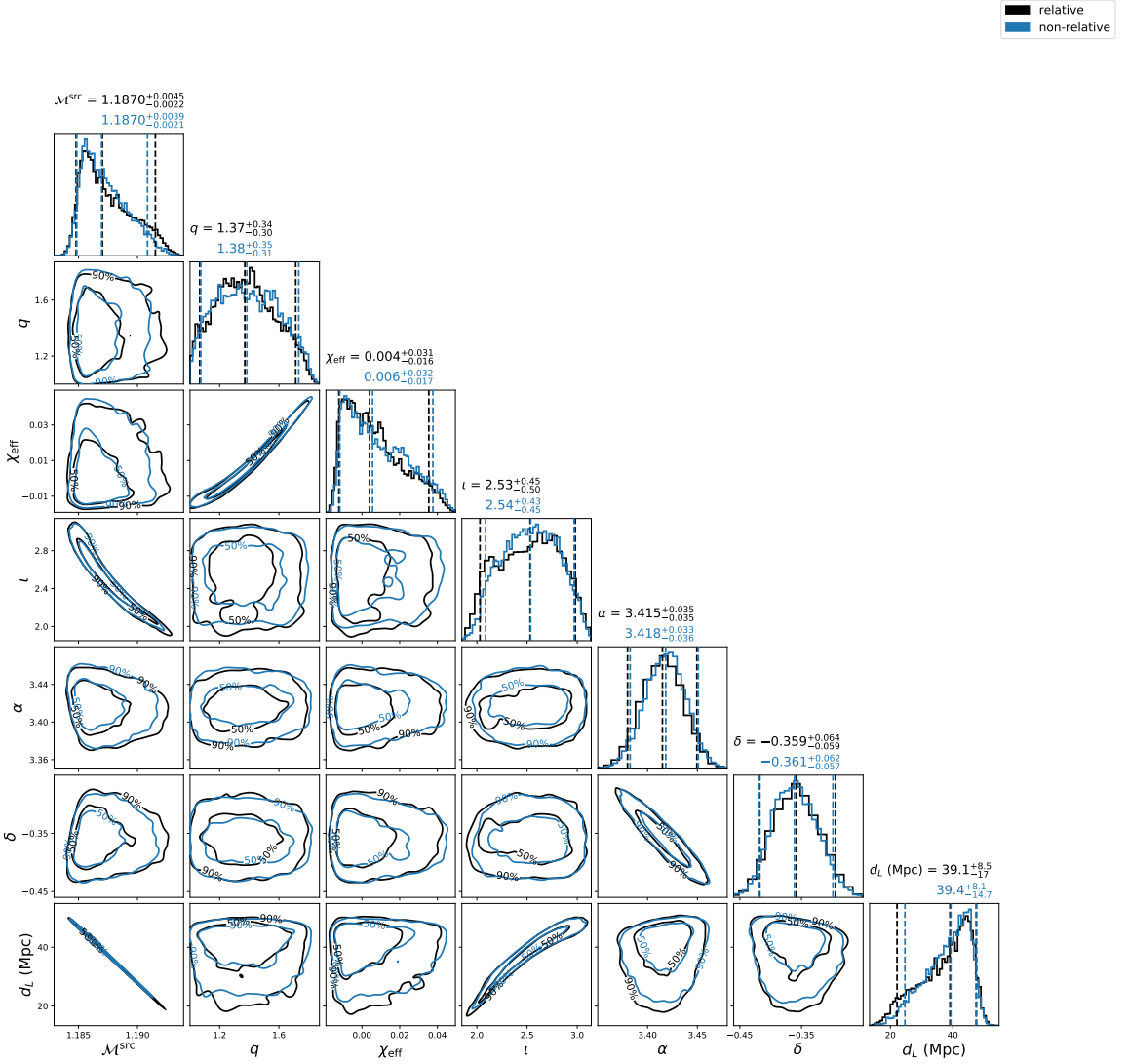


Figure 9: Posterior distributions from a relative-binned parameter estimation analysis of GW170817 (black contour) as compared to a run using the standard non-relative likelihood (blue contour). Marginalized 1-dimensional histograms for each parameter are shown along the diagonal, with vertical dashed lines at the median value and the bounds of the 90% credible interval. Off-diagonal plots show 2-dimensional slices of the parameter space with contours delineating the 50% and 90% credible regions. The relative-binned analysis completed in 20 minutes versus roughly 3 hours in the non-relative case, and all parameter distributions are consistent between the two analyses.

Chapter 5

Tidal Deformabilities and Radii of Neutron Stars from the Observation of GW170817

We use gravitational-wave observations of the binary neutron star merger GW170817 to explore the tidal deformabilities and radii of neutron stars. We perform Bayesian parameter estimation with the source location and distance informed by electromagnetic observations. We also assume that the two stars have the same equation of state; we demonstrate that for stars with masses comparable to the component masses of GW170817, this is effectively implemented by assuming that the stars' dimensionless tidal deformabilities are determined by the binary's mass ratio q by $\Lambda_1/\Lambda_2 = q^6$. We investigate different choices of prior on the component masses of the neutron stars. We find that the tidal deformability and 90% credible interval is $\tilde{\Lambda} = 222_{-138}^{+420}$ for a uniform component mass prior, $\tilde{\Lambda} = 245_{-151}^{+453}$ for a component mass prior informed by radio observations of Galactic double neutron stars, and $\tilde{\Lambda} = 233_{-144}^{+448}$ for a component mass prior informed by radio pulsars. We find a robust measurement of the common areal radius of the neutron stars across all mass priors of $8.9 \leq \hat{R} \leq 13.2$ km, with a mean value of $\langle \hat{R} \rangle = 10.8$ km. Our results are the first measurement of tidal deformability with a physical constraint on the star's equation of state and place the first lower bounds on the deformability and areal radii of neutron stars using gravitational waves.

5.1 Introduction

On August 17, 2017 LIGO and Virgo observed gravitational waves from a binary neutron star coalescence, GW170817 [5]. This observation can be used to explore the equation of state (EOS) of matter at super-nuclear densities [160, 168]. This information is encoded as a change in gravitational-wave phase evolution caused by the tidal deformation of the neutron stars [48]. At leading order, the tidal effects are imprinted in the gravitational-wave signal through the binary tidal deformability [48, 78]

$$\tilde{\Lambda} = \frac{16}{13} \frac{(12q + 1)\Lambda_1 + (12 + q)q^4\Lambda_2}{(1 + q)^5}, \quad (5.1)$$

where $q = m_2/m_1 \leq 1$ is the binary's mass ratio [cf. Eq. (34) of Ref. [169]]. The deformability of each star is

$$\Lambda_{1,2} = \frac{2}{3} k_2 \left(\frac{R_{1,2} c^2}{G m_{1,2}} \right)^5, \quad (5.2)$$

where k_2 is the tidal Love number [48, 78], which depends on the star's mass and the EOS. $R_{1,2}$ and $m_{1,2}$ are the areal radii and masses of the neutron stars, respectively.

In the results of Ref. [5], the priors on $\Lambda_{1,2}$ are taken to be completely uncorrelated, which is equivalent to assuming that each star may have a different EOS. Here, we reanalyze the gravitational-wave data using Bayesian inference [35, 170, 118] to measure the tidal deformability, using a correlation between Λ_1 and Λ_2 which follows from the assumption that both stars have the same EOS. We repeat our analysis without the common EOS constraint and calculate the Bayes factor that compares the evidences for these two models. We also fix the sky position and distance from electromagnetic observations [33, 2]. We study the effect of the prior for the component masses by performing analyses with three different priors: the first is uniform between 1 and $2M_\odot$, the second is informed by radio observations of double neutron star binaries, and the third is informed by the masses of isolated pulsars [6].

5.2 The common equation of state constraint

To explore imposing a common EOS constraint, we employ a piecewise polytrope scheme [171] to simulate thousands of equations of state. Each EOS obeys causality, connects at low densities to the well-known EOS of neutron star crusts [172], is

constrained by experimental and theoretical studies of the symmetry properties of matter near the nuclear saturation density, and satisfies the observational constraint for the maximum mass of a neutron star, $m_{\text{max}} \geq 2M_{\odot}$ [173]. Figure 10 shows the results of Tolman-Oppenheimer-Volkoff (TOV) integrations [174, 175] to determine Λ as functions of m , R , and the EOS. Each configuration is color coded according to its radius. In the relevant mass range, Λ generally varies as m^{-6} . For a given mass m , there is an inherent spread of about a factor of ten in Λ , which is correlated with R^6 . We find that the star's tidal deformability is related to its compactness parameter $\beta = Gm/(Rc^2)$ by the relation $\Lambda \simeq a\beta^{-6}$. We find that $a = 0.0093 \pm 0.0007$ bounds this relation if $1.1M_{\odot} \leq m \leq 1.6M_{\odot}$ (note that this is a bound, not a confidence interval). The additional power of β^{-1} in the $\Lambda - \beta$ relation, relative to β^{-5} in Eq. (5.2), originates because the dimensionless tidal Love number, k_2 , varies roughly as β^{-1} for masses $\geq 1M_{\odot}$, although this is not the case for all masses [175]. For $m \rightarrow 0$ we see that $k_2 \rightarrow 0$ so that k_2 is proportional to β with a positive power, but since neutron stars with $m < 1M_{\odot}$ are physically unrealistic, that domain is not pertinent to this Letter.

We observed that, for nearly every specific EOS, the range of stellar radii in the mass range of interest for GW170817 is typically small. As long as $m_{\text{max}} \geq 2M_{\odot}$, the piecewise polytrope study reveals $\langle \Delta R \rangle = -0.070$ km and $\sqrt{\langle (\Delta R)^2 \rangle} = 0.11$ km, where $\Delta R \equiv R_{1.6} - R_{1.1}$ with $R_{1.1,1.6}$ the radii of stars with $m = 1.1$ and $m = 1.6M_{\odot}$, respectively. Therefore, for masses relevant for GW170817, each EOS assigns a common value of \hat{R} to stellar radii with little sensitivity to the mass. We can combine the relations $\Lambda \simeq a\beta^{-6}$ and $R_1 = R_2$ to find the simple prescription $\Lambda_1 = q^6\Lambda_2$. We impose the common EOS constraint in our analysis using this relation. The exponent of q changes with chirp mass \mathcal{M} and for $\mathcal{M} > 1.5M_{\odot}$ this relation has to be modified. However, this is not relevant for the study of GW170817.

5.3 Implications for the neutron star radius

The common EOS constraint allows us to show that the binary tidal deformability $\tilde{\Lambda}$ is essentially a function of the chirp mass \mathcal{M} , the common radius \hat{R} , and the mass ratio q , but that its dependence on q is very weak. Substituting the expressions

$\Lambda \simeq a\beta^{-6}$ and $R = \hat{R}$ into Eq. (5.1), we find

$$\tilde{\Lambda} = \frac{16a}{13} \left(\frac{\hat{R}c^2}{G\mathcal{M}} \right)^6 f(q). \quad (5.3)$$

where $f(q)$ is very weakly dependent on q :

$$f(q) = q^{8/5}(12 - 11q + 12q^2)(1 + q)^{-26/5}. \quad (5.4)$$

For example, if we compare a binary with $q = 0.75$ to an equal mass binary, we find $f(0.75)/f(1) = 1.021$. As long as $q \geq 0.6$, valid for $1M_\odot \leq m \leq 1.6M_\odot$ for both stars, we infer from Eq. (5.3),

$$\tilde{\Lambda} = a' \left(\frac{\hat{R}c^2}{G\mathcal{M}} \right)^6, \quad (5.5)$$

where $a' = 0.0042 \pm 0.0004$. For stars with masses comparable to GW170817, the common radius \hat{R} can be found from the inversion of Eq. (5.5),

$$\hat{R} \simeq R_{1.4} \simeq (11.2 \pm 0.2) \frac{\mathcal{M}}{M_\odot} \left(\frac{\tilde{\Lambda}}{800} \right)^{1/6} \text{ km}. \quad (5.6)$$

The quoted errors originate from the uncertainties in a and q , and amount, in total, to 2%.

5.4 Parameter estimation methods

We use Bayesian inference to measure the parameters of GW170817 [65]. We calculate the posterior probability density function, $p(\vec{\theta}|\vec{d}(t), H)$, for the set of parameters $\vec{\theta}$ for the gravitational-waveform model, H , given the LIGO Hanford, LIGO Livingston, and Virgo data $\vec{d}(t)$ [124, 125]

$$p(\vec{\theta}|\vec{d}(t), H) = \frac{p(\vec{\theta}|H)p(\vec{d}(t)|\vec{\theta}, H)}{p(\vec{d}(t)|H)}. \quad (5.7)$$

The prior, $p(\vec{\theta}|H)$, is the set of assumed probability distributions for the waveform parameters. The likelihood $p(\vec{d}(t)|\vec{\theta}, H)$ assumes a Gaussian model for the detector noise [122]. Marginalization of the likelihood to obtain the posterior probabilities is

performed using Markov Chain Monte Carlo (MCMC) techniques using the *PyCBC Inference* software [35, 170] and the parallel-tempered *emcee* sampler [118, 71, 176]. We fix the sky location and distance to GW170817 [33, 2] and calculate the posterior probabilities for the remaining source parameters. Following Ref. [5], the waveform model H is the restricted TaylorF2 post-Newtonian aligned-spin model [92, 93, 94, 95, 96, 97].

To implement the common EOS constraint we construct the priors on $\Lambda_{1,2}$ according to

$$\Lambda_1 = q^3 \Lambda_s, \quad \Lambda_2 = q^{-3} \Lambda_s, \quad (5.8)$$

where $\Lambda_s \sim U[0, 5000]$. We discard draws with $\tilde{\Lambda} > 5000$, since these values are beyond the range of all plausible EOS. The resulting prior on $\tilde{\Lambda}$ is uniform between 0 and 5000. We also perform analyses that do not assume the common EOS constraint where we allow completely uncorrelated priors for $\Lambda_{1,2}$. This allows us to compare the evidences between these hypotheses. For the uncorrelated $\Lambda_{1,2}$ analyses, the prior for $\Lambda_1 \sim U[0, 1000]$ and $\Lambda_2 \sim U[0, 5000]$ with these intervals set by the range of plausible equations of state in the mass range of interest, our convention of $m_1 \geq m_2$, and discarding draws with $\tilde{\Lambda} > 5000$.

The choice of mass prior can have an impact on the recovery of the tidal deformability [58]. To investigate this, we carry out our parameter estimation analyses using three different priors on the binary's component masses. First, we assume a uniform prior on each star's mass, with $m_{1,2} \sim U[1, 2] M_\odot$. Then, we assume a Gaussian prior on the component masses $m_{1,2} \sim N(\mu = 1.33, \sigma = 0.09) M_\odot$, which is a fit to masses of neutron stars observed in double neutron star systems [6]. The third prior assumes that the component masses are drawn from a fit to the observed mass distributions of recycled and slow pulsars in the Galaxy with $m_1 \sim N(\mu = 1.54, \sigma = 0.23) M_\odot$ and $m_2 \sim N(\mu = 1.49, \sigma = 0.19) M_\odot$ [6]. We impose the constraint $m_1 \geq m_2$ which leads to $\Lambda_2 \geq \Lambda_1$. For all our analyses, the prior on the component spins is $\chi_{1,2} \sim U[-0.05, 0.05]$, consistent with the expected spins of field binaries when they enter the LIGO-Virgo sensitive band [123].

To measure the source parameters for GW170817, we performed parameter estimation on the Advanced LIGO-Virgo data available at the LIGO Open Science Center [124, 125]. Our analysis was performed with the *PyCBC Inference* software [35, 170] and the parallel-tempered *emcee* sampler [118, 71] for sampling over the

parameter space using Markov Chain Monte Carlo (MCMC) techniques [176].

The LIGO data files include a post-processing noise subtraction performed by the LIGO-Virgo Collaboration [125, 126]. The LIGO documentation states that these data have been truncated to remove tapering effects due to the cleaning process [125], however the LIGO data shows evidence of tapering after GPS time 1187008900 in the LIGO Hanford detector. To avoid any contamination of our results we do not use any data after GPS time 1187008891. The power spectral density (PSD) used to construct the likelihood was calculated using Welch’s method [177] with 16 second Hann-windowed segments (overlapped by 8 s) taken from GPS time 1187007048 to 1187008680. The PSD estimate is truncated to 8 s length in the time domain using the method described in Ref. [127]. The gravitational-wave data used in the likelihood is taken from the interval 1187008691 to 1187008891.

Ref. [178] found that choice of the low-frequency cutoff can have an effect on the measurement of the neutron star tidal deformability and used a different power spectral density estimation technique to that used in our analysis [179]. We investigated the effect of changing our estimate of the power spectral density with the power spectral density released as supplemental materials to Ref. [178]. We find that the change in parameter measurements is smaller than the statistical errors, and conclude that the choice of power spectral density estimation technique does not affect our results. To investigate the choice of low-frequency cutoff, we computed the measurabilities of the chirp mass \mathcal{M} , signal-to-noise ratio ρ , and binary deformability $\tilde{\Lambda}$ in the frequency range 10-2000 Hz. These are defined as the integrand as a function of frequency of the noise moment integrals I_{10} , I_0 , and I_{-10} (see Ref. [4]) and shown in Fig. 12. It can be seen that the signal-to-noise ratio is non-zero down to a frequency of ~ 20 Hz for all the three detectors. While detector sensitivity at this frequency does not affect the measurability of $\tilde{\Lambda}$, it does affect the measurability of the chirp mass \mathcal{M} . We repeated our analyses at 25 Hz, 23 Hz, and 20 Hz, and found an improvement in the \mathcal{M} measurement when extending until the low-frequency cutoff was 20 Hz. Consequently, we evaluated the likelihood from a low-frequency cutoff of 20 Hz to the Nyquist frequency of 2048 Hz. The improved measurement of \mathcal{M} eliminates regions of higher $\tilde{\Lambda}$ values from the posterior probability densities, and hence better constrains the measurement of this parameter, as shown in Fig 15.

The templates for the waveforms used in our parameter estimation analysis are

generated using the restricted TaylorF2 waveform model, a Fourier domain waveform model generated using stationary phase approximation. We use the implementation from the LIGO Algorithm Library (LAL) [101] accurate to 3.5 post-Newtonian (pN) order in orbital phase [93], 2.0 pN order in spin-spin, quadrupole-monopole and self-spin interactions [94, 95], and 3.5 pN order in spin-orbit interactions [96]. The tidal corrections enter at the 5 pN and 6 pN orders [97]. The waveforms are terminated at twice the orbital frequency of a test particle at the innermost stable circular orbit of a Schwarzschild black hole of mass $M = m_1 + m_2$, where $m_{1,2}$ are the masses of the binary's component stars. The TaylorF2 model assumes that the spins of the neutron stars are aligned with the orbital angular momentum. Binary neutron stars formed in the field are expected to have small spins, and precession of the binary's orbital plane is not significant [123].

We fix the sky location of the binary to the right ascension $RA = 197.450374^\circ$ and declination $Dec = -23.381495^\circ$ [33] for all of our runs. We also fix the luminosity distance of NGC 4993 $d_L = 40.7$ Mpc [2]. The small error in the known distance of NGC 4993 produces errors that are much smaller than the errors in measuring the tidal deformability. We have checked that including the uncertainty in the distance error does not affect our conclusions of the tidal deformabilities or radius. The MCMC computes the marginalized posterior probabilities for the remaining source parameters: chirp mass \mathcal{M} , mass ratio q , the component (aligned) spins $\chi_{1,2} = cJ_{1,2}/Gm_{1,2}^2$, component tidal deformabilities $\Lambda_{1,2}$, polarization angle ψ , inclination angle ι , coalescence phase ϕ_c , and coalescence time t_c . When generating the waveform in the MCMC, each $m_{1,2}$ draw follows the constraint $m_1 \geq m_2$, and the masses are transformed to the detector frame chirp mass \mathcal{M}^{det} and q with a restriction $1.1876 \leq \mathcal{M}^{\text{det}} \leq 1.2076$.

For direct comparison with the results of Ref. [5], Fig 13 shows the posterior probability densities for $\Lambda_{1,2}$ for an MCMC using a 30 Hz low-frequency cutoff for the uniform component mass prior $m_{1,2} \sim U[1, 2] M_\odot$, and assuming that the priors on $\Lambda_{1,2}$ are completely uncorrelated ($\Lambda_{1,2} \sim U[0, 3000]$). No cut is placed on $\tilde{\Lambda}$ in this analysis. We have digitized the 50% and 90% contours from Fig. 5 of Ref. [5] and compared them to 50% and 90% upper limit contours for our result computed using a radial binning to enclose 50% and 90% of the posterior probability starting from $\Lambda_1 = \Lambda_2 = 0$. The 90% contours agree well, with a slight difference in the 50% contours. Given the accuracy of measuring the tidal deformability, this difference can

be attributed to small differences in the technical aspects of our analysis compared to that of Ref. [5]. We note that the 90% confidence contour of Fig. 5 in Ref. [5] with $\Lambda_1 = \Lambda_2$, passes through $\tilde{\Lambda} \approx 1100$. If we impose $\Lambda_1 = q^6 \Lambda_2$, then this contour continues to follow $\tilde{\Lambda} \approx 1100$ for $q \leq 1$. We interpret the difference between this result and the result of Table I of Ref. [5] $\tilde{\Lambda} \leq 800$ (90% confidence) as being due to a different choice of prior on $\tilde{\Lambda}$ (one non-uniform and one uniform).

Our common equation of state constraint is implemented in the MCMC by drawing a variable $\Lambda_s \sim U[0, 5000]$, drawing the component masses from their respective priors and computing

$$\Lambda_1 = q^3 \Lambda_s, \quad \Lambda_2 = q^{-3} \Lambda_s, \quad (5.9)$$

with draws that have $\tilde{\Lambda} > 5000$ discarded. This produces a prior that is uniform in $\tilde{\Lambda}$ between 0 and 5000, as shown in Fig. 14 for all of our three mass priors discussed in the main text. For comparison, we also show the prior on $\tilde{\Lambda}$ computed assuming independent $\Lambda_{1,2} \sim U[0, 3000]$ and the component mass prior $m_{1,2} \sim U[1, 2] M_\odot$. It can be seen that this prior vanishes as $\tilde{\Lambda} \rightarrow 0$ and so can bias the posterior at low values of $\tilde{\Lambda}$. In addition to the physical requirement of a common EOS constraint, the prior used in the common EOS analysis is uniform as $\tilde{\Lambda} \rightarrow 0$, allowing us to fully explore likelihoods in this region, and set lower bounds on our credible intervals.

5.5 Results

Fig. 15 shows the posterior probability densities for the parameters of interest in our study: the source frame chirp mass \mathcal{M}^{src} ; the mass ratio $q = m_2/m_1$; the source frame component masses $m_{1,2}^{\text{src}}$ (which are functions of \mathcal{M}^{src} and q); the effective spin $\chi_{\text{eff}} = (m_1 \chi_1 + m_2 \chi_2)/(m_1 + m_2)$; and the binary tidal deformability $\tilde{\Lambda}$. Posterior probability densities are shown for the uniform mass prior, double neutron star mass prior, and the Galactic neutron star mass prior analyses with 20 Hz low-frequency cutoff, and the uniform mass prior analyses with 25 Hz low-frequency cutoff. All the four analyses had the common EOS constraint and the causal $\Lambda(m)$ lower limit imposed. Electronic files containing the thinned posterior probability densities and an IPython notebook [180] for manipulating these data are available at Ref. [181].

Figure 11 shows the posterior probability densities for Λ_1 and Λ_2 with 90% and 50% credible region contours. Overlaid are q contours and $\tilde{\Lambda}$ contours obtained from

Eq. (5.1), $\Lambda \simeq a\beta^{-6}$, and $R_1 \simeq R_2 \simeq \hat{R}$ as

$$\Lambda_1(\tilde{\Lambda}, q) = \frac{13}{16} \tilde{\Lambda} \frac{q^2(1+q)^4}{12q^2 - 11q + 12}, \quad \Lambda_2(\tilde{\Lambda}, q) = q^{-6} \Lambda_1. \quad (5.10)$$

Because of our constraint $\Lambda_2 \geq \Lambda_1$, our credible contours are confined to the region where $q \leq 1$. One can easily demonstrate that $\Lambda_2 \geq \Lambda_1$ is valid unless $(c^2/G)dR/dm > 1$, which is impossible for realistic equations of state. For the entire set of piecewise polytropes satisfying $m_{\max} > 2M_\odot$ we considered, $(c^2/G)dR/dm$ never exceeded 0.26. Even if a first order phase transition appeared in stars with masses between m_2 and m_1 , it would necessarily be true that $dR/dm < 0$ across the transition. Because of the q dependence of Λ_1 , Λ_2 , the credible region enclosed by the contours broadens from the double neutron star (most restricted), to the pulsar, to the uniform mass (least restricted) priors. However, the upper bound of the credible region is robust.

We find $\tilde{\Lambda} = 205_{-167}^{+415}$ for the uniform component mass prior, $\tilde{\Lambda} = 234_{-180}^{+452}$ for the prior informed by double neutron star binaries in the Galaxy, and $\tilde{\Lambda} = 218_{-173}^{+445}$ for the prior informed by all Galactic neutron star masses (errors represent 90% credible intervals). Our measurement of $\tilde{\Lambda}$ appears to be robust to the choice of component mass prior, within the (relatively large) statistical errors on its measurement. The Bayes factors comparing the evidence from the three mass priors are of order unity, so we cannot claim any preference between the mass priors.

The 90% credible intervals on $\tilde{\Lambda}$ obtained from the gravitational-wave observations include regions forbidden by causality. Applying a constraint to our posteriors for the causal lower limit of Λ as a function of m [182], we obtain $\tilde{\Lambda} = 222_{-138}^{+420}$ for the uniform component mass prior, $\tilde{\Lambda} = 245_{-151}^{+453}$ for the prior informed by double neutron star binaries in the Galaxy, and $\tilde{\Lambda} = 233_{-144}^{+448}$ for the prior informed by all Galactic neutron star masses (errors represent 90% credible intervals). Using Eq. (5.6), we map our \mathcal{M} posteriors and $\tilde{\Lambda}$ posteriors (with the causal lower limit applied) to $\hat{R} \simeq R_{1.4}$ posteriors, allowing us to estimate the common radius of the neutron stars for GW170817 for each mass prior. Figure 16 shows the posterior probability distribution for the binary tidal deformation $\tilde{\Lambda}$ and the common radius \hat{R} of the neutron stars in the binary. Our results suggest a radius $\hat{R} = 10.7_{-1.6}^{+2.1} \pm 0.2$ km (90% credible interval, statistical and systematic errors) for the uniform mass prior, $\hat{R} = 10.9_{-1.6}^{+2.1} \pm 0.2$ km for double neutron star mass prior, and $\hat{R} = 10.8_{-1.6}^{+2.1} \pm 0.2$ km for the prior based on all neutron star masses.

Finally, we note the post-Newtonian waveform family used will result in systematic errors in our measurement of the tidal deformability [183, 57]. However, this waveform family allows a direct comparison to the results of Ref. [5]. Accurate modeling of the waveform is challenging, as the errors in numerical simulations are comparable to the size of the matter effects that we are trying to measure [184]. Waveform systematics and comparison of other waveform models (e.g., [51]) will be investigated in a future work.

5.6 Discussion

Using Bayesian parameter estimation, we have measured the tidal deformability and common radius of the neutron stars in GW170817. Table 1 summarizes our findings. To compare to Ref. [5], which reports a 90% upper limit on $\tilde{\Lambda} \leq 800$ under the assumption of a uniform prior on $\tilde{\Lambda}$, we integrate the posterior for $\tilde{\Lambda}$ to obtain 90% upper limits on $\tilde{\Lambda}$. For the common EOS analyses, these are 485, 521, and 516 for the uniform, double neutron star, and Galactic neutron star component mass priors, respectively. We find that, in comparison to the unconstrained analysis, the common EOS assumption significantly reduces the median value and 90% confidence upper bound of $\tilde{\Lambda}$ by about 28% and 19%, respectively, for all three mass priors. The difference between our common EOS results for the three mass priors is consistent with the physics of the gravitational waveform. At constant \mathcal{M} , decreasing q causes the binary to inspiral more quickly [185]. At constant \mathcal{M} and constant q , increasing $\tilde{\Lambda}$ also causes the binary to inspiral more quickly, so there is a mild degeneracy between q and $\tilde{\Lambda}$. The uniform mass prior allows the largest range of mass ratios, so we can fit the data with a larger q and smaller $\tilde{\Lambda}$. The double neutron star mass prior allows the smallest range of mass ratios, and so, a larger $\tilde{\Lambda}$ is required to fit the data, with the Galactic neutron star mass prior lying between these two cases.

Nevertheless, considering all analyses we performed with different mass prior choices, we find a relatively robust measurement of the common neutron star radius with a mean value $\langle \hat{R} \rangle = 10.8$ km bounded above by $\hat{R} < 13.2$ km and below by $\hat{R} > 8.9$ km. Nuclear theory and experiment currently predict a somewhat smaller range by 2 km but with approximately the same centroid as our results [172, 186]. A minimum radius 10.5–11 km is strongly supported by neutron matter theory [187, 188, 189],

Mass prior	$\tilde{\Lambda}$	\hat{R} (km)	$\tilde{\Lambda}_{90\%}$
Uniform	222^{+420}_{-138}	$10.7^{+2.1}_{-1.6} \pm 0.2$	< 485
Double neutron star	245^{+453}_{-151}	$10.9^{+2.1}_{-1.6} \pm 0.2$	< 521
Galactic neutron star	233^{+448}_{-144}	$10.8^{+2.1}_{-1.6} \pm 0.2$	< 516

Table 1: Results from parameter estimation analyses using three different mass prior choices with the common EOS constraint, and applying the causal minimum constraint to $\Lambda(m)$. We show 90% credible intervals for $\tilde{\Lambda}$, 90% credible intervals and systematic errors for \hat{R} , and the 90% upper limits on $\tilde{\Lambda}$.

the unitary gas [190], and most nuclear experiments [172, 186, 191]. The only major nuclear experiment that could indicate radii much larger than 13 km is the PREX neutron skin measurement, but this has published error bars much larger than previous analyses based on antiproton data, charge radii of mirror nuclei, and dipole resonances. Our results are consistent with photospheric radius expansion measurements of x-ray binaries which obtain $R \approx 10\text{--}12$ km [6, 192, 193]. Reference [194] found from an analysis of five neutron stars in quiescent low-mass x-ray binaries a common neutron star radius 9.4 ± 1.2 km, but systematic effects including uncertainties in interstellar absorption and the neutron stars’ atmospheric compositions are large. Other analyses have inferred 12 ± 0.7 [195] and 12.3 ± 1.8 km [196] for the radii of $1.4M_{\odot}$ quiescent sources.

We have found that the relation $q^{7.48} < \Lambda_1/\Lambda_2 < q^{5.76}$, in fact, completely bounds the uncertainty for the range of \mathcal{M} relevant to GW170817, assuming $m_2 > 1M_{\odot}$ [182] and that no strong first-order phase transitions occur near the nuclear saturation density (i.e., the case in which m_1 is a hybrid star and m_2 is not). Analyses using this prescription instead of the q^6 correlation produce insignificant differences in our results. Since models with the common EOS assumption are highly favored over those without this assumption, our results support the absence of a strong first-order phase transition in this mass range.

We have shown that, for binary neutron star mergers consistent with observed double neutron star systems [197], assuming a common EOS implies that $\Lambda_1/\Lambda_2 \simeq q^6$. We find evidence from GW170817 that favors the common EOS interpretation compared to uncorrelated deformabilities. Although previous studies have suggested that measurement of the tidal deformability is sensitive to the choice of mass prior [58],

we find that varying the mass priors does not significantly influence our conclusions suggesting that our results are robust to the choice of mass prior. Our results support the conclusion that we find the first evidence for finite size effects using gravitational-wave observations.

Recently, the LIGO/Virgo collaborations have placed new constraints on the radii of the neutron stars using GW170817 [198]. The most direct comparison is between our uniform mass prior result ($\hat{R} = 10.7_{-1.6}^{+2.1} \pm 0.2$) and the LIGO/Virgo method that uses equation-of-state-insensitive relations [199, 200] ($R_1 = 10.8_{-1.7}^{+2.0}$ and $R_2 = 10.7_{-1.5}^{+2.1}$ km). This result validates our approximation $R_1 = R_2$ used to motivate the prescription $\Lambda_1 = q^6 \Lambda_2$, and Eqs. (5.3, 5.5). Our statistical errors are comparable to the error reported by LIGO/Virgo. Systematic errors from EOS physics of ± 0.2 km are added as conservative bounds to our statistical errors, broadening our measurement error, whereas Ref. [198] marginalized over these errors in the analysis. Reference [198] also investigates a method of directly measuring the parameters of the EOS which results in smaller measurement errors. Investigation of these differences between our analysis and the latter approach will be pursued in a future paper.

Observations of future binary neutron star mergers will allow further constraints to be placed on the deformability and radius, especially if these binaries have chirp masses similar to GW170817 as radio observations suggest. As more observations improve our knowledge of the neutron star mass distribution, more precise mass-deformability correlations can be used to further constrain the star's radius.

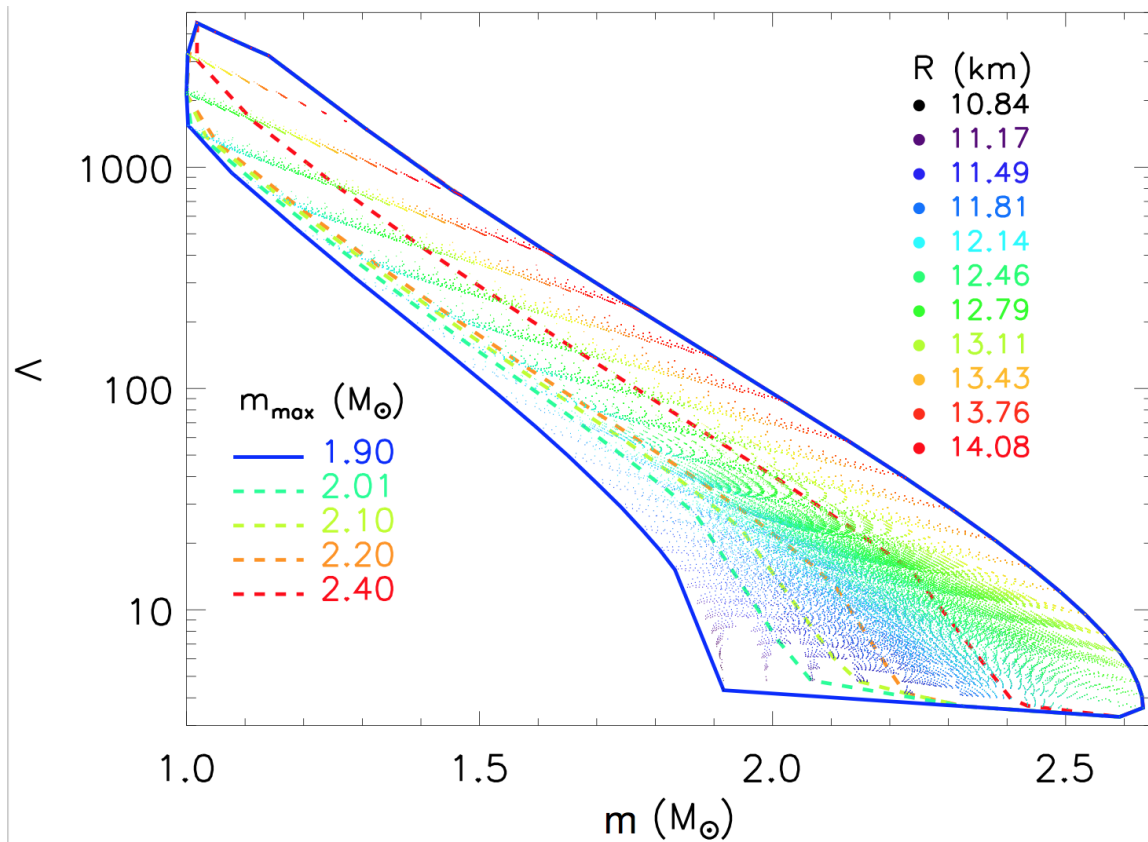


Figure 10: The tidal deformability Λ as a function of mass for physically realistic polytropes. A TOV integration with each EOS parameter set results in a series of values of $\Lambda(m)$ that are shown as points colored by their radii R . Dashed curves are lower bounds to Λ for a given mass m which vary depending on the assumed lower limit to the neutron star maximum mass, m_{\max} . All values of m_{\max} produce the same upper bound.

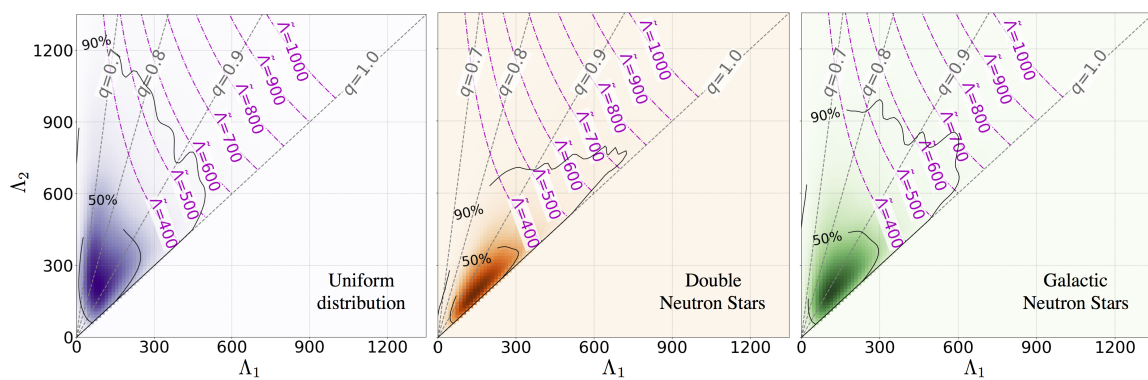


Figure 11: Posterior probability densities for $\Lambda_{1,2}$ with the common EOS constraint using uniform (left), double neutron stars (middle), and Galactic neutron stars (right) component mass priors. The 50% and 90% credible region contours are shown as solid curves. Overlaid are contours of $\tilde{\Lambda}$ (in magenta) and q (in gray). The values of Λ_1 and Λ_2 forbidden by causality have been excluded from the posteriors.

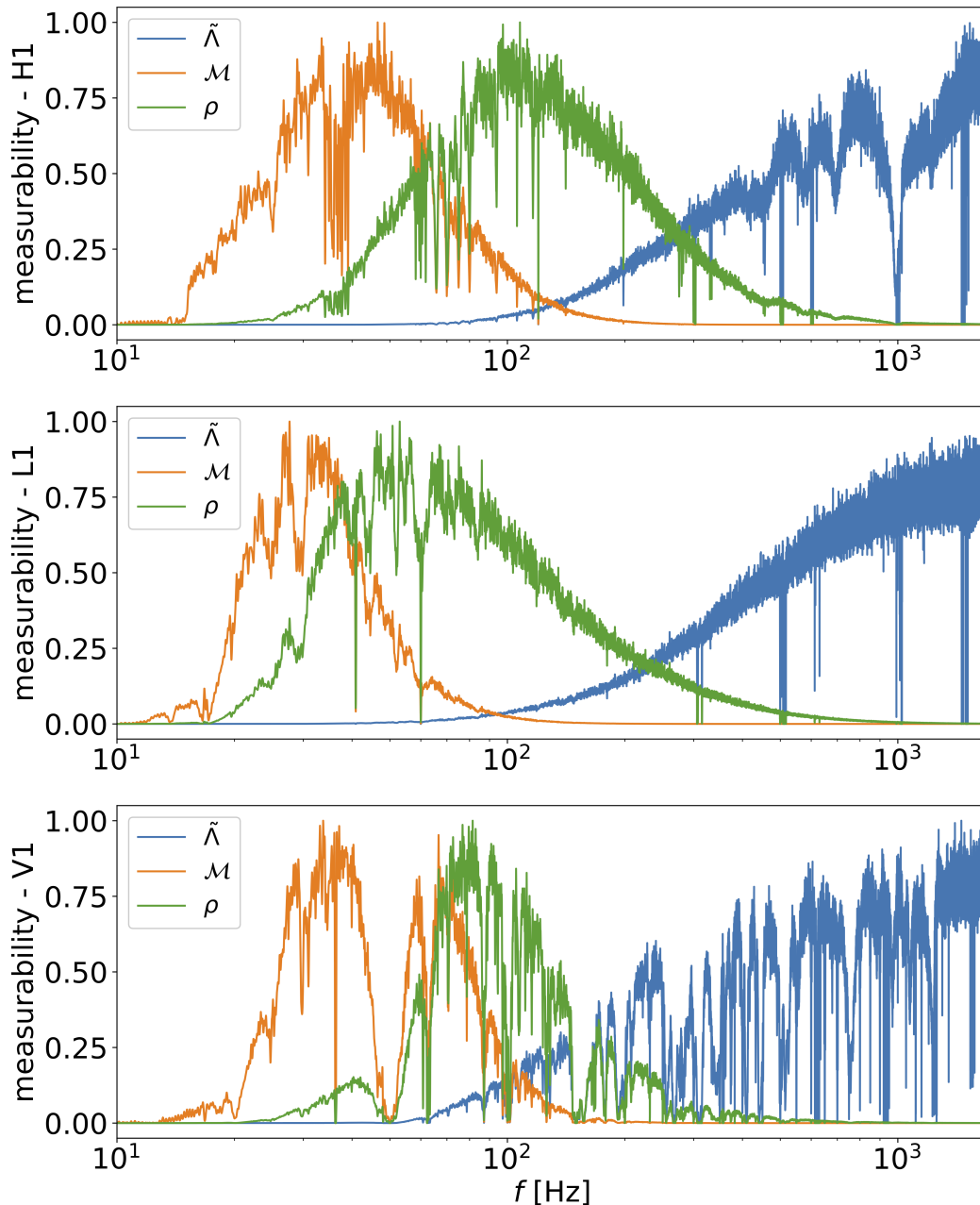


Figure 12: Measurability [4] of the chirp mass \mathcal{M} , SNR ρ and binary deformability $\tilde{\Lambda}$ in the frequency range 10 Hz - 2000 Hz. Each detector's parameter measurability is scaled to the maximum frequency to show the relative accumulation of measurement over the detector's frequency band. Note that between detectors, L1 is more sensitive than H1, which is more sensitive than V1. Measurability of chirp mass is accumulated primarily at low frequencies, whereas measurability of tidal deformability is accumulated at higher frequencies. We extend computation of the likelihood down to 20 Hz where the measured signal-to-noise ratio (the logarithm of the likelihood) drops to zero in all three detectors.

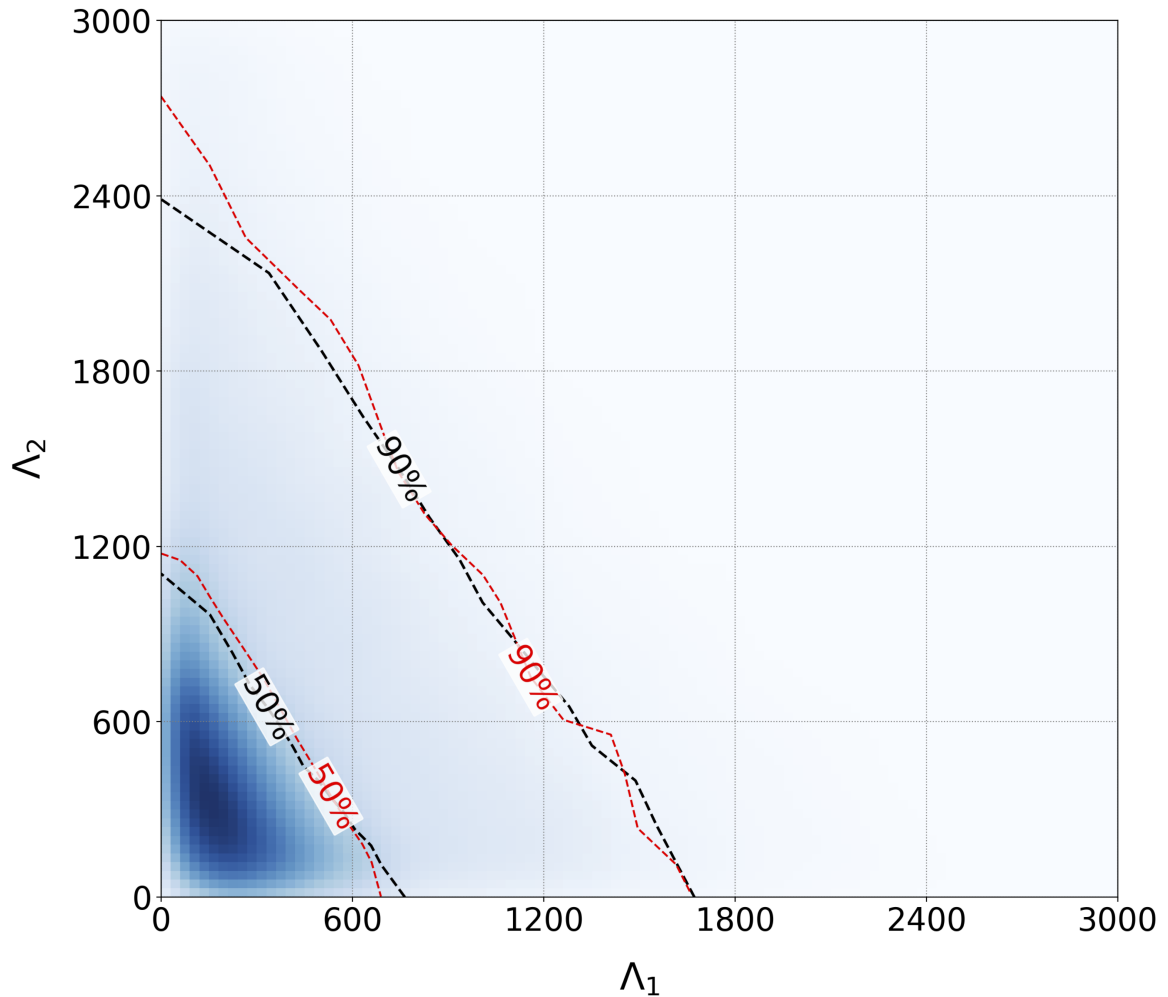


Figure 13: Posterior probability density function for Λ_1 , Λ_2 from unconstrained $\Lambda_{1,2} \sim U[0, 3000]$, $m_{1,2} \sim U[1, 2] M_\odot$, $1.1876 \leq \mathcal{M} \leq 1.2076$, $m_1 \geq m_2$, 30 Hz low-frequency cutoff analysis. The black dotted lines show 50% and 90% upper limits from our analysis. The red dotted lines show 50% and 90% upper limits from the LIGO-Virgo analysis [5].

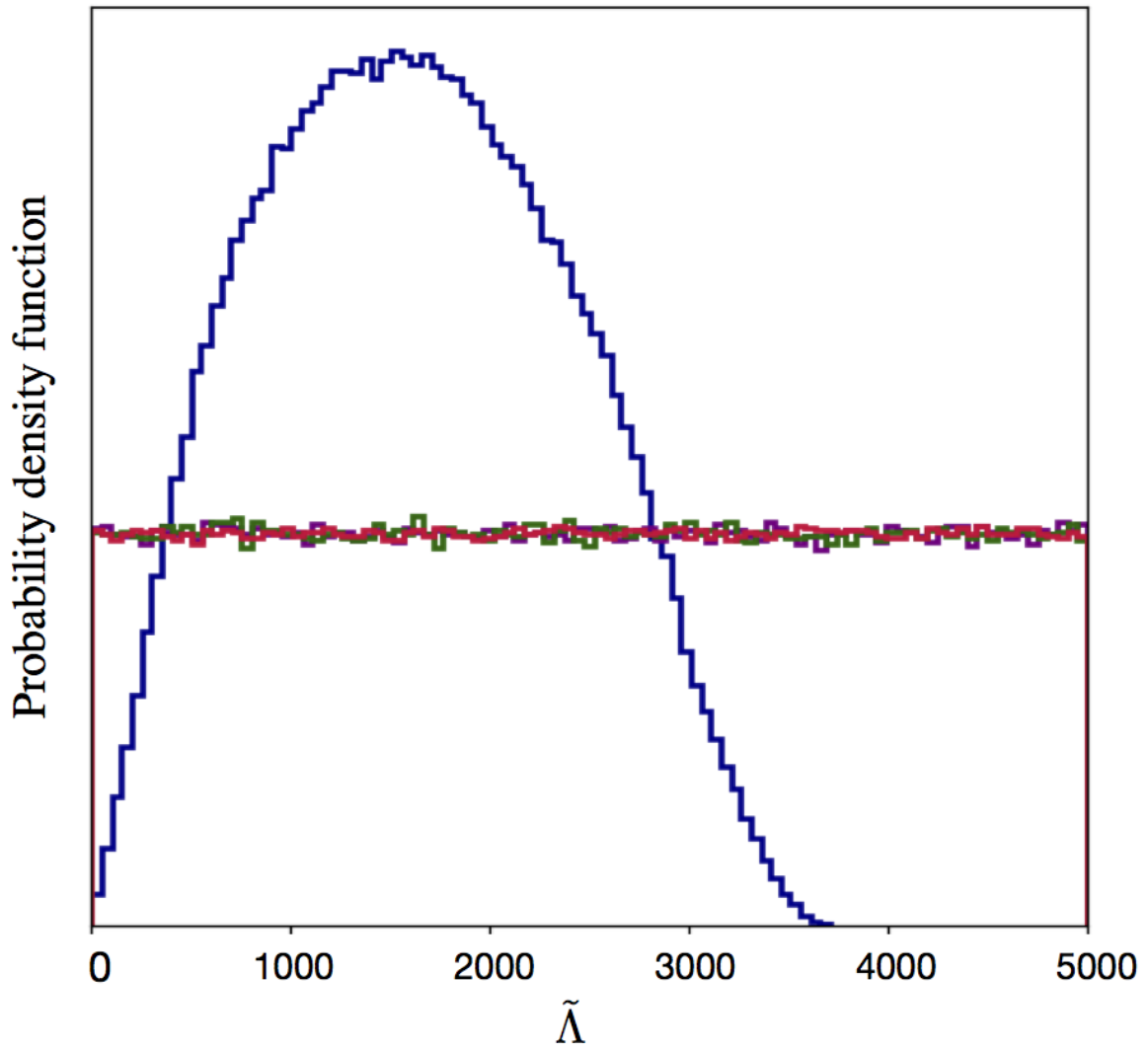


Figure 14: Comparison of the prior probability distributions on $\tilde{\Lambda}$ for the three mass priors imposing the common EOS constraint: uniform (purple), double neutron stars (red), galactic neutron stars (green) with a prior in $\Lambda_{1,2} \sim U[0, 3000]$ and $m_{1,2} \sim U[1, 2]M_{\odot}$, $m_1 \geq m_2$ without the common EOS constraint (blue). The priors in the common EOS analysis are uniform across the region of interest.

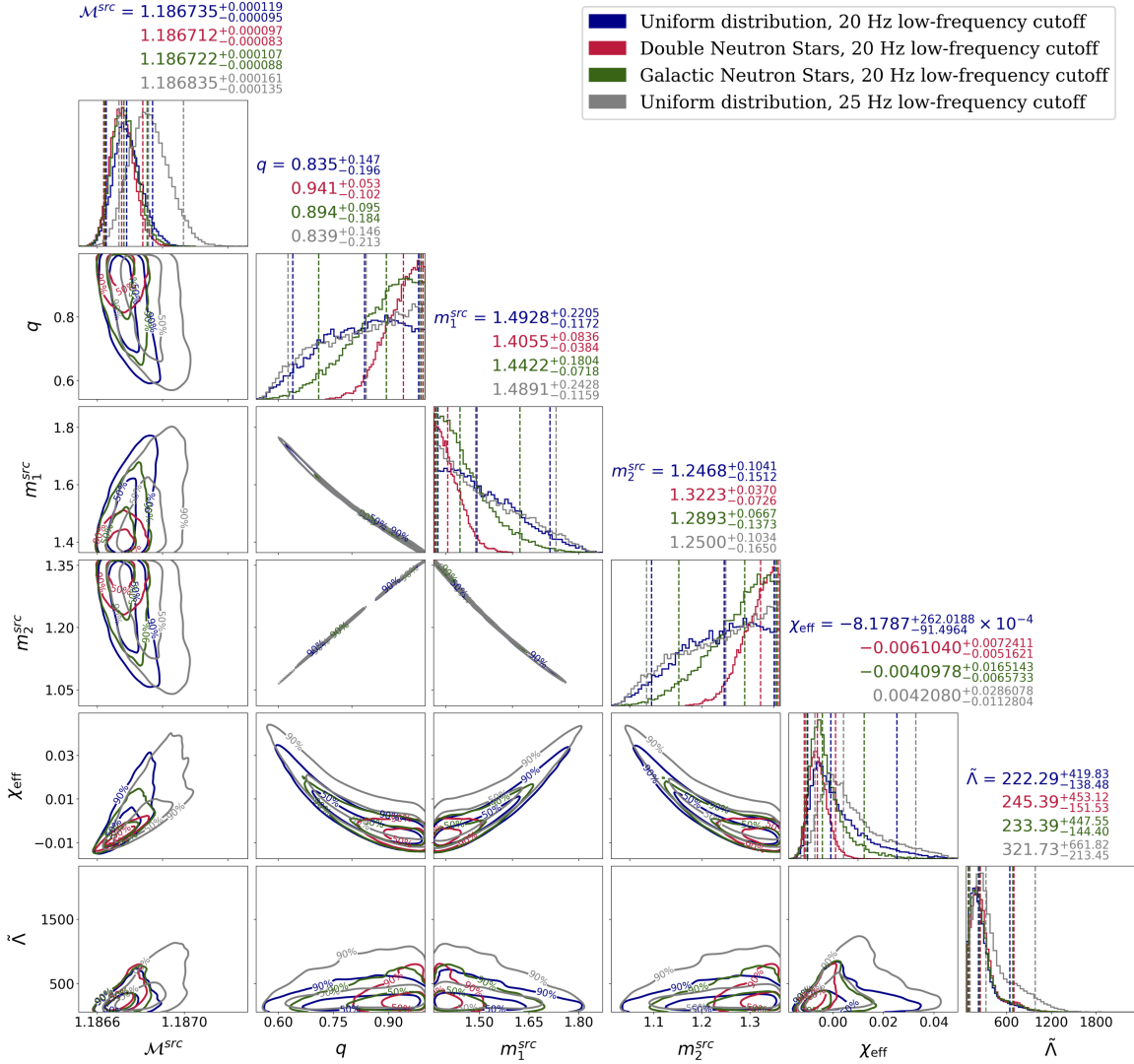


Figure 15: Posterior distributions for the source frame chirp mass \mathcal{M}^{src} , mass ratio q , source frame primary mass m_1^{src} and secondary mass m_2^{src} , effective spin χ_{eff} , and binary deformability parameter $\tilde{\Lambda}$ from parameter estimation analyses with three different choices of mass priors. The posteriors represented in blue are from the analysis using a uniform prior on component masses, $m_{1,2} \sim U[1, 2] M_{\odot}$, and 20 Hz low-frequency cutoff. The posteriors represented in red are from the analysis using a Gaussian mass prior for component masses $m_{1,2} \sim N(\mu = 1.33, \sigma = 0.09) M_{\odot}$ known from radio observations of neutron stars in double neutron star (DNS) systems, and 20 Hz low-frequency cutoff. The posteriors represented in green are from the analysis using the observed mass distributions of recycled and slow pulsars in the Galaxy with $m_1 \sim N(\mu = 1.54, \sigma = 0.23) M_{\odot}$ and $m_2 \sim N(\mu = 1.49, \sigma = 0.19) M_{\odot}$ [6], and 20 Hz low-frequency cutoff. The posteriors represented in gray are from the analysis using a uniform prior on component masses, $m_{1,2} \sim U[1, 2] M_{\odot}$, and 25 Hz low-frequency cutoff. All four analyses had the common EOS constraint and the causal $\Lambda(m)$ lower limit imposed. The one-dimensional plots show marginalized probability density functions for the parameters. The dashed lines on the one-dimensional histograms represent the 5%, 50% and 95% percentiles for each analysis, the values of which are quoted in the titles of the histograms. The 2D plots show 50% and 90% credible regions for the different pairs of parameters. Comparison between the analyses with low-frequency cutoff 20 Hz (blue) and 25 Hz (gray) for the uniform mass prior case shows that extending from 25 Hz to 20 Hz better constrains \mathcal{M} , which improves the measurement of $\tilde{\Lambda}$ by eliminating a region of the posterior with higher values \mathcal{M} and high $\tilde{\Lambda}$.

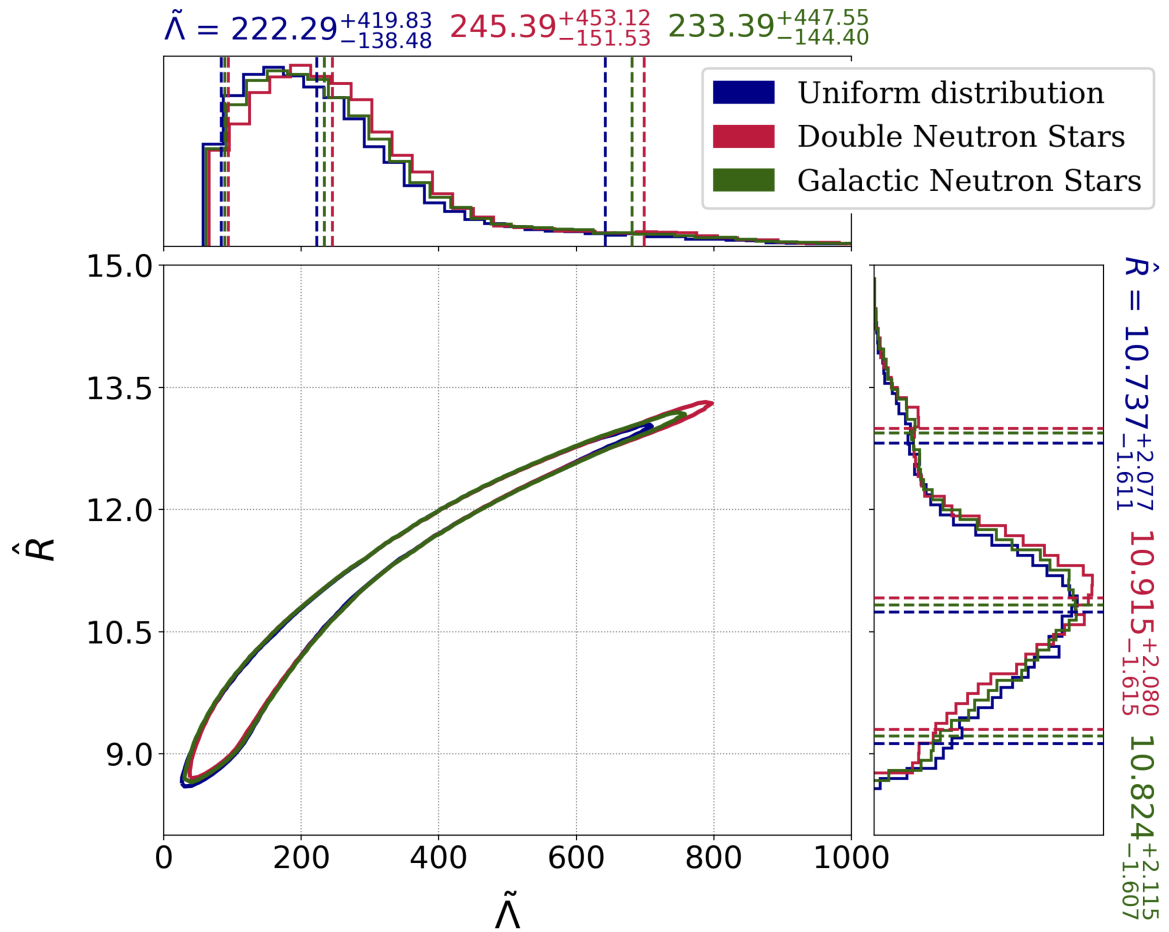


Figure 16: The 90% credible region of the posterior probability for the common radius \hat{R} and binary tidal deformability $\tilde{\Lambda}$ with the common EOS constraint for the three mass priors. The posteriors for the individual parameters are shown with dotted lines at the 5%, 50% and 95% percentiles. The values of $\tilde{\Lambda}$, and hence \hat{R} forbidden by causality have been excluded from the posteriors.

Chapter 6

Prospects for Precise Equation of State Measurements from Advanced LIGO and Cosmic Explorer

Neutron star mergers probe the nature of matter at densities and temperatures far beyond those available in the laboratory. The observation of GW170817 confirmed that gravitational waves can yield meaningful insights into the structure of neutron stars, and hence on the equation of state of matter above nuclear density [5, 201, 202, 203, 204, 205, 206]. Combining gravitational-wave and electromagnetic observations of the first neutron star merger with nuclear theory and numerical simulations has already shed new light on the equation of state of dense matter [142, 207, 208]. The ability of multi-messenger observations of merging neutron stars to explore nuclear physics is determined by: the signal-to-noise ratio of the observed gravitational-wave signals; the fidelity of the waveforms used to model gravitational-wave signals; the ability to model and extract information from electromagnetic counterparts; and theoretical modeling of hot and cold dense nuclear matter and its connection to the observed quantities. In this chapter, we focus on the impact that the signal-to-noise ratio of the signal has on the ability to measure the neutron star equation of state with current and future gravitational-wave detectors.

Gravitational-wave observations of binary neutron star mergers measure the nuclear equation of state through the star’s tidal deformability Λ which is imprinted on the phasing of the inspiral waveform. This measurement of Λ is equivalent to a measurement of the neutron star radius, and hence the nuclear equation of state which connects these two quantities for a given mass. Previous studies have shown that Advanced LIGO will be able to measure the radius of a $1.4M_{\odot}$ neutron star $R_{1.4}$ to better than 10% precision with the first few tens of binary neutron star signals. However many plausible equations of state produce similar radii for a range of masses, so that distinguishing between them would require measurement precision better than 2%. In this work we assess the ability of both Advanced LIGO and the proposed third-generation detector Cosmic Explorer, to make a precise measurement of the equation of state from a large population of simulated binary neutron star signals, for several equations of state that span the plausible range. We perform full Bayesian parameter estimation on all simulated signals and produce a combined measurement of $R_{1.4}$. We find that with 321 signals Advanced LIGO is able to measure $R_{1.4}$ to better than 2% across the entire range of plausible equations of state, although the probability of seeing so many signals in the next decade is low. On the other hand we find that with one year of observation, Cosmic Explorer will be able to measure $R_{1.4}$ to within 0.6% for a soft equation of state, and to within 0.15% for a moderately stiff equation of state.

6.1 Introduction

The observation of the binary neutron star merger GW170817 during the second observing run of the LIGO-Virgo network provided the first constraints on the cold dense matter equation of state through gravitational waves [209]. The observations of AT2017gfo, the electromagnetic counterpart to GW170817, were also able to constrain the equation of state through estimates of the ejecta mass and velocity [210], and by probing the fate of the merger remnant [34]. Additional constraints have also recently come from pulsar observations and nuclear experiment: X-ray observations by the *NICER* instrument of the pulsars J0740+6620 and J0030+0451 have mapped out some of the neutron star mass-radius relationship through direct radius measurements [211, 212, 213], and in the low pressure regime the *PREX-II*

experiment has made precise measurements of the density dependence of the nuclear symmetry energy for lead atoms [214], which can be mapped to the higher pressures in neutron stars in order to also provide an estimate of the expected neutron star radius [215]. Recent efforts have been made to combine some of these and other disparate measurements into a generalized constraint on the equation of state, often given in terms of the radius of a $1.4M_{\odot}$ neutron star $R_{1.4}$: [215] combined the *PREX-II* measurement and the *NICER* constraints on the radius of the pulsar J0030+0451 to give $13.25 \text{ km} < R_{1.4} < 14.26 \text{ km}$ (1σ limits), and [216] combined GW170817, quiescent low-mass X-ray binaries, photospheric radius expansion X-ray bursts, and J0030+0451 to find $R_{1.4} = 11.83^{+0.62}_{-0.71} \text{ km}$ (2σ limits).

While great strides have been made in producing constraints on the equation of state, the prospects for improving these constraints using binary merger events still face significant challenges. GW170817 was a remarkably loud signal, with a signal-to-noise ratio of over 33, and yet the gravitational-wave observation alone was insufficient to conclusively distinguish the signal from a pair of merging black holes [209]. A second binary neutron star signal, GW190425, was observed by the LIGO-Virgo network but at a much lower signal-to-noise ratio of 13, which provided negligible information about the equation of state and also meant that no electromagnetic counterpart was identified [217]. Similarly, there have been three gravitational-wave observations of probable neutron star–black hole mergers to date containing no measurable information on the equation of state, or any identifiable electromagnetic counterpart from the possible disruption of the neutron star [18, 17]. Further complicating matters, the estimated merger rate of binary neutron stars in the local universe has been revised significantly lower after the completion of LIGO’s third observing run [8], which means a correspondingly lower probability that future observing runs will produce a large set of observed signals that can be combined into a precise constraint on the equation of state.

Where previous works have investigated distinguishability between equation of state models, most have primarily focused on distinguishing models that differ substantially from one another. However many models exist that are consistent with current constraints but make similar predictions. As an example, the commonly used models WFF2, APR4, and SQM3, predict values for $R_{1.4}$ of 11.16, 11.32, and 11.37 kilometers, respectively. Naturally the prospect of distinguishing between these or

other similar models is a much greater challenge, but this is very likely what will be required of future equation of state constraints. For the example models given, this will require measurements of $R_{1.4}$ with a precision better than 2%.

The ability to measure the equation of state in gravitational-wave signals depends very sensitively on the equation of state itself, because the range of plausible models predict varying amounts of information in an inspiral waveform. Gravitational-wave signals from coalescing neutron stars carry information about the equation of state as a result of the tidal deformation that the stars' gravitational fields produce in one another. Specifically, the quadrupole moment Q_{ij} of one neutron star is related to the tidal field \mathcal{E}_{ij} of the other neutron star according to $Q_{ij} = -\lambda\mathcal{E}_{ij}$, where λ is the tidal deformability of the neutron star [48]. The tidal deformability is dependent on the equation of state and is commonly expressed in dimensionless form as

$$\Lambda = \frac{2}{3}k_2 \left(\frac{Rc^2}{Gm} \right)^5 \quad (6.1)$$

where k_2 is the tidal Love number. R and m are the radius and mass of the neutron star, respectively. The energy expended in deforming the stars results in a phase difference in the gravitational waveform as compared to a signal with non-deforming bodies. An equation of state that has a large Λ for a given mass is said to be “stiff”, and will generally correspond to a larger radius as the neutron star is more able to hold itself up against gravity. A stiff equation of state produces a larger effect on the gravitational-wave phasing and is therefore more measurable. Conversely, a “soft” equation of state will have a smaller Λ and radius for a given mass, and produces a less measurable effect in a gravitational-wave signal.

Given the difficulty of measuring the equation of state, an established method of improving constraints is to combine multiple observations in order to reduce statistical uncertainty [218]. Previous works have used various implementations of this method to estimate the measurability of the equation of state for a given signal population or detector network [218, 57, 58, 219, 10]. Lackey and Wade [57] combined signals in a simulated LIGO-Virgo network at design sensitivity, for several choices of equation of state. They constrain the neutron star radius across a range of masses and find that the radius can be measured to within ± 1 kilometer with 20 signals. Agathos *et al.* [58] combined 200 signals in a LIGO-Virgo network and found that a catalog of at least 100 signals is sufficient to distinguish between soft, moderate, and stiff equations

of state if one assumes perfect knowledge of the mass distribution, while 150 or more signals would be needed if the mass distribution was unknown. [219] project that the 8 loudest signals from a population of 20 in a LIGO-Virgo network will constrain the radius of a canonical $1.4M_{\odot}$ neutron star to within 10%. Pacilio *et al.* [10] combine 20 signals in both a LIGO-Virgo network and Einstein Telescope, a proposed third-generation detector. They find that LIGO-Virgo is unable to distinguish between similarly soft equations of state from a catalog of 12 used in the analysis, although Einstein Telescope can potentially make this distinction.

In this chapter we build upon these previous works to produce an accurate forecast for a high precision measurement of the equation of state, using both a LIGO-Virgo network operating at design sensitivity as well as a planned third-generation detector Cosmic Explorer. We make our forecast using a population of simulated binary neutron star signals generated from astrophysically realistic parameter distributions. We produce parallel populations of these signals for three choices of equation of state that span the range of the most up-to-date constraints from gravitational-wave events, electromagnetic observations of pulsars and the kilonova AT2017gfo, and nuclear experiments. We perform full Bayesian parameter estimation for each signal in our populations to recover the intrinsic and extrinsic source parameters, and we use a collection of 2000 realistic equations of state built from nuclear theory as a prior distribution in our analysis. We produce a combined equation of state measurement across our populations by transforming each measurement to a constraint on $R_{1.4}$, the radius of a $1.4M_{\odot}$ neutron star. We find that a LIGO-Virgo network is able to measure $R_{1.4}$ to within 2% across the entire range of plausible equations of state, though a soft equation of state will require significantly more signals that are unlikely to occur within the next planned observing runs. We find also that an incorrect mass prior used by our LIGO-Virgo analysis introduces a bias in the equation of state measurement such that a combined measurement with better than 2% precision will exclude the true equation of state at high confidence. We find that Cosmic Explorer is able to achieve better than 0.6% precision on $R_{1.4}$ with signals representing one year of observations for even the softest equation of state in our analysis. We find that in our Cosmic Explorer analysis an incorrect mass prior did introduce a bias, although it was not large enough to strongly exclude the true equation of state even with the much smaller statistical uncertainty on the measurement.

The rest of this chapter is organized as follows: Section 6.2 describes the simulated binary neutron star signals included in our analysis. In Section 6.3 we give background information on equation of state information in gravitational-wave inspiral signals and describe the equations of state used in this analysis. Section 6.4 gives details about our parameter estimation analysis including the method of combining measurements. Section 6.5 presents the results of our analysis including constraints for each of our chosen equations of state. Finally, we conclude in Section 6.6.

6.2 Simulated signals

To simulate measurement scenarios for a LIGO-Virgo network and Cosmic Explorer, we generate a population of simulated binary neutron star merger signals and project them onto the corresponding detectors. For LIGO-Virgo we simulate a three-detector network representing the LIGO Hanford, LIGO Livingston [145, 146], and Virgo [13] detectors. Each LIGO-Virgo detector is simulated at its design sensitivity by injecting simulated signals into Gaussian noise colored by the design power spectral density for each detector [9]. Cosmic Explorer is still in its design phase and does not have a final configuration or site location determined yet, although potential sites in the United States include locations in Utah or Idaho. For simplicity we use a hypothetical Cosmic Explorer detector at the same location and orientation as the LIGO Hanford detector. We choose the 40 kilometer arm length configuration optimized for detection of coalescing binaries for our analysis, and signals are injected into Gaussian noise colored by the corresponding design power spectral density [220].

Following the prescription of [58] we generate our simulated binary neutron star mergers using astrophysically motivated distributions for the source parameters. The collection of electromagnetic observations of known galactic pulsars has found their mass distribution to be well described by a Gaussian centered near $1.4M_{\odot}$. However the gravitational wave observations of GW190425 and two of the neutron star–black hole signals show evidence for a greater number of high-mass neutron stars in the range $1.7 - 1.9M_{\odot}$. To account for both possibilities and to investigate the effect of a different mass distribution on the ability to measure the equation of state, we generate our population for two choices of mass distribution. For our primary population, source-frame component masses are drawn from a Gaussian distribution with mean

$\mu_m = 1.4M_\odot$ and standard deviation $\sigma_m = 0.05M_\odot$. A secondary population has source-frame component masses drawn uniformly in the range $1 - 2M_\odot$. In all cases, component spins along the axis of orbital angular momentum are drawn from a Gaussian distribution with zero-mean and standard deviation $\sigma_\chi = 0.02$. Sky locations are distributed uniformly across the sky, and the inclination and orientation of the binary systems is distributed uniformly on the sphere. For signals analyzed with the LIGO-Virgo network, distances are drawn uniformly in volume in the range $[20, 585]$ Mpc, where the upper bound is the largest distance at which an optimally oriented binary merger with equal masses of $2M_\odot$ would produce a single detector signal-to-noise ratio of 8. Simulated signals are then pre-filtered via a network matched-filter signal-to-noise calculation to select the subset with signal-to-noise $\rho_{\text{mf}} > 13.85$, which is equivalent to a signal-to-noise of 8 in each detector. The resulting LIGO-Virgo population contains 321 signals with signal-to-noise ratios that range from about 10 to 73 for the Gaussian-mass case, and 312 signals with signal-to-noise 10 to 65 for the uniform-mass case. For signals analyzed with Cosmic Explorer, distances are drawn uniformly in volume in the interval $[20, 1100]$ Mpc, with the upper bound determined similarly to the LIGO-Virgo case except requiring $\rho_{\text{mf}} > 100$. The Cosmic Explorer population contains 335 signals with signal-to-noise ranging from about 97 to 790. Except where otherwise noted, stated results will be for the primary population.

We replicate our populations for three different equations of state, which are chosen to span the range allowed by the most comprehensive set of observations and constraints currently available. Each sub-population is generated using a single equation of state, and every neutron star within a sub-population has its tidal deformability determined by the equation of state and its mass. Our choices of equation of state are discussed in greater detail in Section 6.3. All simulated signals are generated using the `IMRPhenomD_NRTidal` waveform approximant [98, 99, 100], which is a frequency domain waveform available in LALSuite [47]. The waveform uses a phenomenological model tuned to numerical relativity data, and it includes contributions to the gravitational-wave phase due to the tidal deformation of the neutron stars.

6.3 Equation of state in gravitational waves

A general frequency-domain gravitational waveform can be expressed

$$h(f) = \mathcal{A} f^{-7/6} \exp[i(\psi_{pp} + \psi_{tidal})] \quad (6.2)$$

where \mathcal{A} is the waveform amplitude, ψ_{pp} is the point-particle contribution to the phasing, and ψ_{tidal} is the contribution to the phasing from tidal effects. At leading order, the tidal phasing is determined by the *effective* tidal deformability $\tilde{\Lambda}$, defined as

$$\tilde{\Lambda} = \frac{16(12q+1)\Lambda_1 + (12+q)q^4\Lambda_2}{13(1+q)^5} \quad (6.3)$$

where $q = m_2/m_1 \leq 1$ is the mass ratio. Thus the leading order tidal phasing in a gravitational waveform is

$$\psi_{tidal} \propto \tilde{\Lambda} f^{5/3}. \quad (6.4)$$

This means a gravitational-wave signal allows a measurement of the amount of deformation occurring during an inspiral, and thus of the equation of state of the dense matter comprising the interior of the neutron star. As is clear from Equation 6.4 the tidal effect in a gravitational waveform is larger for higher frequencies, and it has previously been found that it only becomes measurable for $f \gtrsim 400$ Hz [55]. Both the LIGO-Virgo and proposed Cosmic Explorer detectors have decreased sensitivity at these higher frequencies where the tidal information exists, due to fundamental limitations of the laser interferometer design [56]. This makes the measurement of tidal information in gravitational-wave signals inherently challenging, and therefore differences in measurability between soft and stiff equations of state can be significant.

To illustrate the issue, in Figure 17 we show the match between gravitational waveforms with tidal information included versus corresponding waveforms with no tides, where the match is measured as the noise-weighted overlap between the two waveforms. We calculate the match for different combinations of $\tilde{\Lambda}$ and neutron star mass m for the case of an equal-mass binary. We plot also the functional $m - \tilde{\Lambda}$ relationship for two equations of state representing the soft and stiff ends of the plausible range. The measurability of the tidal information is equivalent to the degree of mismatch as compared to a non-tidal waveform. Both equations of state pass through regions of differing match owing to the mass dependence of the tidal deformability, but the stiff equation of state consistently lies in regions with substantially lower match implying

a greater measurability. This is especially true for neutron star masses below about $1.6M_{\odot}$.

To explore the effect of a stiff or soft equation of state on our ability to place precise constraints, we select for our analysis three equations of state that span the full plausible range. We require that each equation of state support a maximum neutron star mass of $2M_{\odot}$. For simplicity, we do not include any equations of state that contain a phase transition of the dense matter. The equations of state are selected from a set of 2000 that are constructed from nuclear chiral effective field theory, which is calibrated to nuclear experiments up to the nuclear saturation density. From soft to stiff, our chosen equations of state are labeled EOS 487, EOS 895, and EOS 1250, and in Figure 18 we show their location in the $R_{1.4} - \Lambda_{1.4}$ plane along with a selection of recent equation of state constraints from electromagnetic and gravitational-wave observations to date. Also plotted are the pairs of $(R_{1.4}, \Lambda_{1.4})$ values from the entire set of 2000 equations of state used in our analysis as a prior distribution for the parameter estimation, which we discuss in greater detail in Section 6.4.

6.4 Parameter estimation

In general, under the assumption of Gaussian noise characterized by a power spectral density $S(f)$, the likelihood of obtaining detector data d given the presence of a gravitational waveform $h(\theta)$ is

$$\mathcal{L}(d|\theta) \propto \exp \left[-\frac{1}{2} \langle d - h(\theta) | d - h(\theta) \rangle \right], \quad (6.5)$$

where

$$\langle a | b \rangle = 4\Re \int_{f_{\min}}^{f_{\max}} \frac{\tilde{a}^*(f)\tilde{b}(f)}{S(f)} df \quad (6.6)$$

is the noise-weighted inner product [133, 158] and $\theta = \{\theta_1, \theta_2, \dots, \theta_n\}$ is the set of intrinsic and extrinsic parameters defining the waveform. In evaluating this likelihood, we can obtain estimates of the gravitational-wave parameters θ through the joint posterior probability distribution

$$p(\theta|d) \propto \mathcal{L}(d|\theta)p(\theta), \quad (6.7)$$

where $p(\theta)$ is the assumed prior probability distribution of the parameters. Then the marginal posterior probability distribution for an individual parameter is obtained

by integrating $p(\theta|d)$ over all nuisance parameters. For instance, the marginalized posterior distribution for θ_1 is

$$p(\theta_1|d) = \int p(\theta|d) d\theta_2 d\theta_3 \dots d\theta_n. \quad (6.8)$$

We use *PyCBC Inference* [221] with the parallel-tempered version of the `emcee` sampler [102, 103, 222] to sample the parameter space and produce marginalized posterior distributions for the source parameters. To help speed convergence we employ the relative likelihood model available in *PyCBC Inference* which uses an approximation to the full resolution likelihood near its peak in order to reduce runtime, and has been shown to produce comparable parameter estimates to non-relative models [104, 46, 105]. For signals analyzed in the LIGO-Virgo network we include frequencies above a low-frequency cutoff of 20 Hz, and for Cosmic Explorer signals we use frequencies above 7 Hz. All signals are analyzed up to a high frequency cutoff of 2048 Hz. We sample in source-frame component masses, component spins along the direction of the orbital angular momentum, sky location, distance, geocentric time of coalescence, inclination, polarization angle, and equation of state. For each parameter we use a prior distribution that matches the corresponding population distribution with the exception of the equation of state, where our prior distribution is made of a collection of 2000 equations of state built from nuclear theory and designed to be roughly uniform in $R_{1.4}$ over the interval 9 – 15 kilometers. Each equation of state provides a mapping between mass, radius, and tidal deformability for a neutron star. At each iteration, a single equation of state is drawn and used to determine the tidal deformabilities of both neutron stars based on their source-frame masses. In generating a template waveform for the likelihood, source-frame masses are first converted to the detector frame through scaling by a factor of $(1 + z)$, where z is the cosmological redshift at the sampled distance assuming a flat Λ CDM cosmology. All template waveforms are generated using the `IMRPhenomD_NRTidal` waveform in order to match the simulated signals and avoid any systematic errors arising from different implementations across waveform families.

Multiple signals s_1, s_2, \dots, s_N are considered independent of one another and thus the posterior distributions for a given parameter θ_k can be combined straightforwardly

across all signals [218, 58]

$$p(\theta_k | s_1, s_2, \dots, s_N) = p(\theta_k)^{1-N} \prod_{i=1}^N p(\theta_k | s_i) \quad (6.9)$$

where we have assumed the prior $p(\theta_k)$ is the same for all signals.

6.5 Results

In order to combine measurements across an entire population, we transform the posteriors of the equation of state for all signals to posteriors of a common parameter, $R_{1.4}$. Then each signal we analyze constitutes an independent measurement of the same physical quantity, and we can combine posterior distributions across many events following the procedure outlined in the previous section. To simulate a scenario of cumulatively combining each new signal as it occurs, we combine $R_{1.4}$ posteriors one at a time to track the radius constraint (as measured by the 90% credible interval width) as a function of the number of signals included. This also allows for a straightforward conversion to constraint over time, given a merger rate and detector network sensitivity.

For the 321 signals in our LIGO-Virgo network analysis the combined $R_{1.4}$ constraint is shown in Figure 19 for each of the three equations of state we used. As expected, we find a hierarchy in the constraints from the three different equations of state, with a stiffer equation of state leading to a better final precision as a result of the more measurable tidal information in the signals. After combining all signals from EOS 1250, the 90% credible interval on $R_{1.4}$ is approximately 90 meters. For the moderately stiff EOS 895 the final 90% credible interval width is a slightly larger 130 meters. The softest equation of state in our analysis, EOS 487, produced the weakest constraint with a final 90% credible interval of 200 meters. These credible intervals correspond to measurement precision on the true $R_{1.4}$ in each population of 0.7%, 1.1%, and 1.9% respectively.

Constraints at intermediate numbers of signals will depend on the particular order in which the signals are combined, but we attempt to determine a general threshold for 10% precision in two ways: 1. we perform the signal combination for 10 random permutations of the order; 2. we remove all signals with signal-to-noise $\rho > 30$ and combine the remainder of the population to prevent any outside influence from

anomalously loud events. With both methods we find that a 10% precision threshold is achieved after combining roughly 50 signals. This is consistent with other works that have found a better than 10% constraint for similar numbers of signals seen by the LIGO-Virgo network [57, 219]. In Figure 20 we plot the result of combining the 277 signals in the population with $\rho < 30$. The final $R_{1.4}$ constraint for each of the equations of state is a factor of roughly 1.5 larger than was found for the entire population as a consequence of removing the loudest signals.

In previous works it has been shown that imperfect knowledge of the mass distribution of neutron stars can introduce a bias into the equation of state measurement, owing to the mass dependence of the tidal deformability [58, 223]. To investigate the implications of this effect in the context of precision equation of state measurements, we repeat our analysis on the Gaussian distributed mass population using a prior on the component masses that is uniform in the range $1 - 2M_{\odot}$. The combined $R_{1.4}$ constraint results from this analysis can be seen in Figure 21, where the signal ordering is the same as in Figure 19 for the sake of comparison. We find a small but significant bias toward smaller radii in our $R_{1.4}$ measurement for all three equations of state in our analysis, although the statistical uncertainties are not significantly changed. For EOS 1250 and EOS 895, we find the bias is enough to exclude the true value of $R_{1.4}$ at very high confidence after combining about 20 and 100 signals, respectively.

We investigate also the effect on a precision equation of state constraint from a neutron star mass distribution with greater representation of higher mass stars, since larger masses correspond to smaller Λ . To do this we perform our analysis on a population that is drawn uniformly in neutron star masses from $1 - 2M_{\odot}$. The combined $R_{1.4}$ constraint results are shown in Figure 22. We find for each equation of state we analyze the $R_{1.4}$ constraint is essentially unchanged from the Gaussian distributed population analysis, with final measurement precisions ranging from 1 - 2%.

While our LIGO-Virgo analysis includes hundreds of binary neutron star signals to produce a combined constraint, it is not at all certain that the merger rate and detector sensitivity will produce so many signals. To convert our signal-number forecast to a potential time horizon, we estimate the probability of seeing different numbers of events, assuming any population of mergers in the local universe will follow the

universal analytic signal-to-noise distribution described in [7]. We calculate this probability as a function of the total number of events, and we convert that to number of years at the projected sensitivity for the upcoming fourth LIGO observing run (O4). We use the median binary neutron star merger rate estimate $\mathcal{R} = 320 \text{ Gpc}^{-3}\text{yr}^{-1}$ from [8], the projected O4 search volume $VT = 0.016 \text{ Gpc}^3\text{yr}$ from [9], and we assume a detection threshold network signal-to-noise $\rho_t = 9$. The calculated probabilities of seeing 10, 25, and 50 events with $\rho > 10$, consistent with the signals we include in this work, can be seen in Figure 23. We note that O4 is expected to last approximately one year, though we calculate probabilities beyond that timeline to allow for any delays in the planned detector upgrades and to provide a lower limit for future observing runs that are expected to operate with improved sensitivity. We find that while 10 binary neutron star signals with $\rho > 10$ will almost certainly be seen in just 3 years of observation at O4 sensitivity, it will take over 12 years at this sensitivity to have any significant probability of seeing 50 signals.

Planned upgrades are expected to substantially increase detector sensitivity for the fifth observing run and beyond, though no official estimate of the search volume has yet been published. An improved network sensitivity would effectively shift the probability curves in Figure 23 leftward by the factor of improvement in search volume, though we note that even an order of magnitude improvement would likely result in at most 50 signals in several years of observation under the assumptions made here.

Finally, we explore the ability of Cosmic Explorer to precisely measure the equation of state. The extreme sensitivity of the Cosmic Explorer design means that it is expected to be sensitive to the complete population of merging binaries out to a redshift of $z = 1$ [224]. This means that given current merger rate estimates, Cosmic Explorer will likely see hundreds of binary neutron star signals with $\rho > 100$ in a single year of observation, and our simulated population of 335 signals is approximately representative of that set. The combined $R_{1.4}$ constraint for EOS 487 and EOS 895 are shown in Figure 24. We find that for both equations of state a 10% precision threshold is achieved almost immediately, with the precision improving to 0.6% and 0.15% after combining all signals for EOS 487 and EOS 895, respectively. We also note that these constraint projections are likely slight overestimates, as there will be many more signals with $\rho < 100$ seen in one year of observation that would still

contain measurable tidal information. While the combined equation of state measurement will almost certainly be dominated by the louder signals we consider here, it is possible that quieter signals will contribute to improve the constraint somewhat.

We also check whether the Cosmic Explorer constraints are robust to an incorrect choice of mass prior by repeating the analysis using a uniform mass prior from $1-2M_{\odot}$. Systematic biases from an incorrect choice of prior are smaller for louder signals, so we expect that our population of Cosmic Explorer signals will suffer less from this effect. Figure 25 shows the combined $R_{1,4}$ constraints from this analysis for the medium and soft equations of state we investigated, where again the ordering has been preserved from Figure 24 to allow easy comparison. We find there is again a bias toward smaller radii for both EOS 487 and EOS 895, though it is much smaller in absolute terms than that seen in the LIGO-Virgo analysis. Still, the correspondingly smaller statistical uncertainties on our combined measurements make it so the true $R_{1,4}$ values lie right at the upper boundary of the 90% credible interval for both equations of state, emphasizing the need for a good estimate of the neutron star mass distribution even for Cosmic Explorer. As was the case in our LIGO-Virgo analysis, we find the statistical uncertainties on the combined measurements are largely unchanged from the Gaussian mass prior analysis.

6.6 Conclusion

We presented an updated forecast using more plausible equations of state for binary neutron star mergers seen by a LIGO-Virgo network, and new results for the proposed Cosmic Explorer detector. We use the most up-to-date estimates for the range of plausible equations of state and of the merger rate in the local universe. We find that Advanced LIGO will constrain $R_{1,4}$ to within 10% at 90% confidence with the first 50 signals, largely consistent with previous works, and we show that this projection is robust to a change in the mass population of neutron stars. We also extend the projection to find that across the full range of plausible equations of state, Advanced LIGO will be able to measure $R_{1,4}$ to better than about 2% after 321 signals, although the probability of seeing this many signals before third generation detectors become operational is potentially very low. On the other hand we find that the much greater sensitivity of Cosmic Explorer means it will be able to measure $R_{1,4}$ to better than

0.6% at 90% confidence across the full range of plausible equations of state with one year of observation. This precision from Cosmic Explorer will be sufficient to distinguish even similarly soft equations of state from one another at high confidence.

As discussed by Wysocki *et al.*, our analysis confirms that accurate knowledge of the mass distribution of neutron stars in the population of merging binaries is vital to making an unbiased measurement of the equation of state. We find that biases due to an incorrect mass prior can be present even in measurements from a population of loud signals in a third-generation detector like Cosmic Explorer, and as such we emphasize the added importance of efforts to mitigate these biases in the context of precision equation of state measurements.

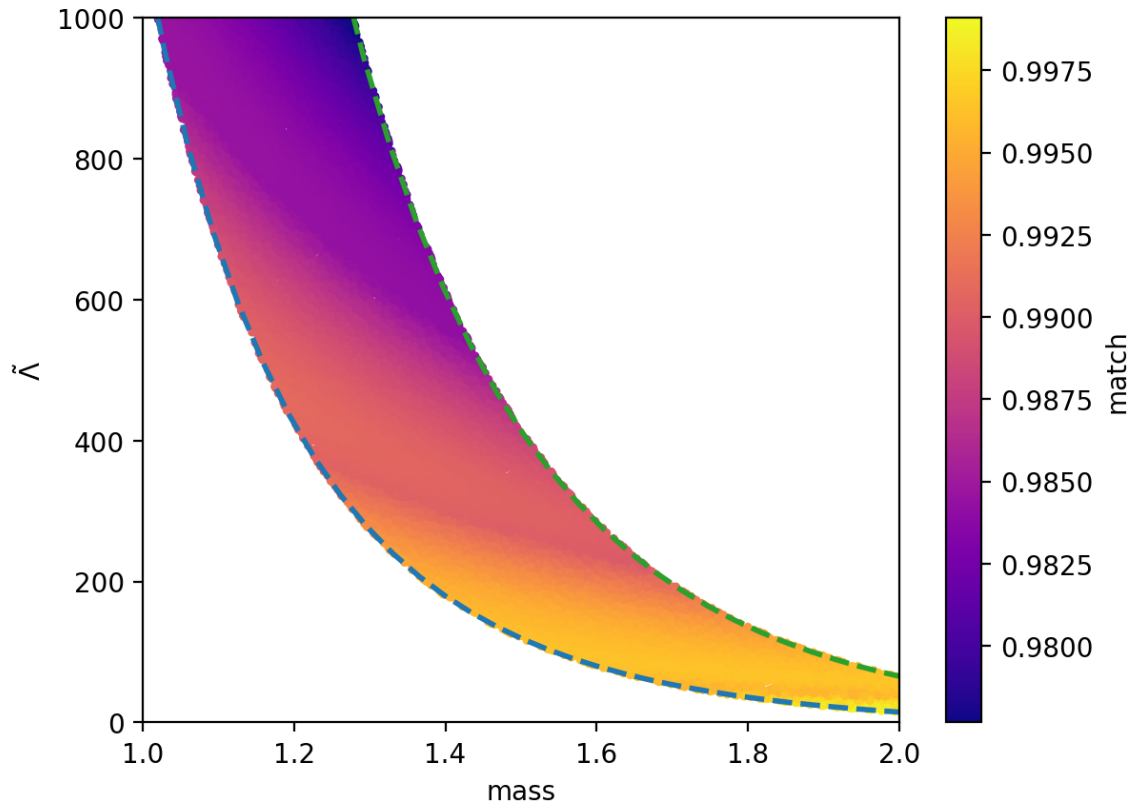


Figure 17: Match between gravitational waveforms for equal mass binaries with and without tidal deformability included. The match is calculated as the noise-weighted overlap between the two waveforms in the frequency range 20 – 2048 Hz using the Advanced LIGO design sensitivity noise curve `aLIGODesignSensitivityP1200087`. Waveforms are generated using masses ranging from $1 - 2M_{\odot}$, and for the waveform including tidal deformability we use values of $\tilde{\Lambda} = \Lambda_1 = \Lambda_2$ that span the range of plausible values between the soft (lower curve) and stiff (upper curve) equations of state selected for our analysis.

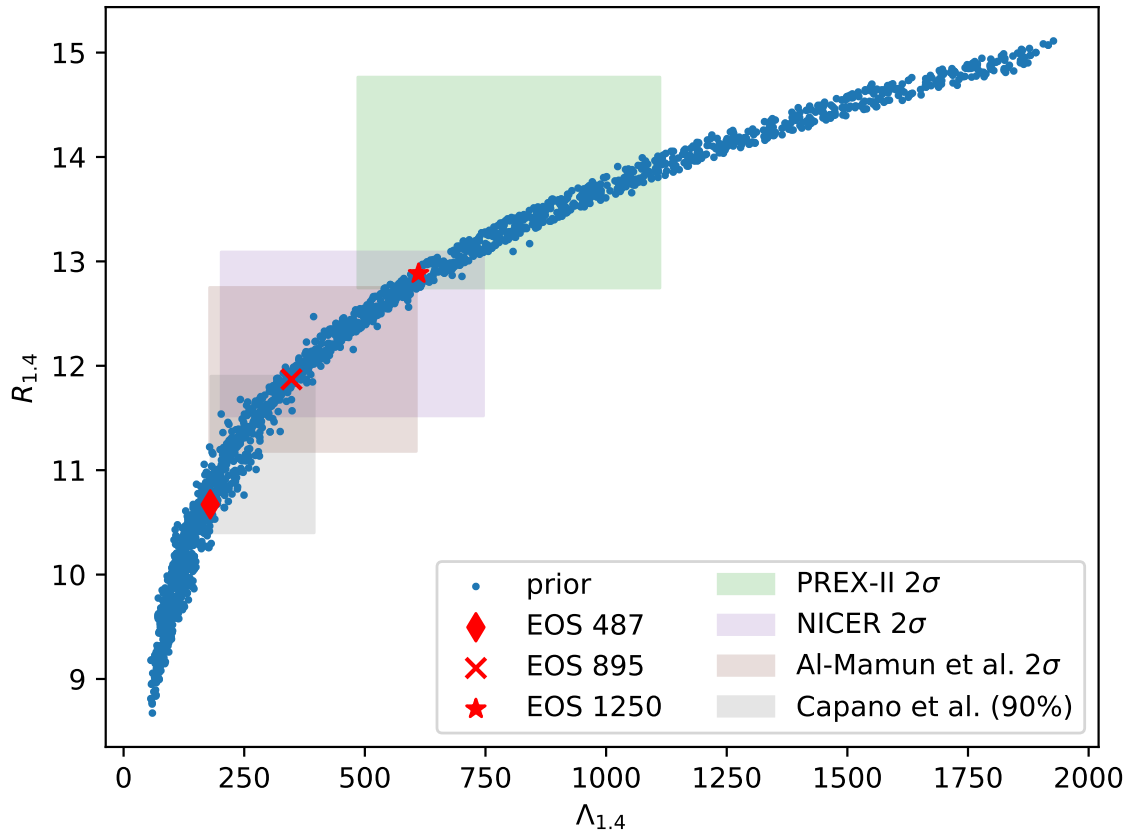


Figure 18: The radius in kilometers and dimensionless tidal deformability of a $1.4M_{\odot}$ neutron star, denoted $R_{1.4}$ and $\Lambda_{1.4}$, for the equations of state used in this work. The soft, medium, and stiff equations of state whose measurability we assess, EOS 487, EOS 895, and EOS 1250, are shown as a red diamond, red cross, and red star, respectively. The $(\Lambda_{1.4}, R_{1.4})$ coordinates for the 2000 equations of state used as a prior distribution in our analysis are shown in blue. Shaded regions represent a selection of constraints on the equation of state from gravitational-wave and electromagnetic observations, and nuclear experiment. The constraints span a significant range with potentially some tension between them. The three equations of state we investigate in this work are chosen to span the majority of the range covered by these constraints.

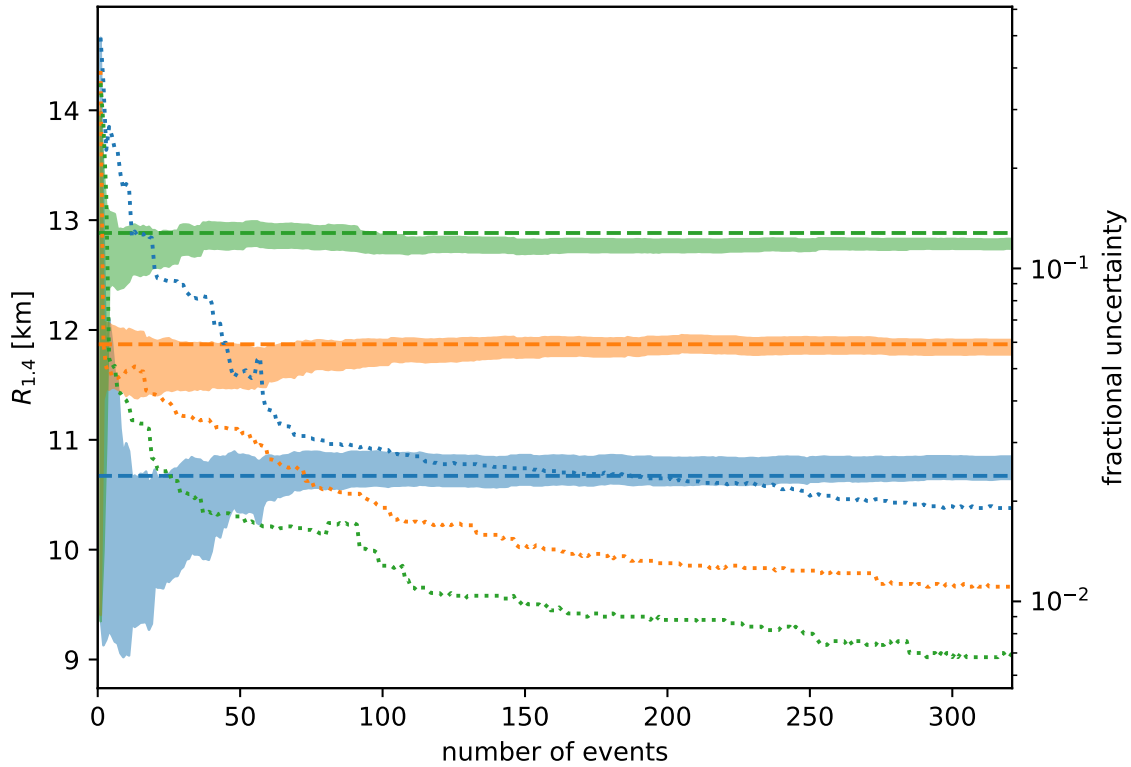


Figure 19: Combined $R_{1.4}$ measurements for our Gaussian mass distributed population in the LIGO-Virgo network. Results are shown for the soft (blue), medium (orange), and stiff (green) equations of state that we used. Signals are combined one at a time to show an updating constraint on the measurement as each signal is added. Shaded regions represent the 90% credible interval for each measurement. The true values of $R_{1.4}$ for each of the equations of state are plotted as horizontal dashed lines in the appropriate color. Dotted lines show the fractional uncertainty in the measurement at each number of signals included, measured as the ratio of the 90% credible interval to the true value of $R_{1.4}$ for a given equation of state.

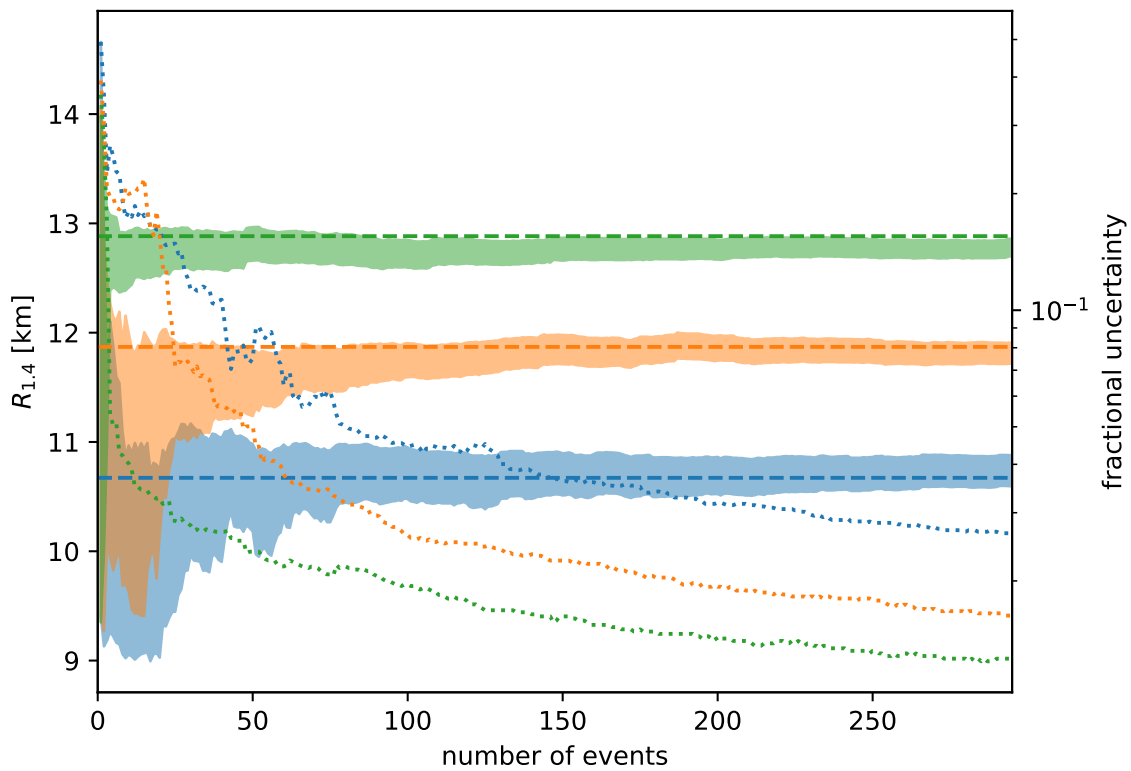


Figure 20: Same as Figure 19 except including only signals with signal-to-noise $\rho < 30$. By removing louder signals we attempt to mitigate any potentially outside effect on the radius constraint from signals that are unlikely to be seen by the LIGO-Virgo network. For the stiff, medium, and soft equations of state we find that a 10% precision measurement on $R_{1,4}$ is reached after 5, 30, and 50 signals, respectively.

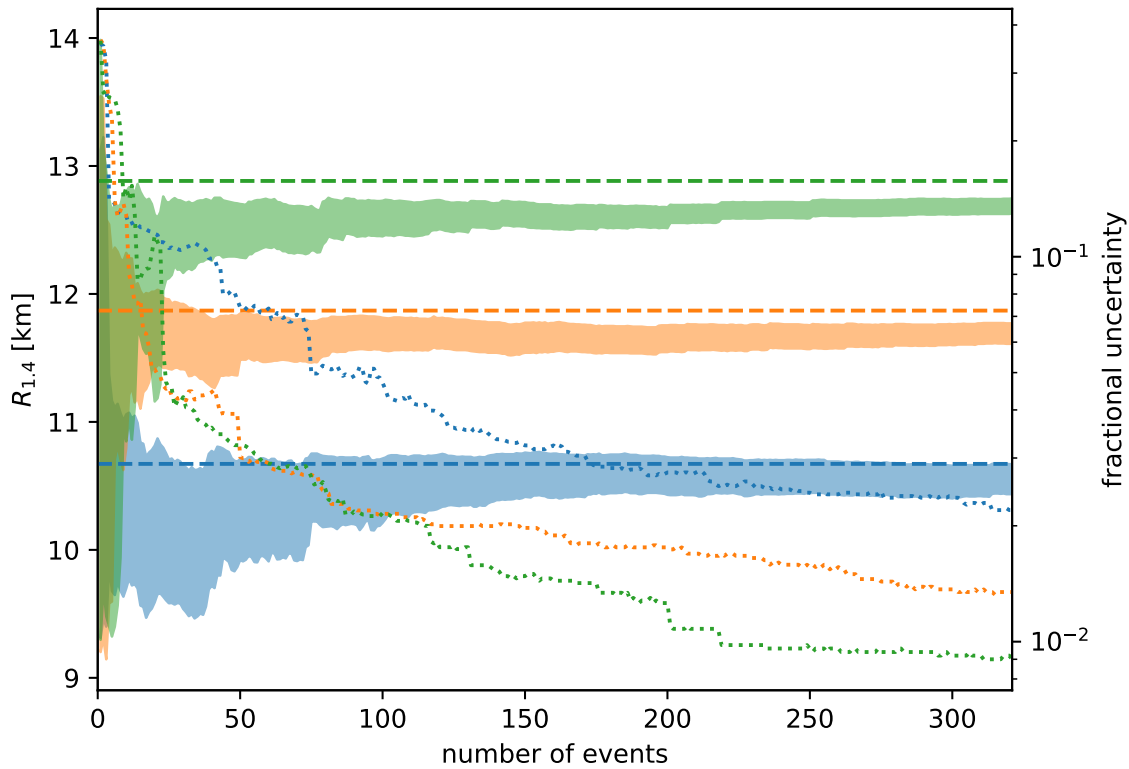


Figure 21: Same as Figure 19 except we recover all signals with a uniform prior on the source-frame component masses from $1 - 2M_{\odot}$. This incorrect choice of mass prior introduces a bias in the equation of state measurement, leading to systematically lower estimates of $R_{1.4}$. We find that for EOS 1250 and EOS 895 the bias causes the true equation of state to be ruled out at high confidence after about 20 and 100 signals, respectively.

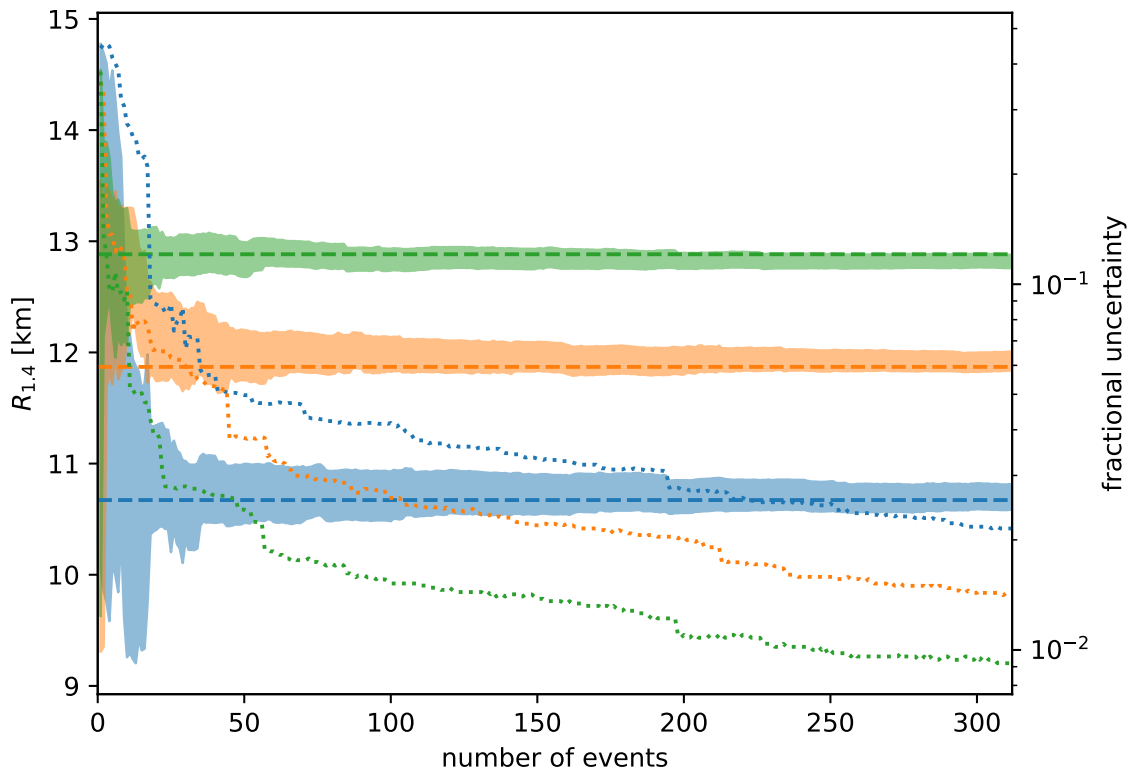


Figure 22: Combined $R_{1.4}$ measurements for our uniform mass population in the LIGO-Virgo network. Source-frame component masses are drawn from $1 - 2M_{\odot}$ to represent a population with more high-mass neutron stars. All signals are recovered with a uniform mass prior from $1 - 2M_{\odot}$ and signals are combined following the same procedure as the Gaussian mass population. We find the combined equation of state measurements from the uniform mass population are essentially unchanged from the Gaussian mass population, with precision on the measurement of $R_{1.4}$ ranging from $1 - 2\%$.

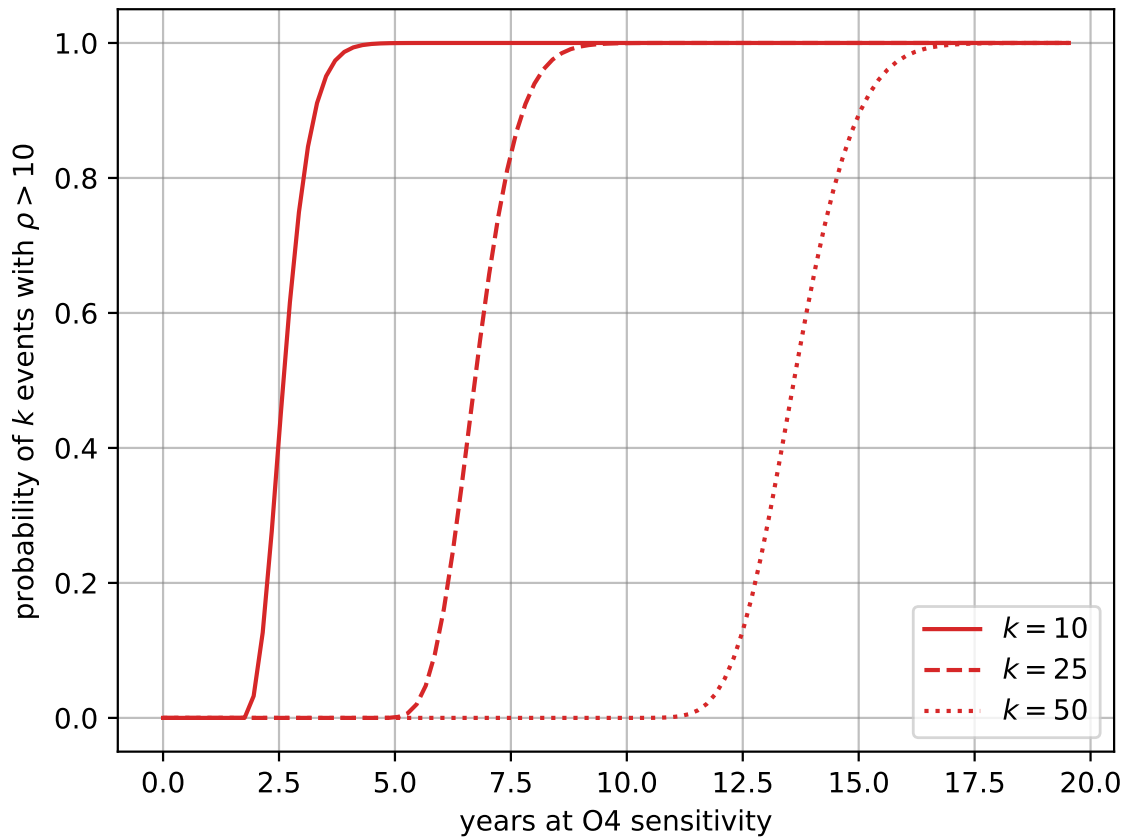


Figure 23: Probability of seeing 10, 25, and 50 events with signal-to-noise $\rho > 10$ over time, assuming the population of merging binary neutron stars in the local universe follows the universal signal-to-noise distribution described in [7]. The probabilities for 10, 25, and 50 events are shown as solid, dashed, and dotted lines, respectively. We use the median binary neutron star merger rate estimate from [8] and the projected sensitive volume for the upcoming fourth observing run (O4) of the Advanced LIGO network [9] to plot probabilities against number of years at O4 sensitivity. We assume a detection threshold network signal-to-noise ratio of 9.

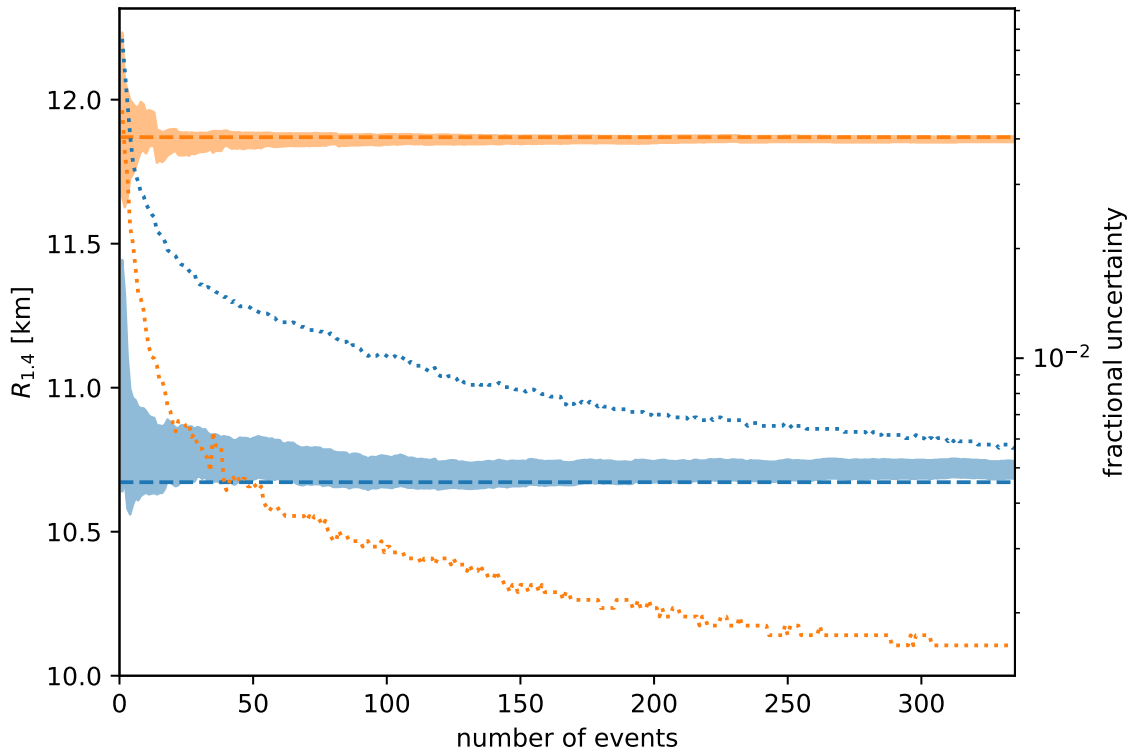


Figure 24: Combined $R_{1,4}$ measurements for our Gaussian mass distributed population in Cosmic Explorer, which is representative of the signals expected in one year of observation. Results are shown for the soft (blue) and medium (orange) equations of state in our analysis. As in Fig. 19 the horizontal dashed lines indicate the true value of $R_{1,4}$ for each equation of state, and the dotted lines show the calculated fractional uncertainty which is defined as the ratio of the 90% credible interval to the true value of $R_{1,4}$. We find that for both equations of state, a 10% precision threshold on the measurement of $R_{1,4}$ is achieved almost immediately, consistent with the third-generation detector result from [10]. The measurement precision improves to 0.6% and 0.15% for the soft and medium equations of state, respectively, after all signals are combined.

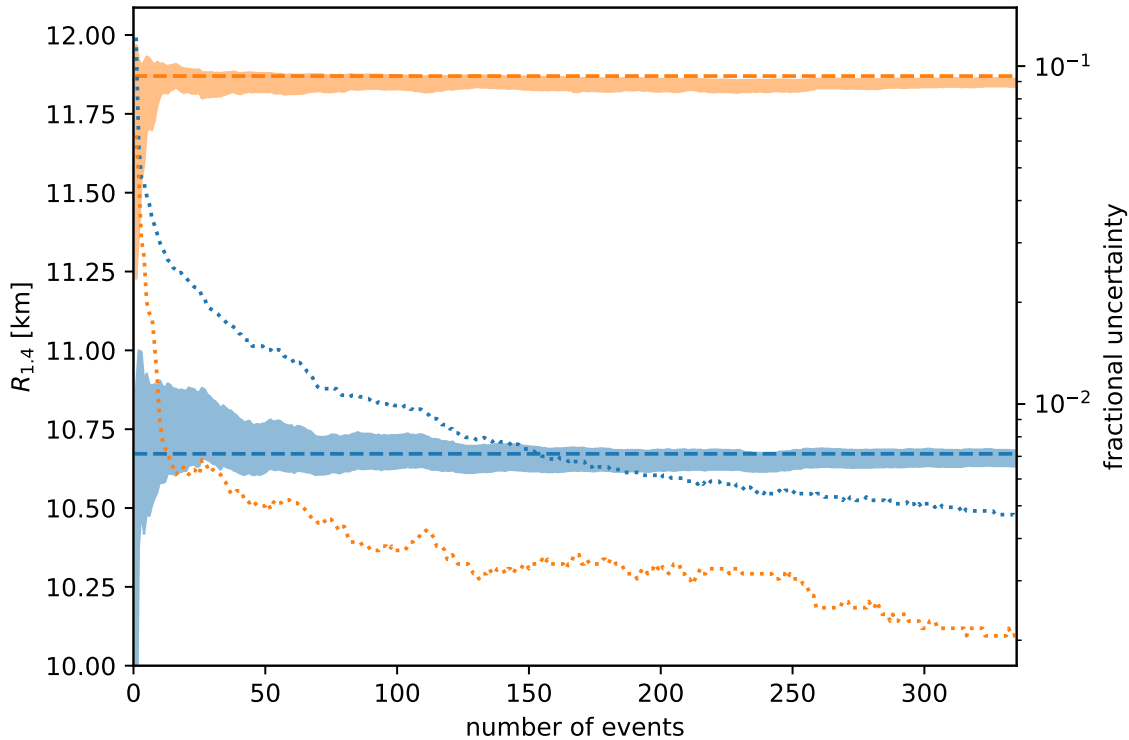


Figure 25: Same as Figure 24 except we recover signals using a uniform mass prior from $1 - 2M_{\odot}$. The ordering of signals has been preserved from the Gaussian prior analysis for comparison, and it can be seen that the combined constraints for both equations of state is again biased toward smaller radii as a result of the incorrect mass prior. The bias is smaller than what was seen in our LIGO-Virgo analysis as a result of the much louder signals in the Cosmic Explorer population, however the true values for both equations of state are still found at the edge of their respective 90% credible interval because of the correspondingly smaller statistical uncertainties on these measurements.

Chapter 7

Conclusions

In the current era of gravitational-wave astrophysics we are moving beyond first direct detections and first multimessenger observations, to now making routine discoveries that deepen our understanding of the compact objects in our cosmic neighborhood. The LIGO-Virgo gravitational-wave detector network has detected 52 confirmed binary merger observations so far, and the detection rate has only accelerated as improved detector sensitivity extends our reach deeper into the universe. From the two observed binary neutron star mergers, our knowledge of the dynamics of these events and of neutron star physics has grown dramatically. They have provided confirmation of binary neutron star mergers as a source of short gamma-ray bursts, and also as important sites of heavy element production through r -process nucleosynthesis that can help explain observed chemical abundances. They have also shown that it is possible to measure the tidal information in a gravitational-wave signal to meaningfully update our constraints on the nuclear equation of state. As the LIGO-Virgo detectors approach their design sensitivity, and as third-generation detectors begin to come online, we expect to see many more binary neutron star mergers in the coming years. We anticipate that these new detections will provide even further insights into the physics of neutron stars.

In this thesis we have studied binary neutron star mergers, through a combination of observations and computational modeling. Specifically we explore the ability of a gravitational-wave analysis to extract physical parameters of the binary system, and of the neutron stars involved in the merger. We investigate the impact of multimessenger information on a gravitational-wave analysis, and we study the measurability of the

nuclear equation of state, both now and in the future.

We have presented an analysis of the binary neutron star merger GW170817 informed by electromagnetic distance measurements of its identified host galaxy, and we demonstrated that using an independent distance measurement in a gravitational-wave analysis can break the distance-inclination degeneracy to allow for much tighter constraints on the inclination angle of the binary. We find our improved measurement of the inclination supports models for a structured relativistic jet and its afterglow emission being viewed off-axis.

We have presented measurements of the tidal deformabilities and radii of the neutron stars in GW170817. Our analysis imposed a physical constraint to require that both neutron stars obey the same equation of state, and we used a prior on the leading order tidal parameter constructed to contain all physical models of the equation of state without biasing the measurement toward any particular model. We note that the methodology we employed could be adapted for the analysis of future binary neutron star merger events with similar masses. We find our results are broadly consistent with several other studies [198, 210, 225, 142] which employed various methods to measure the tidal deformabilities and radii in their own analyses of GW170817.

We have presented a likelihood model developed for *PyCBC Inference* that uses the relative binning parameter estimation technique to reduce computational cost for potential multimessenger gravitational-wave sources. We extended the work of previous implementations to make our relative likelihood model a coherent network statistic so that it can additionally measure sky locations. We validated the relative model on populations of simulated binary neutron star and simulated neutron star–black hole merger signals, and we showed that it is possible to seed the relative analysis with the best-fit template parameters from a low-latency search pipeline. We found that the parameter estimation for all signals in our simulated populations completed in less than 20 minutes, with sky localization and intrinsic parameter estimates that are comparable to analyses done with a standard non-relative likelihood.

We have presented a comprehensive study of the future prospects for a precise equation of state measurement from Advanced LIGO and Cosmic Explorer. We explored the measurability of the equation of state across the full parameter space

allowed by combined constraints from astrophysical observations and nuclear experiments. We showed that a precision threshold for measurements to distinguish between substantially similar theoretical models for the equation of state is equivalent to measuring the radius of a $1.4M_{\odot}$ neutron star to better than 2%, and we presented a framework for combining individual equation of state measurements across entire populations to produce a combined, high-precision measurement. We found it is unlikely that Advanced LIGO will achieve 2% precision in the next observing runs given current estimates of the merger rate for binary neutron stars, however Cosmic Explorer will measure the equation of state to better than 1% within one year of operation. Our framework can be directly applied to any future signals from binary neutron star mergers, and we anticipate that the resulting precise knowledge of the true equation of state will be invaluable for efforts to model these merger events and their associated kilonovae.

Bibliography

- [1] K. Ackley et al. Neutron Star Extreme Matter Observatory: A kilohertz-band gravitational-wave detector in the global network. *Publ. Astron. Soc. Austral.*, 37:e047, 2020.
- [2] Michele Cantiello et al. A Precise Distance to the Host Galaxy of the Binary Neutron Star Merger GW170817 Using Surface Brightness Fluctuations. *Astrophys. J.*, 854(2):L31, 2018.
- [3] Ben Farr et al. Parameter estimation on gravitational waves from neutron-star binaries with spinning components. *Astrophys. J.*, 825(2):116, 2016.
- [4] Thibault Damour, Alessandro Nagar, and Loic Villain. Measurability of the tidal polarizability of neutron stars in late-inspiral gravitational-wave signals. *Phys. Rev.*, D85:123007, 2012.
- [5] B.P. Abbott et al. GW170817: Observation of Gravitational Waves from a Binary Neutron Star Inspiral. *Phys. Rev. Lett.*, 119(16):161101, 2017.
- [6] Feryal Özel and Paulo Freire. Masses, Radii, and the Equation of State of Neutron Stars. *Ann. Rev. Astron. Astrophys.*, 54:401–440, 2016.
- [7] Hsin-Yu Chen and Daniel E. Holz. The Loudest Gravitational Wave Events. 9 2014.
- [8] R. Abbott et al. Population Properties of Compact Objects from the Second LIGO-Virgo Gravitational-Wave Transient Catalog. *Astrophys. J. Lett.*, 913(1):L7, 2021.

- [9] Benjamin P. Abbott et al. Prospects for Observing and Localizing Gravitational-Wave Transients with Advanced LIGO, Advanced Virgo and KAGRA. 2013. [Living Rev. Rel.19,1(2016)].
- [10] Costantino Pacilio, Andrea Maselli, Margherita Fasano, and Paolo Pani. Ranking the Love for the neutron star equation of state: the need for third-generation detectors. 4 2021.
- [11] J. Aasi et al. Advanced LIGO. *Class. Quantum Grav.*, 32:074001, 2015.
- [12] B. P. Abbott et al. Observation of Gravitational Waves from a Binary Black Hole Merger. *Phys. Rev. Lett.*, 116(6):061102, 2016.
- [13] F. Acernese et al. Advanced Virgo: a second-generation interferometric gravitational wave detector. *Class. Quant. Grav.*, 32(2):024001, 2015.
- [14] B. P. Abbott et al. Multi-messenger Observations of a Binary Neutron Star Merger. *Astrophys. J.*, 848:L12, 2017.
- [15] B.P. Abbott et al. GWTC-1: A Gravitational-Wave Transient Catalog of Compact Binary Mergers Observed by LIGO and Virgo during the First and Second Observing Runs. *Phys. Rev. X*, 9(3):031040, 2019.
- [16] R. Abbott et al. GWTC-2: Compact Binary Coalescences Observed by LIGO and Virgo During the First Half of the Third Observing Run. *Phys. Rev. X*, 11:021053, 2021.
- [17] R. Abbott et al. Observation of Gravitational Waves from Two Neutron Star–Black Hole Coalescences. *Astrophys. J. Lett.*, 915(1):L5, 2021.
- [18] R. Abbott et al. GW190814: Gravitational Waves from the Coalescence of a 23 Solar Mass Black Hole with a 2.6 Solar Mass Compact Object. *Astrophys. J. Lett.*, 896(2):L44, 2020.
- [19] David Reitze et al. Cosmic Explorer: The U.S. Contribution to Gravitational-Wave Astronomy beyond LIGO. *Bull. Am. Astron. Soc.*, 51(7):035, 2019.
- [20] M. Punturo et al. The Einstein Telescope: A third-generation gravitational wave observatory. *Class. Quant. Grav.*, 27:194002, 2010.

- [21] Benjamin P. Abbott et al. Sensitivity of the Advanced LIGO detectors at the beginning of gravitational wave astronomy. *Phys. Rev.*, D93(11):112004, 2016. [Addendum: *Phys. Rev.* D97,no.5,059901(2018)].
- [22] A. Goldstein et al. An Ordinary Short Gamma-Ray Burst with Extraordinary Implications: Fermi-GBM Detection of GRB 170817A. *Astrophys. J.*, 848(2):L14, 2017.
- [23] V. Savchenko et al. INTEGRAL Detection of the First Prompt Gamma-Ray Signal Coincident with the Gravitational-wave Event GW170817. *Astrophys. J.*, 848(2):L15, 2017.
- [24] R. Chornock et al. The Electromagnetic Counterpart of the Binary Neutron Star Merger LIGO/VIRGO GW170817. IV. Detection of Near-infrared Signatures of r-process Nucleosynthesis with Gemini-South. *Astrophys. J.*, 848(2):L19, 2017.
- [25] P. S. Cowperthwaite et al. The Electromagnetic Counterpart of the Binary Neutron Star Merger LIGO/Virgo GW170817. II. UV, Optical, and Near-infrared Light Curves and Comparison to Kilonova Models. *Astrophys. J.*, 848(2):L17, 2017.
- [26] M. M. Kasliwal et al. Illuminating Gravitational Waves: A Concordant Picture of Photons from a Neutron Star Merger. *Science*, 358:1559, 2017.
- [27] M. Nicholl et al. The Electromagnetic Counterpart of the Binary Neutron Star Merger LIGO/VIRGO GW170817. III. Optical and UV Spectra of a Blue Kilonova From Fast Polar Ejecta. *Astrophys. J.*, 848(2):L18, 2017.
- [28] E. Pian et al. Spectroscopic identification of r-process nucleosynthesis in a double neutron star merger. *Nature*, 551:67–70, 2017.
- [29] S. J. Smartt et al. A kilonova as the electromagnetic counterpart to a gravitational-wave source. *Nature*, 551(7678):75–79, 2017.
- [30] V. Ashley Villar et al. The Combined Ultraviolet, Optical, and Near-Infrared Light Curves of the Kilonova Associated with the Binary Neutron Star Merger GW170817: Unified Data Set, Analytic Models, and Physical Implications. *Astrophys. J.*, 851(1):L21, 2017.

- [31] H. Wahlquist. The Doppler Response to Gravitational Waves From a Binary Star Source. *Gen. Rel. Grav.*, 19:1101–1113, 1987.
- [32] Samantha A. Usman, Joseph C. Mills, and Stephen Fairhurst. Constraining the Inclinations of Binary Mergers from Gravitational-wave Observations. *Astrophys. J.*, 877(2):82, 2019.
- [33] M. Soares-Santos et al. The Electromagnetic Counterpart of the Binary Neutron Star Merger LIGO/Virgo GW170817. I. Discovery of the Optical Counterpart Using the Dark Energy Camera. *Astrophys. J.*, 848(2):L16, 2017.
- [34] Ben Margalit and Brian D. Metzger. The Multi-Messenger Matrix: the Future of Neutron Star Merger Constraints on the Nuclear Equation of State. *Astrophys. J. Lett.*, 880(1):L15, 2019.
- [35] C. M. Biwer, Collin D. Capano, Soumi De, Miriam Cabero, Duncan A. Brown, Alexander H. Nitz, and V. Raymond. PyCBC Inference: A Python-based parameter estimation toolkit for compact binary coalescence signals. 2018.
- [36] Michael Pürrer. Frequency domain reduced order models for gravitational waves from aligned-spin compact binaries. *Class. Quant. Grav.*, 31(19):195010, 2014.
- [37] Priscilla Canizares, Scott E. Field, Jonathan Gair, Vivien Raymond, Rory Smith, and Manuel Tiglio. Accelerated gravitational-wave parameter estimation with reduced order modeling. *Phys. Rev. Lett.*, 114(7):071104, 2015.
- [38] Jonathan Blackman, Bela Szilagyi, Chad R. Galley, and Manuel Tiglio. Sparse Representations of Gravitational Waves from Precessing Compact Binaries. *Phys. Rev. Lett.*, 113(2):021101, 2014.
- [39] Michael Pürrer. Frequency domain reduced order model of aligned-spin effective-one-body waveforms with generic mass-ratios and spins. *Phys. Rev. D*, 93(6):064041, 2016.
- [40] Scott E. Field, Chad R. Galley, Jan S. Hesthaven, Jason Kaye, and Manuel Tiglio. Fast prediction and evaluation of gravitational waveforms using surrogate models. *Phys. Rev. X*, 4(3):031006, 2014.

- [41] Sarah Caudill, Scott E. Field, Chad R. Galley, Frank Herrmann, and Manuel Tiglio. Reduced Basis representations of multi-mode black hole ringdown gravitational waves. *Class. Quant. Grav.*, 29:095016, 2012.
- [42] Scott E. Field, Chad R. Galley, Frank Herrmann, Jan S. Hesthaven, Evan Ochsner, and Manuel Tiglio. Reduced basis catalogs for gravitational wave templates. *Phys. Rev. Lett.*, 106:221102, 2011.
- [43] Priscilla Canizares, Scott E. Field, Jonathan R. Gair, and Manuel Tiglio. Gravitational wave parameter estimation with compressed likelihood evaluations. *Phys. Rev. D*, 87(12):124005, 2013.
- [44] Jonathan Blackman, Scott E. Field, Chad R. Galley, Béla Szilágyi, Mark A. Scheel, Manuel Tiglio, and Daniel A. Hemberger. Fast and Accurate Prediction of Numerical Relativity Waveforms from Binary Black Hole Coalescences Using Surrogate Models. *Phys. Rev. Lett.*, 115(12):121102, 2015.
- [45] Neil J. Cornish. Fast fisher matrices and lazy likelihoods, 2013.
- [46] Barak Zackay, Liang Dai, and Tejaswi Venumadhav. Relative Binning and Fast Likelihood Evaluation for Gravitational Wave Parameter Estimation. 6 2018.
- [47] LIGO Scientific Collaboration. LALSuite: LIGO Scientific Collaboration Algorithm Library Suite, December 2020.
- [48] Éanna É. Flanagan and Tanja Hinderer. Constraining neutron star tidal Love numbers with gravitational wave detectors. *Phys. Rev.*, D77:021502, 2008.
- [49] Thibault Damour and Alessandro Nagar. Effective One Body description of tidal effects in inspiralling compact binaries. *Phys. Rev.*, D81:084016, 2010.
- [50] Donato Bini, Thibault Damour, and Guillaume Faye. Effective action approach to higher-order relativistic tidal interactions in binary systems and their effective one body description. *Phys. Rev. D*, 85:124034, 2012.
- [51] Sebastiano Bernuzzi, Alessandro Nagar, Tim Dietrich, and Thibault Damour. Modeling the Dynamics of Tidally Interacting Binary Neutron Stars up to the Merger. *Phys. Rev. Lett.*, 114(16):161103, 2015.

- [52] Kenta Hotokezaka, Koutarou Kyutoku, Hirotada Okawa, and Masaru Shibata. Exploring tidal effects of coalescing binary neutron stars in numerical relativity. II. Long-term simulations. *Phys. Rev. D*, 91(6):064060, 2015.
- [53] Alessandro Nagar, Francesco Messina, Piero Retteno, Donato Bini, Thibault Damour, Andrea Geralico, Sarp Akcay, and Sebastiano Bernuzzi. Nonlinear-in-spin effects in effective-one-body waveform models of spin-aligned, inspiralling, neutron star binaries. *Phys. Rev. D*, 99(4):044007, 2019.
- [54] Sarp Akcay, Sebastiano Bernuzzi, Francesco Messina, Alessandro Nagar, Néstor Ortiz, and Piero Retteno. Effective-one-body multipolar waveform for tidally interacting binary neutron stars up to merger. *Phys. Rev. D*, 99(4):044051, 2019.
- [55] Ian Harry and Tanja Hinderer. Observing and measuring the neutron-star equation-of-state in spinning binary neutron star systems. *Class. Quant. Grav.*, 35(14):145010, 2018.
- [56] C. M. Caves. Quantum Mechanical Noise in an Interferometer. *Phys. Rev. D*, 23:1693–1708, 1981.
- [57] Benjamin D. Lackey and Leslie Wade. Reconstructing the neutron-star equation of state with gravitational-wave detectors from a realistic population of inspiralling binary neutron stars. *Phys. Rev.*, D91(4):043002, 2015.
- [58] Michalis Agathos, Jeroen Meidam, Walter Del Pozzo, Tjonnie G. F. Li, Marco Tompitak, John Veitch, Salvatore Vitale, and Chris Van Den Broeck. Constraining the neutron star equation of state with gravitational wave signals from coalescing binary neutron stars. *Phys. Rev.*, D92(2):023012, 2015.
- [59] Michael McNeil Forbes, Sukanta Bose, Sanjay Reddy, Dake Zhou, Arunava Mukherjee, and Soumi De. Constraining the neutron-matter equation of state with gravitational waves. *Phys. Rev. D*, 100(8):083010, 2019.
- [60] Zack Carson, Katerina Chatziioannou, Carl-Johan Haster, Kent Yagi, and Nicolás Yunes. Equation-of-state insensitive relations after GW170817. *Phys. Rev. D*, 99(8):083016, 2019.

- [61] Philippe Landry, Reed Essick, and Katerina Chatziioannou. Nonparametric constraints on neutron star matter with existing and upcoming gravitational wave and pulsar observations. *Phys. Rev. D*, 101(12):123007, 2020.
- [62] L. S. Finn and D. F. Chernoff. Observing binary inspiral in gravitational radiation: One interferometer. *Phys. Rev. D*, 47:2198–2219, March 1993.
- [63] Curt Cutler and Eanna E. Flanagan. Gravitational waves from merging compact binaries: How accurately can one extract the binary’s parameters from the inspiral wave form? *Phys. Rev.*, D49:2658–2697, 1994.
- [64] David Nicholson and Alberto Vecchio. Bayesian bounds on parameter estimation accuracy for compact coalescing binary gravitational wave signals. *Phys. Rev.*, D57:4588–4599, 1998.
- [65] Nelson Christensen and Renate Meyer. Using Markov chain Monte Carlo methods for estimating parameters with gravitational radiation data. *Phys. Rev.*, D64:022001, 2001.
- [66] Thomas Bayes and Richard Price. An essay towards solving a problem in the doctrine of chances. *Phil. Trans. Roy. Soc. Lond.*, 53:370–418, 1763.
- [67] E. T. Jaynes. *Probability Theory: The Logic of Science*. Cambridge University Press, Cambridge, 2003.
- [68] L A Wainstein and V D Zubakov. *Extraction of signals from noise*. Prentice-Hall, Englewood Cliffs, NJ, 1962.
- [69] Nelson Christensen, Rejean J. Dupuis, Graham Woan, and Renate Meyer. A Metropolis-Hastings algorithm for extracting periodic gravitational wave signals from laser interferometric detector data. *Phys. Rev. D*, 70:022001, 2004.
- [70] Neal Madras and Alan D. Sokal. The Pivot algorithm: a highly efficient Monte Carlo method for selfavoiding walk. *J. Statist. Phys.*, 50:109–186, 1988.
- [71] W. D. Vousden, W. M. Farr, and I. Mandel. Dynamic temperature selection for parallel tempering in Markov chain Monte Carlo simulations. *Monthly Notices of the Royal Astronomical Society*, 455(2):1919–1937, 2016.

- [72] J. Skilling. Nested sampling for general Bayesian computation. *Bayesian Analysis*, 1(4):833–860, 2006.
- [73] Farhan Feroz and M. P. Hobson. Multimodal nested sampling: an efficient and robust alternative to MCMC methods for astronomical data analysis. *Mon. Not. Roy. Astron. Soc.*, 384:449, 2008.
- [74] Joshua S Speagle. dynesty: a dynamic nested sampling package for estimating bayesian posteriors and evidences. *Monthly Notices of the Royal Astronomical Society*, 493(3):3132–3158, Feb 2020.
- [75] F. Feroz, M. P. Hobson, and M. Bridges. MultiNest: an efficient and robust Bayesian inference tool for cosmology and particle physics. *Mon. Not. Roy. Astron. Soc.*, 398:1601–1614, 2009.
- [76] K. S. Thorne. THREE HUNDRED YEARS OF GRAVITATION. 1987.
- [77] P. C. Peters. Gravitational Radiation and the Motion of Two Point Masses. *Phys. Rev.*, 136:B1224–B1232, 1964.
- [78] Tanja Hinderer. Tidal Love numbers of neutron stars. *Astrophys. J.*, 677:1216–1220, 2008.
- [79] P. C. Peters and J. Mathews. Gravitational radiation from point masses in a Keplerian orbit. *Phys. Rev.*, 131:435–439, 1963.
- [80] Tanja Hinderer, Benjamin D. Lackey, Ryan N. Lang, and Jocelyn S. Read. Tidal deformability of neutron stars with realistic equations of state and their gravitational wave signatures in binary inspiral. *Phys. Rev. D*, 81:123016, 2010.
- [81] Vitor Cardoso, Leonardo Gualtieri, Carlos Herdeiro, and Ulrich Sperhake. Exploring New Physics Frontiers Through Numerical Relativity. *Living Rev. Relativity*, 18:1, 2015.
- [82] S. A. Teukolsky. Rotating black holes - separable wave equations for gravitational and electromagnetic perturbations. *Phys. Rev. Lett.*, 29:1114–1118, 1972.

- [83] Emanuele Berti, Vitor Cardoso, and Andrei O. Starinets. Quasinormal modes of black holes and black branes. *Class. Quant. Grav.*, 26:163001, 2009.
- [84] A. Buonanno and T. Damour. Effective one-body approach to general relativistic two-body dynamics. *Phys. Rev.*, D59:084006, 1999.
- [85] Alessandra Buonanno and Thibault Damour. Transition from inspiral to plunge in binary black hole coalescences. *Phys. Rev.*, D62:064015, 2000.
- [86] Thibault Damour, Piotr Jaranowski, and Gerhard Schaefers. On the determination of the last stable orbit for circular general relativistic binaries at the third postNewtonian approximation. *Phys. Rev.*, D62:084011, 2000.
- [87] Thibault Damour. Coalescence of two spinning black holes: an effective one-body approach. *Phys. Rev.*, D64:124013, 2001.
- [88] Parameswaran Ajith et al. Phenomenological template family for black-hole coalescence waveforms. *Class. Quant. Grav.*, 24:S689–S700, 2007.
- [89] P. Ajith et al. Inspiral-merger-ringdown waveforms for black-hole binaries with non-precessing spins. *Phys. Rev. Lett.*, 106:241101, 2011.
- [90] L. Santamaria et al. Matching post-Newtonian and numerical relativity waveforms: systematic errors and a new phenomenological model for non-precessing black hole binaries. *Phys. Rev.*, D82:064016, 2010.
- [91] Luc Blanchet. Gravitational radiation from post-newtonian sources and inspiralling compact binaries. *Living Reviews in Relativity*, 9(1):4, Jun 2006.
- [92] B. S. Sathyaprakash and S. V. Dhurandhar. Choice of filters for the detection of gravitational waves from coalescing binaries. *Phys. Rev.*, D44:3819–3834, 1991.
- [93] Alessandra Buonanno, Bala Iyer, Evan Ochsner, Yi Pan, and B. S. Sathyaprakash. Comparison of post-Newtonian templates for compact binary inspiral signals in gravitational-wave detectors. *Phys. Rev.*, D80:084043, 2009.
- [94] K. G. Arun, Alessandra Buonanno, Guillaume Faye, and Evan Ochsner. Higher-order spin effects in the amplitude and phase of gravitational waveforms emitted

- by inspiraling compact binaries: Ready-to-use gravitational waveforms. *Phys. Rev.*, D79:104023, 2009. [Erratum: *Phys. Rev.*D84,049901(2011)].
- [95] Balazs Mikoczi, Matyas Vasuth, and Laszlo A. Gergely. Self-interaction spin effects in inspiraling compact binaries. *Phys. Rev.*, D71:124043, 2005.
- [96] Alejandro Bohé, Sylvain Marsat, and Luc Blanchet. Next-to-next-to-leading order spin-orbit effects in the gravitational wave flux and orbital phasing of compact binaries. *Class. Quant. Grav.*, 30:135009, 2013.
- [97] Justin Vines, Éanna É. Flanagan, and Tanja Hinderer. *Phys. Rev. D*, 83:084051, Apr 2011.
- [98] Sascha Husa, Sebastian Khan, Mark Hannam, Michael Pürrer, Frank Ohme, Xisco Jiménez Forteza, and Alejandro Bohé. Frequency-domain gravitational waves from nonprecessing black-hole binaries. I. New numerical waveforms and anatomy of the signal. *Phys. Rev. D*, 93(4):044006, 2016.
- [99] Sebastian Khan, Sascha Husa, Mark Hannam, Frank Ohme, Michael Pürrer, Xisco Jiménez Forteza, and Alejandro Bohé. Frequency-domain gravitational waves from nonprecessing black-hole binaries. II. A phenomenological model for the advanced detector era. *Phys. Rev. D*, 93(4):044007, 2016.
- [100] Tim Dietrich, Sebastiano Bernuzzi, and Wolfgang Tichy. Closed-form tidal approximants for binary neutron star gravitational waveforms constructed from high-resolution numerical relativity simulations. *Phys. Rev. D*, 96(12):121501, 2017.
- [101] R. A. Mercer et al. LIGO Algorithm Library, 2017. <https://git.ligo.org/lscsoft/lalsuite>.
- [102] Daniel Foreman-Mackey, David W. Hogg, Dustin Lang, and Jonathan Goodman. emcee: The mcmc hammer. *Publications of the Astronomical Society of the Pacific*, 125(925):306–312, Mar 2013.
- [103] W. D. Vousden, W. M. Farr, and I. Mandel. Dynamic temperature selection for parallel tempering in markov chain monte carlo simulations. *Monthly Notices of the Royal Astronomical Society*, 455(2):1919–1937, Nov 2015.

- [104] Neil J. Cornish. Fast Fisher Matrices and Lazy Likelihoods. 7 2010.
- [105] Daniel Finstad and Duncan A. Brown. Fast Parameter Estimation of Binary Mergers for Multimessenger Follow-up. *Astrophys. J. Lett.*, 905(1):L9, 2020.
- [106] D. A. Coulter et al. Swope Supernova Survey 2017a (SSS17a), the Optical Counterpart to a Gravitational Wave Source. *Science*, 2017. [Science358,1556(2017)].
- [107] Stefano Valenti, David J. Sand, Sheng Yang, Enrico Cappellaro, Leonardo Tartaglia, Alessandra Corsi, Saurabh W. Jha, Daniel E. Reichart, Joshua Haislip, and Vladimir Kouprianov. The discovery of the electromagnetic counterpart of GW170817: kilonova AT 2017gfo/DLT17ck. *Astrophys. J.*, 848(2):L24, 2017.
- [108] K. D. Alexander et al. The Electromagnetic Counterpart of the Binary Neutron Star Merger LIGO/VIRGO GW170817. VI. Radio Constraints on a Relativistic Jet and Predictions for Late-Time Emission from the Kilonova Ejecta. *Astrophys. J.*, 848(2):L21, 2017.
- [109] K. D. Alexander, R. Margutti, P. K. Blanchard, W. Fong, E. Berger, A. Hajela, T. Eftekhari, R. Chornock, P. S. Cowperthwaite, D. Giannios, C. Guidorzi, A. Kathirgamaraju, A. MacFadyen, B. D. Metzger, M. Nicholl, L. Sironi, V. A. Villar, P. K. G. Williams, X. Xie, and J. Zrake. A Decline in the X-ray through Radio Emission from GW170817 Continues to Support an Off-Axis Structured Jet. *ArXiv e-prints*, May 2018.
- [110] Davide Lazzati, Rosalba Perna, Brian J. Morsony, Diego López-Cámara, Matteo Cantiello, Riccardo Ciolfi, Bruno Giacomazzo, and Jared C. Workman. Late time afterglow observations reveal a collimated relativistic jet in the ejecta of the binary neutron star merger GW170817. 2017.
- [111] Raffaella Margutti et al. The Electromagnetic Counterpart of the Binary Neutron Star Merger LIGO/VIRGO GW170817. V. Rising X-ray Emission from an Off-Axis Jet. *Astrophys. J.*, 848(2):L20, 2017.
- [112] R. Margutti et al. The Binary Neutron Star Event LIGO/Virgo GW170817 160 Days after Merger: Synchrotron Emission across the Electromagnetic Spectrum. *Astrophys. J.*, 856(1):L18, 2018.

- [113] K. P. Mooley et al. A mildly relativistic wide-angle outflow in the neutron star merger GW170817. *Nature*, 554:207, 2018.
- [114] XiLong Fan, Christopher Messenger, and Ik Siong Heng. A Bayesian approach to multi-messenger astronomy: Identification of gravitational-wave host galaxies. *Astrophys. J.*, 795(1):43, 2014.
- [115] Ilya Mandel. The Orbit of GW170817 Was Inclined by Less Than 28° to the Line of Sight. *Astrophys. J.*, 853(1):L12, 2018.
- [116] B. P. Abbott et al. A gravitational-wave standard siren measurement of the Hubble constant. *Nature*, 551(7678):85–88, 2017.
- [117] T. M. C. Abbott et al. Dark Energy Survey Year 1 Results: A Precise H_0 Measurement from DES Y1, BAO, and D/H Data. 2017.
- [118] D. Foreman-Mackey et al. emcee: The mcmc hammer. *PASP*, 125:306–312, 2013.
- [119] Christopher M. Biwer, Collin Capano, et al. In preparation.
- [120] Alex Nitz, Ian Harry, Duncan Brown, Christopher M. Biwer, Josh Willis, Tito Dal Canton, Larne Pekowsky, Thomas Dent, Andrew R. Williamson, Collin Capano, Soumi De, Miriam Cabero, Bernd Machenschalk, Prayush Kumar, Steven Reyes, Thomas Massinger, Amber Lenon, Stephen Fairhurst, Alex Nielsen, shasvath, Duncan Macleod, Francesco Pannarale, Leo Singer, Stanislav Babak, Hunter Gabbard, Daniel Finstad, John Veitch, CBC Sugar, Sebastian Khan, and Lorena Magaña Zertuche. ligo-cbc/pycbc: Post-o2 release 6, February 2018.
- [121] Lee Samuel Finn. Aperture synthesis for gravitational wave data analysis: Deterministic sources. *Phys. Rev.*, D63:102001, 2001.
- [122] Christian Rover, Renate Meyer, and Nelson Christensen. Coherent Bayesian inference on compact binary inspirals using a network of interferometric gravitational wave detectors. *Phys. Rev.*, D75:062004, 2007.

- [123] Duncan A. Brown, Ian Harry, Andrew Lundgren, and Alexander H. Nitz. Detecting binary neutron star systems with spin in advanced gravitational-wave detectors. *Phys. Rev.*, D86:084017, 2012.
- [124] Michele Vallisneri, Jonah Kanner, Roy Williams, Alan Weinstein, and Branson Stephens. The LIGO Open Science Center. *J. Phys. Conf. Ser.*, 610(1):012021, 2015.
- [125] Kent Blackburn et al. *LOSC CLN Data Products for GW170817*, 2017.
- [126] J Driggers, S Vitale, A Lundgren, M Evans, K Kawabe, S Dwyer, K Izumi, and P Fritschel. Offline noise subtraction for Advanced LIGO, 2017. <https://dcc.ligo.org/LIGO-P1700260/public>.
- [127] Bruce Allen, Warren G. Anderson, Patrick R. Brady, Duncan A. Brown, and Jolien D. E. Creighton. FINDCHIRP: An Algorithm for detection of gravitational waves from inspiraling compact binaries. *Phys. Rev.*, D85:122006, 2012.
- [128] Craig Cahillane et al. Calibration uncertainty for Advanced LIGO's first and second observing runs. *Phys. Rev.*, D96(10):102001, 2017.
- [129] Aaron Viets et al. Reconstructing the calibrated strain signal in the Advanced LIGO detectors. *Class. Quant. Grav.*, 35(9):095015, 2018.
- [130] Naoki Seto. Prospects of ligo for constraining inclination of merging compact binaries associated with three-dimensionally localized short-hard grbs. *Phys. Rev.*, D75:024016, 2007.
- [131] K. G. Arun, Hideyuki Tagoshi, Chandra Kant Mishra, and Archana Pai. Synergy of short gamma ray burst and gravitational wave observations: Constraining the inclination angle of the binary and possible implications for off-axis gamma ray bursts. *Phys. Rev.*, D90(2):024060, 2014.
- [132] Bernard F. Schutz. Determining the Hubble Constant from Gravitational Wave Observations. *Nature*, 323:310–311, 1986.
- [133] Lee Samuel Finn and David F. Chernoff. Observing binary inspiral in gravitational radiation: One interferometer. *Phys. Rev.*, D47:2198–2219, 1993.

- [134] E. Troja et al. The X-ray counterpart to the gravitational wave event GW 170817. *Nature*, 551:71–74, 2017. [Nature551,71(2017)].
- [135] C. Guidorzi et al. Improved Constraints on H_0 from a Combined Analysis of Gravitational-wave and Electromagnetic Emission from GW170817. *Astrophys. J.*, 851(2):L36, 2017.
- [136] B.P. Abbott et al. Gravitational Waves and Gamma-rays from a Binary Neutron Star Merger: GW170817 and GRB 170817A. *Astrophys. J. Lett.*, 848(2):L13, 2017.
- [137] J.M. Lattimer. Impact of GW170817 for the nuclear physics of the EOS and the r-process. *Annals Phys.*, 411:167963, 2019.
- [138] R. Abbott et al. GW190814: Gravitational Waves from the Coalescence of a 23 Solar Mass Black Hole with a 2.6 Solar Mass Compact Object. *Astrophys. J. Lett.*, 896(2):L44, 2020.
- [139] Cody Messick et al. Analysis Framework for the Prompt Discovery of Compact Binary Mergers in Gravitational-wave Data. *Phys. Rev. D*, 95(4):042001, 2017.
- [140] Alexander H. Nitz, Tito Dal Canton, Derek Davis, and Steven Reyes. Rapid detection of gravitational waves from compact binary mergers with PyCBC Live. *Phys. Rev. D*, 98(2):024050, 2018.
- [141] Francois Foucart, Tanja Hinderer, and Samaya Nissanke. Remnant baryon mass in neutron star-black hole mergers: Predictions for binary neutron star mimickers and rapidly spinning black holes. *Phys. Rev. D*, 98(8):081501, 2018.
- [142] Collin D. Capano, Ingo Tews, Stephanie M. Brown, Ben Margalit, Soumi De, Sumit Kumar, Duncan A. Brown, Badri Krishnan, and Sanjay Reddy. Stringent constraints on neutron-star radii from multimessenger observations and nuclear theory. *Nature Astron.*, 4(6):625–632, 2020.
- [143] Leo P. Singer and Larry R. Price. Rapid bayesian position reconstruction for gravitational-wave transients. *Physical Review D*, 93(2), Jan 2016.

- [144] Mark Hannam, Duncan A. Brown, Stephen Fairhurst, Chris L. Fryer, and Ian W. Harry. When can gravitational-wave observations distinguish between black holes and neutron stars? *The Astrophysical Journal*, 766(1):L14, Mar 2013.
- [145] B.P. Abbott et al. GW150914: The Advanced LIGO Detectors in the Era of First Discoveries. *Phys. Rev. Lett.*, 116(13):131103, 2016.
- [146] Aaron Buikema et al. Sensitivity and performance of the Advanced LIGO detectors in the third observing run. *Phys. Rev. D*, 102(6):062003, 2020.
- [147] S.V. Dhurandhar and B.S. Sathyaprakash. Choice of filters for the detection of gravitational waves from coalescing binaries. 2. Detection in colored noise. *Phys. Rev. D*, 49:1707–1722, 1994.
- [148] Serge Droz, Daniel J. Knapp, Eric Poisson, and Benjamin J. Owen. Gravitational waves from inspiraling compact binaries: Validity of the stationary phase approximation to the Fourier transform. *Phys. Rev. D*, 59:124016, 1999.
- [149] Luc Blanchet, Thibault Damour, Bala R. Iyer, Clifford M. Will, and Alan G. Wiseman. Gravitational radiation damping of compact binary systems to second postNewtonian order. *Phys. Rev. Lett.*, 74:3515–3518, 1995.
- [150] Guillaume Faye, Sylvain Marsat, Luc Blanchet, and Bala R. Iyer. The third and a half post-Newtonian gravitational wave quadrupole mode for quasi-circular inspiralling compact binaries. *Class. Quant. Grav.*, 29:175004, 2012.
- [151] Samantha A. Usman et al. The PyCBC search for gravitational waves from compact binary coalescence. *Class. Quant. Grav.*, 33(21):215004, 2016.
- [152] Tito Dal Canton, Alexander H. Nitz, Bhooshan Gadre, Gareth S. Davies, Veronica Villa-Ortega, Thomas Dent, Ian Harry, and Liting Xiao. Realtime search for compact binary mergers in Advanced LIGO and Virgo’s third observing run using PyCBC Live. 8 2020.
- [153] Bruce Allen, Warren G. Anderson, Patrick R. Brady, Duncan A. Brown, and Jolien D. E. Creighton. Findchirp: An algorithm for detection of gravitational waves from inspiraling compact binaries. *Physical Review D*, 85(12), Jun 2012.

- [154] Tito Dal Canton and Ian W. Harry. Designing a template bank to observe compact binary coalescences in Advanced LIGO's second observing run. 5 2017.
- [155] Alejandro Bohé et al. Improved effective-one-body model of spinning, non-precessing binary black holes for the era of gravitational-wave astrophysics with advanced detectors. *Phys. Rev. D*, 95(4):044028, 2017.
- [156] Alexander H. Nitz, Thomas Dent, Tito Dal Canton, Stephen Fairhurst, and Duncan A. Brown. Detecting binary compact-object mergers with gravitational waves: Understanding and Improving the sensitivity of the PyCBC search. *Astrophys. J.*, 849(2):118, 2017.
- [157] B. Abbott et al. LIGO/Virgo public alerts user guide, 2019.
- [158] David F. Chernoff and Lee Samuel Finn. Gravitational radiation, inspiraling binaries, and cosmology. *Astrophys. J. Lett.*, 411:L5–L8, 1993.
- [159] Warren G. Anderson, Patrick R. Brady, Jolien D. E. Creighton, and Eanna E. Flanagan. Excess power statistic for detection of burst sources of gravitational radiation. *Physical Review D*, 63(4), Jan 2001.
- [160] K S Thorne. Gravitational radiation. In S. W. Hawking and W. Israel, editors, *Three hundred years of gravitation*, chapter 9, pages 330–458. Cambridge University Press, Cambridge, 1987.
- [161] Stephen Fairhurst. Triangulation of gravitational wave sources with a network of detectors. *New J. Phys.*, 11:123006, 2009. [Erratum: *New J. Phys.* 13, 069602 (2011)].
- [162] C P L Berry, B Farr, W M Farr, C-J Haster, I Mandel, H Middleton, L P Singer, A L Urban, A Vecchio, S Vitale, and et al. Early advanced ligo binary neutron-star sky localization and parameter estimation. *Journal of Physics: Conference Series*, 716:012031, May 2016.
- [163] Sylvia Biscoveanu, Salvatore Vitale, and Carl-Johan Haster. The reliability of the low-latency estimation of binary neutron star chirp mass. *The Astrophysical Journal*, 884(2):L32, Oct 2019.

- [164] Tito Dal Canton, Alexander H. Nitz, Bhooshan Gadre, Gareth S. Davies, Verónica Villa-Ortega, Thomas Dent, Ian Harry, and Liting Xiao. Realtime search for compact binary mergers in advanced ligo and virgo’s third observing run using pycbc live, 2020.
- [165] Frank J. Massey. The kolmogorov-smirnov test for goodness of fit. *Journal of the American Statistical Association*, 46(253):68–78, 1951.
- [166] Liang Dai, Tejaswi Venumadhav, and Barak Zackay. Parameter Estimation for GW170817 using Relative Binning. 6 2018.
- [167] Shasvath J. Kapadia et al. A self-consistent method to estimate the rate of compact binary coalescences with a Poisson mixture model. *Class. Quant. Grav.*, 37(4):045007, 2020.
- [168] Jocelyn S. Read, Charalampos Markakis, Masaru Shibata, Koji Uryu, Jolien D. E. Creighton, and John L. Friedman. Measuring the neutron star equation of state with gravitational wave observations. *Phys. Rev.*, D79:124033, 2009.
- [169] Samuel E. Gralla. On the Ambiguity in Relativistic Tidal Deformability. *Class. Quant. Grav.*, 35(8):085002, 2018.
- [170] Alex Nitz et al. *PyCBC v1.9.4*, 2018.
- [171] James M. Lattimer and Madappa Prakash. The Equation of State of Hot, Dense Matter and Neutron Stars. *Phys. Rept.*, 621:127–164, 2016.
- [172] James M. Lattimer. The nuclear equation of state and neutron star masses. *Ann. Rev. Nucl. Part. Sci.*, 62:485–515, 2012.
- [173] John Antoniadis et al. A Massive Pulsar in a Compact Relativistic Binary. *Science*, 340:6131, 2013.
- [174] J. R. Oppenheimer and G. M. Volkoff. On Massive neutron cores. *Phys. Rev.*, 55:374–381, 1939.
- [175] Sergey Postnikov, Madappa Prakash, and James M. Lattimer. Tidal Love Numbers of Neutron and Self-Bound Quark Stars. *Phys. Rev.*, D82:024016, 2010.

- [176] Weare J. Goodman J. *Commun. Appl. Math. Comput. Sci.*, 5(1):65–80, 2010.
- [177] P. Welch. The use of fast fourier transform for the estimation of power spectra: A method based on time averaging over short, modified periodograms. *IEEE Transactions on Audio and Electroacoustics*, 15(2):70–73, Jun 1967.
- [178] B. P. Abbott et al. Properties of the binary neutron star merger GW170817. 2018.
- [179] Tyson B. Littenberg and Neil J. Cornish. Bayesian inference for spectral estimation of gravitational wave detector noise. *Phys. Rev.*, D91(8):084034, 2015.
- [180] Fernando Pérez and Brian E. Granger. IPython: a system for interactive scientific computing. *Computing in Science and Engineering*, 9(3):21–29, May 2007.
- [181] S. De et al. *SUGWG GitHub Repository*, 2018.
- [182] Tianqi Zhao and James M. Lattimer. Tidal Deformabilities and Neutron Star Mergers. 2018.
- [183] Leslie Wade, Jolien D. E. Creighton, Evan Ochsner, Benjamin D. Lackey, Benjamin F. Farr, Tyson B. Littenberg, and Vivien Raymond. Systematic and statistical errors in a bayesian approach to the estimation of the neutron-star equation of state using advanced gravitational wave detectors. *Phys. Rev.*, D89(10):103012, 2014.
- [184] Kevin Barkett et al. Gravitational waveforms for neutron star binaries from binary black hole simulations. *Phys. Rev.*, D93(4):044064, 2016.
- [185] Mark Hannam, Duncan A. Brown, Stephen Fairhurst, Chris L. Fryer, and Ian W. Harry. When can gravitational-wave observations distinguish between black holes and neutron stars? *Astrophys. J.*, 766:L14, 2013.
- [186] James M. Lattimer and Yeunhwan Lim. Constraining the Symmetry Parameters of the Nuclear Interaction. *Astrophys. J.*, 771:51, 2013.
- [187] S. Gandolfi, J. Carlson, and Sanjay Reddy. The maximum mass and radius of neutron stars and the nuclear symmetry energy. *Phys. Rev.*, C85:032801, 2012.

- [188] J. E. Lynn, I. Tews, J. Carlson, S. Gandolfi, A. Gezerlis, K. E. Schmidt, and A. Schwenk. Chiral Three-Nucleon Interactions in Light Nuclei, Neutron- α Scattering, and Neutron Matter. *Phys. Rev. Lett.*, 116(6):062501, 2016.
- [189] Christian Drischler, Kai Hebeler, and Achim Schwenk. Asymmetric nuclear matter based on chiral two- and three-nucleon interactions. *Phys. Rev.*, C93(5):054314, 2016.
- [190] Ingo Tews, James M. Lattimer, Akira Ohnishi, and Evgeni E. Kolomeitsev. Symmetry Parameter Constraints from a Lower Bound on Neutron-matter Energy. *Astrophys. J.*, 848(2):105, 2017.
- [191] I. Tews, T. Krüger, K. Hebeler, and A. Schwenk. Neutron matter at next-to-next-to-next-to-leading order in chiral effective field theory. *Phys. Rev. Lett.*, 110(3):032504, 2013.
- [192] Andrew W. Steiner, James M. Lattimer, and Edward F. Brown. The Equation of State from Observed Masses and Radii of Neutron Stars. *Astrophys. J.*, 722:33–54, 2010.
- [193] N. Degenaar and V. F. Suleimanov. Testing the equation of state of neutron stars with electromagnetic observations. 2018.
- [194] Sebastien Guillot and Robert E. Rutledge. Rejecting proposed dense-matter equations of state with quiescent low-mass X-ray binaries. *Astrophys. J.*, 796(1):L3, 2014.
- [195] James M. Lattimer and Andrew W. Steiner. Neutron Star Masses and Radii from Quiescent Low-Mass X-ray Binaries. *Astrophys. J.*, 784:123, 2014.
- [196] A. W. Shaw, C. O. Heinke, A. W. Steiner, S. Campana, H. N. Cohn, W. C. G. Ho, P. M. Lugger, and M. Servillat. The radius of the quiescent neutron star in the globular cluster M13. 2018.
- [197] T. M. Tauris et al. Formation of Double Neutron Star Systems. *Astrophys. J.*, 846(2):170, 2017.

- [198] B. P. Abbott et al. GW170817: Measurements of neutron star radii and equation of state. 2018.
- [199] Kent Yagi and Nicolas Yunes. Approximate Universal Relations among Tidal Parameters for Neutron Star Binaries. *Class. Quant. Grav.*, 34(1):015006, 2017.
- [200] Katerina Chatziioannou, Carl-Johan Haster, and Aaron Zimmerman. Measuring the neutron star tidal deformability with equation-of-state-independent relations and gravitational waves. *Phys. Rev.*, D97(10):104036, 2018.
- [201] Soumi De, Daniel Finstad, James M. Lattimer, Duncan A. Brown, Edo Berger, and Christopher M. Biwer. Tidal Deformabilities and Radii of Neutron Stars from the Observation of GW170817. *Phys. Rev. Lett.*, 121(9):091102, 2018. [Erratum: *Phys. Rev. Lett.*121,no.25,259902(2018)].
- [202] F.J. Fattoyev, J. Piekarewicz, and C.J. Horowitz. Neutron Skins and Neutron Stars in the Multimessenger Era. *Phys. Rev. Lett.*, 120(17):172702, 2018.
- [203] I. Tews, J. Margueron, and S. Reddy. Critical examination of constraints on the equation of state of dense matter obtained from GW170817. *Phys. Rev. C*, 98(4):045804, 2018.
- [204] Ben Margalit and Brian D. Metzger. Constraining the Maximum Mass of Neutron Stars From Multi-Messenger Observations of GW170817. *Astrophys. J. Lett.*, 850(2):L19, 2017.
- [205] Eemeli Annala, Tyler Gorda, Alekski Kurkela, and Alekski Vuorinen. Gravitational-wave constraints on the neutron-star-matter Equation of State. *Phys. Rev. Lett.*, 120(17):172703, 2018.
- [206] Carolyn Raithel, Feryal Özel, and Dimitrios Psaltis. Tidal deformability from GW170817 as a direct probe of the neutron star radius. *Astrophys. J. Lett.*, 857(2):L23, 2018.
- [207] Tim Dietrich, Michael W. Coughlin, Peter T. H. Pang, Mattia Bulla, Jack Heinzl, Lina Issa, Ingo Tews, and Sarah Antier. Multimessenger constraints on the neutron-star equation of state and the Hubble constant. *Science*, 370(6523):1450–1453, 2020.

- [208] Mohammad Al-Mamun, Andrew W. Steiner, Joonas Nättilä, Jacob Lange, Richard O’Shaughnessy, Ingo Tews, Stefano Gandolfi, Craig Heinke, and Sophia Han. Combining electromagnetic and gravitational-wave constraints on neutron-star masses and radii. *Phys. Rev. Lett.* (*in press*), 2021.
- [209] B. P. Abbott et al. GW170817: Observation of Gravitational Waves from a Binary Neutron Star Inspiral. *Phys. Rev. Lett.*, 119(16):161101, 2017.
- [210] David Radice and Liang Dai. Multimessenger Parameter Estimation of GW170817. *Eur. Phys. J. A*, 55(4):50, 2019.
- [211] Thomas E. Riley et al. A *NICER* View of PSR J0030+0451: Millisecond Pulsar Parameter Estimation. *Astrophys. J. Lett.*, 887(1):L21, 2019.
- [212] Thomas E. Riley et al. A *NICER* View of the Massive Pulsar PSR J0740+6620 Informed by Radio Timing and XMM-Newton Spectroscopy. 5 2021.
- [213] M. C. Miller et al. The Radius of PSR J0740+6620 from *NICER* and XMM-Newton Data. 5 2021.
- [214] D. Adhikari et al. Accurate Determination of the Neutron Skin Thickness of ^{208}Pb through Parity-Violation in Electron Scattering. *Phys. Rev. Lett.*, 126(17):172502, 2021.
- [215] Brendan T. Reed, F. J. Fattoyev, C. J. Horowitz, and J. Piekarewicz. Implications of PREX-2 on the Equation of State of Neutron-Rich Matter. *Phys. Rev. Lett.*, 126(17):172503, 2021.
- [216] Mohammad Al-Mamun, Andrew W. Steiner, Joonas Nättilä, Jacob Lange, Richard O’Shaughnessy, Ingo Tews, Stefano Gandolfi, Craig Heinke, and Sophia Han. Combining Electromagnetic and Gravitational-Wave Constraints on Neutron-Star Masses and Radii. *Phys. Rev. Lett.*, 126(6):061101, 2021.
- [217] B. P. Abbott et al. GW190425: Observation of a Compact Binary Coalescence with Total Mass $\sim 3.4M_{\odot}$. *Astrophys. J. Lett.*, 892(1):L3, 2020.
- [218] Walter Del Pozzo, Tjonnie G. F. Li, Michalis Agathos, Chris Van Den Broeck, and Salvatore Vitale. Demonstrating the feasibility of probing the neutron star

- equation of state with second-generation gravitational wave detectors. *Phys. Rev. Lett.*, 111(7):071101, 2013.
- [219] Francisco Hernandez Vivanco, Rory Smith, Eric Thrane, Paul D. Lasky, Colm Talbot, and Vivien Raymond. Measuring the neutron star equation of state with gravitational waves: The first forty binary neutron star merger observations. *Phys. Rev. D*, 100(10):103009, 2019.
- [220] Kevin Kuns, Evan Hall, Joshua Smith, Matthew Evans, Peter Fritschel, Christopher Wipf, and Stefan Ballmer. Cosmic explorer sensitivity curves, 2020.
- [221] C. M. Biwer, Collin D. Capano, Soumi De, Miriam Cabero, Duncan A. Brown, Alexander H. Nitz, and V. Raymond. PyCBC inference: A python-based parameter estimation toolkit for compact binary coalescence signals. *Publications of the Astronomical Society of the Pacific*, 131(996):024503, jan 2019.
- [222] Jonathan Goodman and Jonathan Weare. Ensemble samplers with affine invariance. *Communications in Applied Mathematics and Computational Science*, 5(1):65–80, January 2010.
- [223] Daniel Wysocki, Richard O’Shaughnessy, Leslie Wade, and Jacob Lange. Inferring the neutron star equation of state simultaneously with the population of merging neutron stars. 1 2020.
- [224] Cosmic explorer horizon study. <https://dcc.cosmicexplorer.org/CE-P2100003>.
- [225] Michael W. Coughlin, Tim Dietrich, Ben Margalit, and Brian D. Metzger. Multimessenger Bayesian parameter inference of a binary neutron star merger. *Mon. Not. Roy. Astron. Soc.*, 489(1):L91–L96, 2019.

Daniel Finstad

DEPARTMENT OF PHYSICS
SYRACUSE UNIVERSITY
SYRACUSE, NY 13244, USA

E-MAIL: dfinstad@syr.edu
PHONE: +1 315-443-3901

EDUCATION

PhD Candidate, Department of Physics
Syracuse University
Advisor: Prof. Duncan Brown

Aug 2016 - Aug 2021

Bachelor of Arts in Physics
Bachelor of Arts in Applied Mathematics
University of California, Berkeley

2013-2015

Associate of Science in Physics
Long Beach City College

2010-2013

PHD RESEARCH

- Bayesian inference analyses of gravitational-wave signals from neutron star and black hole binaries; constraining the nuclear equation of state using neutron star mergers.
- Development of fast likelihood evaluation methods to rapidly identify and localize future potential multimessenger sources
- Code development for PyCBC - open software for analyzing gravitational-wave data <https://github.com/gwastro/pycbc>.

COMPUTATIONAL EXPERIENCE

Programming Languages and Platforms

Proficient: Python, C, Bash, jupyter, HDF5

Substantial Knowledge: Fortran, MATLAB, Mathematica, XML, IDL

High-Throughput and Parallel Computing

HTCondor, Open Science Grid, Pegasus, OpenMP, MPI

- Proficient at running software on highly parallel and high-throughput computing clusters.
- Substantial experience in developing software and scientific workflows for parallel computing and designed to be run on high-throughput clusters.

Code/Data Sharing and Management

Github, Gitlab, Zenodo, Bitbucket, Docker, Singularity, Globus

- Proficient at using these platforms for building, maintaining, reviewing, transferring, and publishing version-controlled code and data generated in large collaborative projects.

Software

Maintainer: PyCBC

Analyses and simulations with: PyCBC, MESA, EMCEE, Dynesty, Astropy

HONORS, AWARDS, AND FELLOWSHIPS

Research Excellence Doctoral Funding Fellowship , Syracuse University – Awarded to 30 graduate students across 16 departments	2020-2021
STEM Fellowship , Syracuse University	2018-2019
NSF PAARE Fellowship , Syracuse University	2017-2018

PUBLICATIONS

Short author papers – first author: 3, contributing author: 1.

Short Author - Refereed and Preprints:

3. **Daniel Finstad**, Duncan A. Brown, *Fast Parameter Estimation of Binary Mergers for Multimessenger Followup*, arXiv:2009.13759 (2020), Accepted by Astrophysical Journal Letters.
2. Soumi De, **Daniel Finstad**, James M. Lattimer, Duncan A. Brown, Edo Berger, Christopher M. Biwer, *Tidal Deformabilities and Radii of Neutron Stars from the Observation of GW170817*, Phys. Rev. Lett., 121, 091102 (2018). [302 citations]
 - **Data release:** <https://github.com/sugwg/gw170817-common-eos>
1. **Daniel Finstad**, Soumi De, Duncan A. Brown, Edo Berger, Christopher M. Biwer, *Measuring the Viewing Angle of GW170817 with Electromagnetic and Gravitational Waves*, Astrophys. J. Lett. 860, L2(2018). [40 citations]
 - **Data release:** <https://github.com/sugwg/gw170817-inclination-angle>

Short Author - In Preparation:

1. **Daniel Finstad**, Duncan A. Brown et al., *Prospects for Precise Equation of State Measurements from Advanced LIGO and Cosmic Explorer* (2021).

LIGO Scientific Collaboration Publications:

Following are publications to which I have contributed as a member of the collaboration from Sep 2016 to Jan 2018

2. B. P. Abbott et al., *GW170817: Observation of gravitational waves from a binary neutron star inspiral*, Phys. Rev. Lett., 119, 161101 (2017).
1. B. P. Abbott et al., *Multi-messenger observations of a binary neutron star merger*, Astrophys. J. Lett., 848,2 (2017).

PRESENTATIONS

American Physical Society April Meeting

Denver, Colorado, USA

Using Gravitational Waves to Observe the Black Hole Mass Gap due to Pair-Instability Supernovae

April 2019

Eastern Gravity Meeting

Brooklyn, New York, USA

Measuring the viewing angle of GW170817 with electromagnetic and gravitational waves

May 2018

PROFESSIONAL DEVELOPMENT

Data Science at Scale Internship

Los Alamos National Laboratory

Summer Internship

Summer 2019

MESA (Modules for Experiments in Stellar Astrophysics) Summer School

University of California, Santa Barbara

Summer School

Aug 2018

Neutron Star Merger Summer School

Facility for Rare Isotope Beams, Michigan State University

Summer School

May 2018

MENTORING

Co-mentored Syracuse University undergraduate student Laurel White (Physics major) on gravitational-wave data analysis research projects. Tools and techniques involved: Bayesian inference, cluster computing, python, bash.

Fall 2020

PAST RESEARCH EXPERIENCE

Research Assistant

UC Berkeley Space Sciences Lab (Advisor: Prof. Andrew Howard)

Data analysis software development:

Optical fiber characterization for radial velocity measurements using Keck Planet Finder

Spring 2016

Research Student

UC Berkeley Space Sciences Lab (Advisor: Dr. Ed Wishnow)

Infrared interferometer instrumentation at Mt. Wilson Observatory

2015